UNIVERSITY OF CALIFORNIA, MERCED

Mesoscale Porous Nanomaterials Templated by a Liquid Crystal Phase Transition

A dissertation submitted in partial satisfaction of the requirements for the degree
Doctor of Philosophy

in

Physics

by

Tayebeh Sheida Riahinasab

Committee in charge:

Professor Michael Scheibner, Chair
Professor Linda S. Hirst, Advisor
Professor Jay E. Sharping
Professor Benjamin J. Stokes

2019

The Dissertation of Sheida Tayebeh Riahinasab is approved, and is acceptable in quality and form for publication on microfilm and electronically:

Jay E. Sharping

Benjamin J. Stokes

Linda S. Hirst

Michael Scheibner, Chair

University of California, Merced

2019

Dedication

To my mom …

Contents

1 Chapter 1 1

Introduction 1

1.1 Particle Self Assembly 1

1.2 Liquid Crystal Materials 2

1.3 Nematic Liquid Crystal 6

1.4 Nematic Orientational Order 6

1.5 Phase Transitions 7

1.6 Topological Defects 8

1.7 Nanoparticles 12

1.8 Quantum Dots 13

1.9 Optical Properties of Quantum Dots 14

2 Chapter 2 18

Theory 18

2.1 Orientational Order Parameter 18

2.2 Elastic Properties of Nematic Liquid Crystal 20

2.3 Propagation of Light in Anisotropic Optical Media 23

2.4 Polarization 25

Linear Polarization States 25

2.5 Circular Polarization States 25

2.6 Propagation of Light in Uniform Anisotropic Optical Media 26

2.7 Birefringence 27

3 Chapter 3 28

Methods 28

3.1 Polarized Optical Microscopy 28

3.2 Fluorescence Microscopy 31

3.3 Introduction to proton NMR 33

3.4 Scanning Electron Microscope: 35

3.5 Small Angle X-ray Scattering 36

3.6 Differential Scanning Calorimetry (DSC) 37

4 Chapter 4 40

Designing ligands for robust micro-capsule formation 40

4.1 Introduction 40

4.2 Molecular Structure of Ligands 42
4.3 Characterization of Ligands using Polarized Optical Microscopy 44
4.4 Differential Scanning Calorimetry of Ligands 45
4.5 Ligand Exchange Process 46
4.6 Nuclear Magnetic Resonance (NMR) Spectroscopy 46
4.7 Liquid Crystal/Quantum Dot Mixtures 48
4.8 Shell Formation Procedure 48
4.9 Preparation for SEM Imaging 50
4.10 SAXS Analysis of Shells 50
4.11 Conclusions 52
5 Chapter 5 54
Nanoparticle-based hollow microstructures formed by two-stage nematic nucleation and phase separation 54
5.1 Introduction 54
5.2 Results 56
5.3 Discussion 62
5.4 Methods 65
5.5 Conclusion 66
6 Chapter 6 67
Future work 67
7 Bibliography 69

Abbreviations

QDs	Quantum dots
NPs	Nano particles
LC	Liquid crystal
NLC	Nematic liquid crystal
NMR	Nuclear magnetic resonance
TEM	Transmission electron microscopy
SEM	Scanning electron microscopy
SAXS	Small angle x-ray scattering
DSC	Differential scanning calorimetry
CdSe	Cadmium selenide
ZnS	Zinc sulfide
5CB	4- cyno-4'-pentylbiphenyl
PVA	Polyvinyl alcohol
UV-Vis	Ultraviolet - visible
POM	Polarized optical microscopy
FL	Fluorescence
Wt%	Weight percent
nm	Nanometer
ml	Milliliter
$CDCl_3$	Deuterated chloroform
^{13}C	Carbon-13
^{1}H	Hydrogen-1
s	Second
eV	Electronvolt
KeV	Kiloelectronvolt
μm	Micrometer
CTAB	Cetyltrimethylammonium bromide
mm	Millimeter
ODA	Octylamines
CCD	Charge-coupled device
PL	Photoluminescence
FE	Field emission
min	Minute
L	Ligand
FRET	Förster resonance energy transfer
NN Lab	Nanomaterials and nanofabrication
LC-QDs	Ligand modified QDs
ALS	Advanced light source
μW	Microwatt
PL	Pro-mesogenic ligands

List of figures

Figure 1-1. Molecular structures of (a) cholesterol-1 myristate and (b) cholesterol-1 benzoate 3
Figure 1-2. Schematic illustration of phase transition behavior and the molecular order of matter discussed in this research. Crystal (has the long range positional and orientational order), liquid (the molecules undergo random motion with molecules axes varying in different direction), and liquid crystals materials. . T_N represents disordering (melting) temperature of the crystalline state, and T_I is the isotropic temperature. Liquid crystal exists in a state between solid and liquid. In addition to these main phases of matter, there are many mesophases or intermediate states. 3
Figure 1-3. Molecular structure of 4-cyano-4'-pentylbiphenyl. Alternatively known as 5CB, is a material which has a rod-like shape and in bulk exhibits the nematic phase at room temperature. 4
Figure 1-4. The Nematic liquid crystal phase. The molecules locally orient in a common direction, defined by the director *n* (The director shows the local average orientation of the molecules, which tend to point in the same direction as their neighbors) 5
Figure 1-5. Schematic orientation of molecules in the smectic C and smectic A phases... 5
Figure 1-6. Illustration of the ordering of molecules in a cholesteric LC. The nematic director twists along an axis perpendicular to the long molecular axis. 6
Figure 1-7. Represents the angle between a liquid crystal molecule and the director. 7
Figure 1-8. A first order phase transition; plot of order parameter vs. temperature showing the discontinuity at transition temperature $T_{NI.}$ 8
Figure 1-9. Schlieren texture in a nematic liquid crystal imaged using polarized optical microscopy . The cross sign represents the orientation of the cross polarizers and if the direction of director is in direction of any polarizers then I see black (extinction). For the lighter areas the director (*n*) lies at an angle between the polarizers, revealing the texture. 9
Figure 1-10. a) Defects in a capillary tube. Two-point defects are shown, one of which is opposite to the other b) the two possible director configurations inside the droplets 10
Figure 1-11. Six different types of point defect [39]. 10
Figure 1-12. Burgers circuit around a defect point. The circuit is followed around in the counterclockwise direction. In this case we have a +1 defect. 11
Figure 1-13. Different director orientations for +1 and -1 topological defects next to their appearance under the polarizing microscope with slightly uncrossed polarizers 11
Figure 1-14. Schlieren texture in nematic liquid crystal including defects labelled by their topological charge 12
Figure 1-15. Transmission electron Microscopy (TEM) image of quantum dot nanoparticles 13
Figure 1-16. Transmission electron microscope image of a quantum dot 14
Figure 1-17. a) Increasing the size of quantum dots, the semiconductor band gap decreases. Splitting the energy level due to the quantum confinement effect b) emission spectra of different size of QDs 15
Figure 2-1. A rigid rod-like shape of an elongated liquid crystal molecule with three axes. 18

Figure 2-2. Schematic diagram showing the orientation of a rod like molecule 18
Figure 2-3. Schematic of order parameter for different state; isotropic (a), liquid crystal (b), and crystal (c)..... 20
Figure 2-4. These are most commonly known as splay, twist, and bend. Splay occurs when molecular orientation is perpendicular to a gradient direction. Twist occurs when molecular orientation changes as you travel through different axis. And bend occurs when molecular orientation is parallel to a gradient direction. 21
Figure 3-1. Schematic of a polarized optical microscope 28
Figure 3-2. Two different polarized optical microscopic images of the same brush defect in the nematic phase taken at two different arbitrary angles 45° apart. [70] 29
Figure 3-3. The geometry of a liquid crystal slab rotated between crossed polarizers. [70] 30
Figure 3-4. Schematic presentation of nematic liquid crystal alignment in cell with (b) planar and (d) Homeotropic anchoring 31
Figure 3-5. Schematic for a fluorescence microscope [63] 32
Figure 3-6. The schematic of confocal microscopy [70] 33
Figure 3-7. Schematic operation of a basic NMR spectrometer [63] 34
Figure 3-8. Scattering geometry of Bragg diffraction 36
Figure 3-9. Schematic of a typical transmission x-ray scattering beam-line [70]. S1-3 are slits to define the beam and D is the sample to detector distance. 37
Figure 3-11. A high-sensitivity differential scanning calorimeter typically used for liquid crystal materials is shown in (a) and a close-up picture of the two furnaces in (b). Picture (c) shows an aluminum sample pan used to encapsulate the sample. These sample pans hold a few milligrams of material. [70] 38
Figure 3-12. an example of differential scanning calorimetric data for a thermotropic liquid crystal (8CB), the first peak is the smectic A to nematic phase transition and second peak is the nematic to isotropic liquid phase transition. Delta H is the enthalpy of the transitions. [70]..... 39
Figure 4-1. Schematic of molecular structure of mesogenic ligand 42
Figure 4-2. Ligand library synthesis, “Reproduced with permission from the American Chemical Society” 44
Figure 4-3. Birefringence textures of 4a–h observed using polarized optical microscopy (10X objective). Transition temperature (T_{trans}) and latent heat (ΔH_{trans}) of the only observed differential scanning calorimetry event for each ligand are included in parentheses. Crossed arrows indicate polarizer directions. “Reproduced with permission from the American Chemical Society” [106] 45
Figure 4-4. Differential scanning calorimetry traces for pure ligands showing baseline corrected heat flow as a function of temperature. Each ligand exhibits a single peak indicative of a direct phase transition from the crystal to isotropic liquid phase. “ Reproduced with permission from the American Chemical Society” [106] 45
Figure 4-5. Schematic representation of non-mesogenic ODA ligands and modified surface of QDs with mesogenic and ODA ligands (LC-QDs), ... 46
Figure 4-6. The ^{1}H NMR spectrum after ligand exchange obtained at 500 MHz in CDCl3. “Reproduced with permission from the American Chemical Society” [106]..... 47

Figure 4-7. Same-slide ambient temperature fluorescence microscope images of QD mesostructures formed from 6.2 nm CdSe/ZnS QDs (λmax= 540 nm) functionalized with ligand 4a following disper-sion in 4-cyano-4'-pentylbiphenyl (0.15 wt %) after a) depositing on the slide; b) reheating the slide through the clearing point; and c) reheating the slide to 350 °C. Images record total fluorescence emission intensity following excitation at λ_{max}= 540 nm. “Reproduced with permission from the American Chemical Society” [106] 49
Figure 4-8. Fluorescence microscopy images of QD mesostructures formed from 6 nm CdSe/ZnS QDs (λmax= 540 nm) functionalized with different ligands. “Reproduced with permission from the American Chemical Society” [106]..... 49
Figure 4-9. Scanning electron microscope images of a) intact and b) fractured QD capsules formed from 540 nm CdSe/ZnS QDs functionalized with ligand 4a. “Reproduced with permission from the American Chemical Society” [106]SAXS Analysis of Shells 50
Figure 4-10. Small-angle x-ray scattering (SAXS) data collected at 10 keV with 1 s exposure for assembled quantum dot microshells suspended in nematic liquid crystal prepared at 0.15 wt %, and plotted as relative intensity as a function of scattering vector, q. The characteristic interparticle spacing, d, is calculated from each peak position as 2π/q. Insert shows interparticle spacing (d) as a function of ligand aminoalkyl chain length. “Reproduced with permission from the American Chemical Society” [106]..... 51
Figure 4-11. Quenching effect of temperature on QD Luminescence. “Reproduced with permission from the American Chemical Society” [106]..... 52
Figure 5-1. Hollow nanoparticle-based microstructures formed from ligand-modified quantum dots. Fluorescence microscopy imaging demonstrates the three distinct quantum dot structures formed under different conditions: a branching tubular network, formed at 1 °C min^{-1}, b solid closed-cell foam-like structures formed at 30 °C min^{-1}, and c hollow shell capsules formed at 200 °C min^{-1}. All structures are composed of 620 nm CdSe/ZnS ligand-modified quantum dots, suspended in nematic liquid crystal initially at 0.15 wt% at room temperature. d Sequence of reactions used to prepare the mesogenic ligand (8) for nanoparticle attachment. “Reproduced with permission from the Nature Publishing Group” [104]..... 57
Figure 5-2. Size dependence of cooling (quench) rate and nanoparticle concentration. Representative fluorescence microscopy images of spherical shells formed from ligand-modified quantum dots (LC-QDs) at a–c fixed LC-QD concentration of 0.3 wt% in 5CB, varying cooling rate, and d–f fixed cooling rate of 200 °C min^{-1}, varying LC-QD concentration in 5CB. g Qualitative phase diagram for the three distinct morphologies predominantly observed as a function of cooling rate and concentration. General morphological zones on the diagram are indicated by the colored boxes with circle size representative of structure size. h, i Plots of average shell diameter vs. cooling rate and concentration respectively, with error bars indicating standard deviation (s.d.); the total number of measured structures, *n*, ranged from 10 to 183. “Reproduced with permission from the Nature Publishing Group” [104] 58
Figure 5-3. Confocal imaging of foam structures. Confocal microscope *z*-projection images of a quantum dot foam droplet (*z* depth = 23.13 μm) with four representative slices (b–e) at *z* intervals of 0.665 μm; and f a large foam structure (*z* depth = 91.90 μm). Scale bars for b–e are 50 μm. “Reproduced with permission from the Nature Publishing Group” [104] ... 60

Figure 5-4. a–d Experimental high-speed video imaging snapshots representative of four stages in nematic nucleation and growth during the process: a initial nucleation and growth, b coarsening, c domain separation, and d secondary nucleation. Scale bars is 50 μm. “Reproduced with permission from the Nature Publishing Group” [104] 61
Figure 5-5. Understanding the mechanism for structure differentiation. (a–f) Series of snapshots taken from a fluorescence microscope movie demonstrating the foam formation process in a droplet of liquid crystal with initially well-dispersed quantum dots (QDs). In these images, QD-rich areas appear light and QD- poor areas appear dark. The curved white line in these images is the edge of the droplet, with liquid crystal on the right of this curve. Scale bars for (a–f) are 100 μm. g A zoomed-in view from e with the arrow indicating inner nematic domain nucleation. h A confocal microscope image of several foam structures suspended in 5CB. Images taken from stack of 40 images, Max projected and false colored using Fiji software. i schematics illustrating the role of secondary nucleation on final structure showing the particle-rich isotropic phase as white and the nematic phase as gray left: secondary domains nucleate early on while the isotropic domain is still connected, center: secondary domains nucleate after isotropic domains have separated, and right: secondary domains nucleate late, when isotropic domains have already reached a small size. “Reproduced with permission from the Nature Publishing Group” [104] 64

List of tables

Table 4-1----------44

Table 6-1 ----------74

Acknowledgments

There are too many to thank for this opportunity. My largest will go to my advisor, Prof. Linda S.Hirst. Without her guidance, this could have not been possible. She created for me precious opportunity to be able to participate and present our work in numerous conferences. She also supported me in difficult times, believed in me, and gave me grateful suggestion when I was wandering at the crossroads. I am also thankful to my committee members: Dr. Michael Scheibner, Dr. Benjamin J. Stokes, and Dr. Jay E. sharping.

I would also like to thank my lab mates for this collaboration and assistance. In particular, I would like to thank Amanda Tan and Fereshteh Memarian for their kind support. Special lab mate thanks go to Dr. Joe Lopes for his superb help and encouragement from day one to last minutes of the defense.

I also acknowledge the funding support I was fortunate to have during my studies: UC Merced Physics Department, UC Merced Grad Division, and NSF- CBET-1507551.

I also like to thank our collaborators at Dr. Stokes lab, particularly Amir Keshavarz, Prof. Sai Ghosh, and Prof. Robin Selinger from Kent State University.

Finally, I would like to thank my parents and Dr. Arghavan Alamatsaz, and Dr. Daniel Esmaili for their endless support and encouragement.

As always it is impossible to mention everybody who has been involved in this work.

Curriculum Vitae

Sheida T. Riahinasab

(626)-388-0420 || Sheida.T.Riahi@Gmail.com

Summary

- Product reliability evaluation by managing sample test and analyzing metrology results.

- Performance evaluation of electrochromic device by characterizing the single film and film stack.

- Enthusiastic and self-motivated scientist with 5 years of research experience developing novel methods to improve the efficiency of semiconductor for photovoltaic application by 9%.

- Project manager for an interdisciplinary collaboration resulting in the discovery of nanofoams in the liquid crystal. A first-authored 2019 paper published in Nature Communication and was integral to the creation of a patent.

- Having an innovative idea resulting in $70K funding: Writing a proposal and receiving $70K fund. The funding was used to buy an advanced microscope for visualization of our system. This advanced microscope assisted 10 personnel to conduct 4500 hours of research.

- Extensive experience in micro-fluidic device fabrication by using photolithography in clean room.

Technical Skills

Characterization Techniques:

- Scanning Electron Microscopy (SEM)
- Thin Film Deposition
- Small Angle X-ray Scattering (SAXS)
- Transmission Electron Microscopy (TEM)
- Fluorescence Confocal Microscopy (FL)
- Time Lapse Photography (TLP)
- Focused Ion Beam Microscopy (FIB)
- Atomic Force Microscope (AFM)
- Nuclear Magnetic Resonance (NMR)
- Fourier-transform infrared spectroscopy
- Fiji/ImageJ
- Origin lab/Sigma plot
- Defect Inspection
- Physical Vapor Deposition (PVD)
- Electrospinning
- UV-Visible Spectrophotometry
- WetChem
- Lithography with+/- Photoresist
- Profilometer
- JMP (DOE, SPC, ANOVA)

Management Skills:

- Leadership & project management: Mentored grad student & led two collaborative projects
- Critical thinking & problem solving: Reverse engineered and improved a previous method for surface modification
- Self-management: Self-trained in most of the aforementioned experimental techniques

Experience

Reliability Engineer Intern Sep 2019-Present

View Inc, CA

- Conducted durability testing and characterized products through leading sample testing, subsequent metrology, and analyzing metrology results.
- Identified the root cause of device failure during process development.
- Designed experiment and analyzed results using DOE and ANOVA

Process Engineer Intern June-Aug (2019)

View Inc, MS

- Electrochromic (EC) single film deposition & characterization to improve the performance of the new generation of smart glass:
  - Optimized the performance of transparent conducting oxide (TCO) coater for single film deposition
  - Modeled and designed the experiment by using JMP
  - Deposited single film on a glass substrate by physical vapor deposition (sputtering)
  - Measured the thickness of single film deposition using a confocal microscope
  - Electrochemical characterization (cyclic voltammetry) of the single film by using WetChem lab
  - Checked the temperature of the substrate for deposition by using the MOLE
  - Electrochemical characterization (cyclic voltammetry) of the single film by using WetChem lab
  - Checked the temperature of the substrate for deposition by using the MOLE
- Used the GASP to measure stress (pressure per sq in) of the IGU
- Studied the electrochemistry of lite by using CVCC technique

Research Assistant 2014-Present

University of California Merced, CA

- Developed a novel method to self-assemble semiconductor nanoparticle into a variety of 3D structure in liquid crystal solvent

- Designed, and characterized a new library (25) of mesogenic (liquid crystal-like) ligands for nanoparticles, optimizing ligand exchange process
- Created novel meta-material (nanoparticle foam) for electromagnetic cloaking and a gas sensing
- Successfully led interdisciplinary collaborations with six chemists, two engineers, and ten physicists

Graduate Teaching Assistant

University of California Merced, CA

- Lead 7 labs & 6 discussions for PHYS 08/18 & Calculus I/II Spring 2014
- Taught fundamentals of math and its applications in physics for ten hours per weeks, more than 100 students for passing courses

Mentorship

University of California Merced, CA

- Mentoring of 5 undergrad & 4 grad students as a member of Soft Matter Laboratory
- Trained them in characterization techniques and helped prepare them to give presentations at conferences

Graduate Research Assistant 2011-2013

University of Memphis, TN

- Studied the lifetime of free radicals produced by x-ray irradiation in medical polymers with electron spin resonance
-
- Led team of 5 experimental physicists in projects ranging from pure science to application

Education

Ph.D. Candidate in Soft Condensed Matter Physics, 2013 - 2019
The University of California, Merced, (GPA: 3.82/4.0)

M.S. in Material Science Physics, 2011-2013
University of Memphis, (GPA 3.83/4.0)

B.S. in Physics, 2004-2008

University of Isfahan, (GPA 3.43/4.0)

Patent

• Filed, Hirst and Riahinasab, 2017. "Solid Foam Comprising Mesogenic Ligand-Functionalized Nanoparticles and Method of Making". Serial No. 62/574,02

Honors & Awards

• Grad dean's dissertation fellowship 2019

• Media article regarding discovery of nanofoams in liquid crystals 2019

• Grad student opportunity program fellowship 2017-2018

• Awarded best academic performance during first year of Ph.D. 2014

• NASA-funded Merced nanomaterials center for energy and sensing fellowship (MACES) 2017

• Research assistant/ physics graduate group summer fellowship, UC Merced 2015-2017

Publications

• ***S. T. Riahinasab***, A. Keshavarz, B.J. Stokes, L. S. Hirst, "Designing liquid crystalline ligands for increased quantum dots photovoltaic efficiency", Nanomaterials. Under preparation (2019)

• C. N. Melton, ***S. T. Riahinasab***, L. S. Hirst, "Formation and characterization of single quantum dot microshells", Emerging Liquid Crystal Technologies XII: PROC.SPIE, under preparation (2019)

• ***S. T. Riahinasab,*** A. Keshavarz, C. N. Melton, A. Elbaradei, G. I. Warren, B. J. Stokes, L. S. Hirst, "Nanoparticle-based hollow microstructures formed by two-stage nematic nucleation and phase separation", Nature communications. 2019 Feb 22; 10(1):894.

• A. Keshavarz, ***S. T. Riahinasab,*** B. J.Stokes, L. S. Hirst, "New promesogenic ligands for self-assembly of quantum dots into highly thermostable microcapsules via nematic templating", ACS Appl. Nano Mater., 2019, 2 (4), pp 2542–2547

• C. N. Melton, ***S. T. Riahinasab***, A. Keshavarz, B. J. Stokes, and L. S. Hirst. " Phase transition-driven nanoparticle assembly in liquid crystal droplets." Nanomaterials 8, no. 3 (2018): 146.

• ***S. T. Riahinasab***, A. Elbaradei, A. Keshavarz, B.J. Stokes, L. S. Hirst, "Nanoparticle microstructures template by liquid crystal phase-transition dynamics", Emerging Liquid Crystal Technologies XII: PROC.SPIE, 10125-2, (2017)

• L. S. Hirst, ***S. T. Riahinasab,*** C. N. Melton**,** "Liquid crystal composites as a route to 3D nanoparticle assembly", SPIE Newsroom. DOI: 10.1117/2.1201702.006865, (2017)

• J. Amaral, E. Betady, M. Quint, D. Martin, ***S. T. Riahinasab***, L. S. Hirst and S. Ghosh, "Effect of mesogenic ligands on short and long-term spectral dynamics and stability of core-shell CdSe /ZnS quantum dots", *Mater. Res. Exp* (2016)

• Muhammad J. Benjamin W, ***T Riahinasab***, Rudra G, Dipendra A, "A Comparative of radiation effect in medical-grade polymers: UHMWPE, PUC and PEEK", *Radiation Physics and Chemistry* (2015)

• ***Sheida T. Riahinasab.*** Electron spin resonance studies of UV- and X ray irradiated Poly (ethe- ether-ketone). Master's Thesis, 2013

Conferences

Talk: S. T. Riahinasab, Linda S. Hirst, "Nanoparticle-based hollow microstructures formed by two-stage nematic nucleation and phase separation", MRS, Phoenix, AZ, 2019

Talk: S. T. Riahinasab, Amir Keshavarz, Benjamin J. Stokes, Linda S. Hirst, "Designing Liquid Crystalline Ligands for Increased QD Photovoltaic Efficiency", APS March Meeting, Los Angles, CA, 2018

Talk: S. T. Riahinasab, Amir Keshavarz, Benjamin J. Stokes, Linda S. Hirst, "Designing Liquid Crystalline Ligands for Increased QD Photovoltaic Efficiency", APS Far West Section, University of California Merced, CA 2017

Talk: S. T. Riahinasab, Amir Keshavarz, Ahmed Elbaradei, Charles N. Melton, Gabrielle I. Warren, Benjamin J. Stokes, Linda S. Hirst, "Nanoparticle foams and capsules formed by liquid crystal phase transition templating", Gordon Research Conference, University of New England, ME, 2017

Poster: ***S. T. Riahinasab***, Amir Keshavarz, Ahmed Elbaradei, Charles N. Melton, Gabrielle I. Warren, Benjamin J. Stokes, Linda S. Hirst, "Nanoparticle foams and capsules formed by liquid crystal phase transition templating", The Biomedical Engineering Symposium, UCLA, CA, 2017

Poster: S. T. Riahinasab, A. Elbaradei, A. Keshavarz, B. Stokes, L. S. Hirst, "Nanoparticle foams formed by liquid crystal phase transition templating", University of Tufts, Boston, MA, 2017

Talk: S. T. Riahinasab, A. Elbaradei, A. Keshavarz, B. Stokes, L. S. Hirst, Nanoparticle Microstructure Templated by Liquid Crystal Phase-Transition Dynamics, APS March Meeting, New Orleans, LA, 2017

Talk: Linda S. Hirst, ***S. T. Riahinasab,*** C. N. Melton, Nanoparticles are sorted by elastic forces in a liquid crystal nano-composite to form three-dimensional solid structures including capsules and networks, SPIE, San Francisco, CA, 2017

Talk: S. T. Riahinasab, A. Elbaradei, A. Keshavarz, B. Stokes, L. S. Hirst, Nanoparticles Assembly via Phase Transition of Liquid Crystal Template, APS Far West Section, University of California Davis, Davis, CA 2016

Poster: S. T. Riahinasab, A. Elbaradei, A. Keshavarz, B. Stokes, L. S. Hirst, Assembling Nanoparticles at the Isotropic to Nematic Phase Transition, International Liquid Crystal Conference, Kent State University, Kent, OH, 2016

Talk: T. Riahinasab, A. Elbaradei, L. S. Hirst, Nano-particles Assembly via Phase Transition of Liquid Crystal Template, APS Far West Section, California State University, Long Beach, CA, 2016

Poster: T. Riahinasab, M. Shah Jahan, B. Walters, Thermoluminescence Observations of X-Irradiated PEEK with DSC Correlation, SFB Annual Meeting & Exposition, Denver, CO, 2014

Poster: T. Riahinasab, M. Shah Jahan, B. Walters, X-ray and UV- Induced Free Radicals in PCU, SFB Annual Meeting & Exposition, Denver, CO, 2014

Talk: T. Riahinasab, M. Shah Jahan, B. Walters, Measurements of Free Radicals in UV- and X-Irradiated PEEK, First International PEEK Conference, Philadelphia, PA, 2013

Poster: T. Riahinasab, M. Shah Jahan, B. Walters, Electron Spin Resonance to Analyze Radiation and Heat Induced Radicals in PEEK, SFB Annual Meeting & Exposition, Boston, MA, 2013

Workshops

• New England Complex Fluids Workshop, University of Tufts, Boston	MA, 2017
• Yosemite Software Carpentry Workshop, University of California, Merced	CA, 2017
• Nanobiofabrication Module, University of California Merced	CA, 2017
• Light/Matter Interactions at the Nano-Bio Interface, University of Illinois at Urbana Champaign	IL, 2016
• Summer School, Soft Solids and Complex Fluids, University of Massachusetts, Amherst	MA, 2015

Associations

• Member of Materials Research Society	2018-Present
• Society of Women Engineers	2017-Present
• Iranian American Physics Network Group	2017-Present
• Member of Topical Group on Soft Matter	2016-Present
• SPIE-International Society for Optics and Photonics	2016-Present
• Member of American Physics Society	2015-Present
• Member of Society for Biomaterial	2011-Present

References

• Dr. Linda S. Hirst. Professor. University of California, Merced. lhirst@ucmerced.edu

• Dr. Michael Scheibner. Associate Professor. University of California, Merced. mscheibner@ucmerced.edu

• Dr. Benjamin J. Stokes. Assistant Professor. University of California, Merced. bstokes2@ucmerced.edu

Abstract

Mesoscale Porous Nanomaterials Templated by a Liquid Crystal Phase Transition

Sheida T. Riahinasab
University of California, Merced, 2019
Committee Chair: Michael Scheibner

Semiconductor nanoparticles (NPs) are an emerging type of material with the potential to revolutionize consumer electronics, and photonics. These particles derive their properties from their small size and can be tuned based on their diameter. Their small size however makes controlling and using them hard, and solving this problem is the focus of this thesis. One way to control such small particles is to orient them spatially using self-assembly. There are two main approaches to self-assembly; top-down assembly and bottom-up assembly. These top-down processes can be extremely expensive, time-consuming, and are typically only be prepared on small scales with specific substrates. Bottom-up processes involve taking colloidal nanoparticles that are manipulated into an array or cluster using a host material such as a liquid crystal (LC) or a block co-polymer, etc. These processes are more cost-effective, can be prepared on numerous substrates, and have the potential for large-scale production.

In this research, I use the nematic liquid crystal, an anisotropic fluid, as a host. The orientation of liquid crystal can be changed by applying an electric field, changing temperature, or applying a magnetic field. NPs used in this research are quantum dots (QDs) that fluoresce and can be tracked to map out their position during the assembly process. The liquid crystal's ordering changes over large length-scales during a phase transition, this alteration of the bulk liquid crystal can be used to assemble the NPs into 3D micron structures. I have developed quantum dots modified with a special mesogenic (liquid-crystal-like) ligand that aids particle dispersion into the liquid crystal host. The mesogenic ligand's flexible arm structure enhances ligand alignment with the local liquid crystal director, enhancing QDs dispersion in the isotropic and nematic phases.

My work has focused on understanding the mechanism of assembly of NPs in 3D, overcoming current limitations and introducing better approaches. This has revolved around understanding how I can control the size of assembled structures based on their applications. My focus here was to study the effect of two main parameters; concentration of nanoparticles in liquid crystal and the system cooling rate through the isotropic to nematic phase transition. I observed that the cooling rate not only changes the size of the 3D structures, but also that it changes the morphology of these 3D structures to give various hollow assemblies made of closely packed functionalized NPs. As the liquid crystal undergoes the phase transition and nematic domains nucleate and grow, NPs tend to remain

in the isotropic regions. A secondary nematic nucleation can then occur inside the shrinking isotopic domains under certain conditions to produce hollow capsules and multi-compartment foam-like materials. The mechanism for this process is explored in this thesis.

As part of this thesis I focused on NP surface modification, which is necessary for the dispersion of NPs in LC as well as a potential tunable mechanism to modulate QD emission spectra (including decreasing Forster Resonance energy transfer (FRET), by varying the spacing between NPs. I modified the surface of NPs using a series of pro-mesogenic ligands to study the effect of NP separation distance on QD emission in drop-cast films. Methods included transmission electron microscopy (TEM), photoluminescence spectroscopy (PL), and small angle x-ray scattering (SAXS).

An important goal of this thesis work was to modify the surface of NPs with mesogenic/ pro-mesogenic ligands. This surface modification makes the particles more soluble in a liquid crystal host. The interaction between ligands also acts to keep the NPs close together and to stabilize the closely packed micron-scale NP structures. As a result of these modifications I demonstrated the ability to control not only the size, but the morphology of NP structures.

Chapter 1

Introduction

1.1 Particle Self Assembly

Self-assembly is a process by which the interactions between particles or molecules cause them to come together and form potentially complex hierarchical structures. This structural assembly is not unique to manmade experiments however, self-assembly is widely observed in biology, from lipid vesicle formation to protein folding. In nature this process allows for precise construction of proteins, from amino acids to human beings from single cells. By better understanding the underlying physics behind self-assembly I can use this powerful concept to construct synthetic materials that are both cheaper, use less material, and are exact on the nanoscale level. This research focuses on using self-assembly to control the construction of quantum dots into larger-scale structures for applications in photonics, electronics, and renewable energy devices. Quantum dots are nanoparticles that have unique optical properties due to their small size and have been building blocks for numerous applications. The main challenge of using these particles comes from the very property that gives them their uniqueness; their small size. Trying to control the assembly and placement of particles that are 60,000 times smaller than a human hair requires novel strategies. In this thesis my solution is to use self-assembly in liquid crystal to control the assembly of nanoparticles into large structures and to manipulate those structures.

In any self-assembled system, the basic components form patterns or structures without external intervention. The resulting structure can have properties of both constituents, or have properties that are entirely different. Such properties can be tuned by changing parameters such as concentration, method of formation, temperature, etc. Self-assembly can be seen in many different areas of science, such as the spontaneous formation of a vesicle by placing lipids in water, liquid crystal formed into a resonant cavity for lasers, and even the formation of planets and starts into solar systems. Self-assembly can be broken down into two main categories; static and dynamic. For static self-assembly, the system is in equilibrium, it is stable and does not transfer energy. The formation of molecular crystals is an example of this type of self-assembly [1,2]. Dynamic self-assembly involves systems which dissipate energy, such as pattern formation in oscillatory chemical reactions due to the competition between the diffusion and reaction [3,4], or the formation of the mitotic spindle by ATP consuming motor proteins. In addition to these two main types, we have two further types of self-assembly, templated and biological self-assembly. Templated self-assembly is when the materials are guided by their interactions with an interface, such as how crystallization on a surface determines the morphology of the lattice [5,6].

In this thesis, I studied the self-assembly of nanoparticles by inserting them into an anisotropic material, more specifically inserting the quantum dots into liquid crystal. Liquid crystals have been used as a host for many materials as they can interact with other particles through multiple mechanisms, leading to a range of resulting constructs [7,8,9].

The most common mechanisms include elastic forces, phase changes, and liquid crystal molecular orientation. How to use these mechanisms to assemble colloidal nanoparticles in liquid crystal has been the focus of much research [10,11,12,13,14,15]. Assembling very small particles (~10 nm in diameter) proves more of a challenge since the particles are subject to Brownian fluctuations, where the size of the particle approaches that of the solvent molecules. Because of the dominant role that particle-particle interactions play, controlling nanoparticles through the molecular orientation or ordering of liquid crystals can be used as it plays a large role in how the liquid crystal interacts with the nanoparticle and vice versa. Briefly as the molecules in nematic liquid crystal tend to be locally orientated with a direction, when nanoparticles are added to the host, they disrupt this packing. Places where the molecules aren't aligned in the same direction, i.e. topological defects [16], accumulate particles and this behavior can be used to assemble them.

Phase transitions represent another self-assembly method used in the work outlined in this thesis. This concept is related to molecular orientation and is a newly discovered phenomenon by the Hirst research group. This technique has led to the formation of new 3D structures of functionalized quantum dots, modified with a suitably designed ligand such as: hollow micro-shells, hollow foams, and hollow networks [17,18,19,20]. When I insert the functionalized NPs into the liquid crystal, their surface anchoring is compatible with one phase of the liquid crystal, i.e. the isotropic phase. If I let the system go through the nematic phase transition, particles would incur an energy penalty to be in the new ordered phase, so tend to stay in the isotropic phase as that phase shrinks. This process is the basis of the 3D structure formation I study here. Such structures can be stabilized by ligand-ligand interactions between the particles. These two methods of self-assembly for nanoparticles using liquid crystal as a host produce stable structures in the LC environment. Here I focused on the phase transition self-assembly. I can control the size and type of the final 3D structures by changing two main parameters: concentration of NPs in liquid crystal and the cooling (quench) rate, as well as controlling the spatial organization of particles by using the droplet of liquid crystal [95].

1.2 Liquid Crystal Materials

In 1887 Otto Lehmann investigated the phase transitions of several cholesterol samples extracted from plants using a polarizing microscope with a heated stage [21]. He observed a cloudy liquid phase after melting a solid substance called cholestery-1 myristate (Figure 1-1a) at 71°C. However, the melted phase was surprisingly not clear, and did not fully transition to the liquid phase. He observed a clear liquid only after continuously heating it up to 85 °C. Otto Lehmann was the first person to propose the liquid crystal state to be a distinct new state of matter following from his experiments with a material that he thought at the time was an imperfect phase transition from crystalline to liquid. In 1888, Friedrich Reinitzer also discovered this new state of matter, when he observed a sample of cholestery-1 benzoate (Figure 1-1b) transition through an intermediate state between liquid and crystal that he called liquid crystal phase [22].

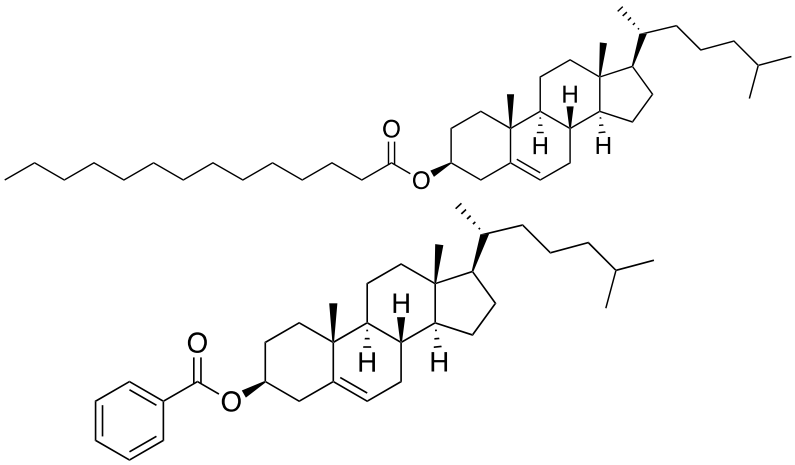

Figure 1-1. Molecular structures of (a) cholesterol-1 myristate and (b) cholesterol-1 benzoate

To understand what a liquid crystal is I need to compare it to the solid and liquid phases. By looking at the phase diagram (Figure 1-2), I can see that the solid crystalline phase molecules are ordered in a lattice and oriented in a specific direction with long range coherency. The liquid phase is isotropic, by which I mean that it has no positional or orientational order. The liquid crystal state, which is often composed of rod-like molecules, is a fluid-like phase, in which the molecules can translate, fluctuate, and rotate freely with some degree of anisotropy. In an anisotropic phase, the optical properties of the system vary with the average alignment with the director.

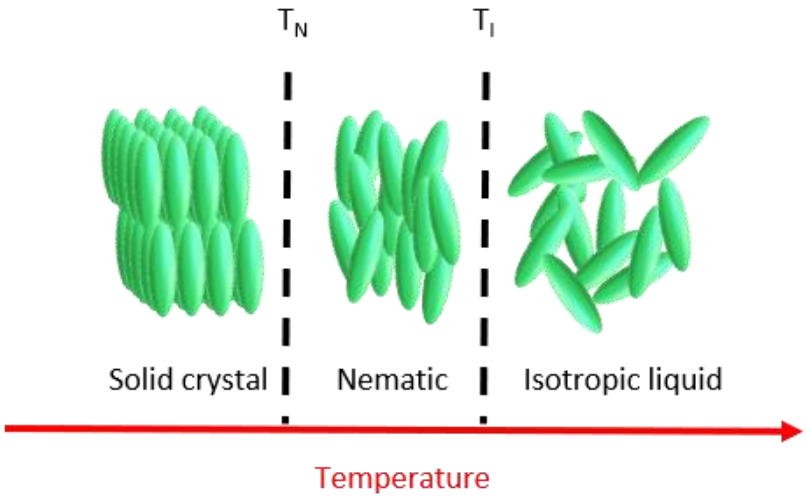

Figure 1-2. Schematic illustration of phase transition behavior and the molecular order of matter discussed in this research. Crystal (has the long range positional and orientational order), liquid (the molecules undergo random motion with molecules axes varying in different direction), and liquid crystals materials. [23]. T_N represents disordering (melting) temperature of the crystalline state, and T_I is the isotropic temperature. Liquid crystal exists in a state between solid and liquid. In addition to these main phases of matter, there are many mesophases or intermediate states.

For the experiments presented in this thesis, I dispersed our QDs into a liquid crystal host, to study the self-assembly of QDs in LC. The nematic to isotropic phase transition occurs near room temperature in the liquid crystal I selected, and the molecular re-ordering can assemble our QDs. When considering a phase of matter, I am interested in the position and orientation of the constituent molecules. The solid crystalline phase possesses positional order, which means molecules must occupy only certain positions in a crystal lattice, over large length scales. In the liquid phase, the molecules must be adjacent to each other but are free to move around and have no orientational or positional order. Liquid crystals have orientation order at short range length scales. When a solid transition to an isotropic phase, both orders will disappear. If the material exhibits a liquid crystal phase, even though molecules in the liquid crystal state may lose their long-range positional order, they still retain their orientation order, and perhaps short-range positional order.

The liquid crystal state is a stable thermodynamic phase between the liquid and crystalline phases, with both fluid-like properties and short-range molecular order. Its complicated behavior can be understood simply from the molecular shape. Liquid crystals can have many different phases depending on molecular shape and orientation, principally I can simplify liquid crystal molecules into two main shapes; rods and disks [24,25]. While these seem like simple shapes, these anisotropic molecules can display a wide variety of phases (i.e. nematic, smectic and cholesteric) based on the molecular arrangement and ordering. For this research I will focus on the Nematic phase. [26]. Particles are anisotropic when each molecule possesses a directional property. One of the most well-known liquid crystal phases (and the one used in this research), is the nematic liquid crystal. A common nematic liquid crystal used in many experiments is 4-cyano-4'-pentylbiphenyl (5CB). Figure 1-3 shows the molecular structure of 5CB. 5CB is nematic at room temperature, and on increasing temperature, 5CB will go through the nematic-isotropic phase transition at 35 °C [27].

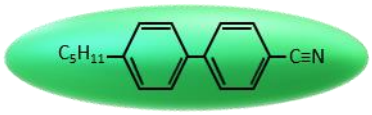

Figure 1-3. Molecular structure of 4-cyano-4'-pentylbiphenyl. Alternatively known as 5CB, is a material which has a rod-like shape and in bulk exhibits the nematic phase at room temperature.

In the nematic phase, all the molecules tend to, on average, locally align in the same direction. I define this local alignment using the director ***n***, a vector that is the average orientation of the molecules and their nearest neighbor's orientational vector. [28] (Figure 1-4), a bulk, unconfined sample of nematic material will tend to have a random molecular orientation over the whole, but locally will have orientational order.

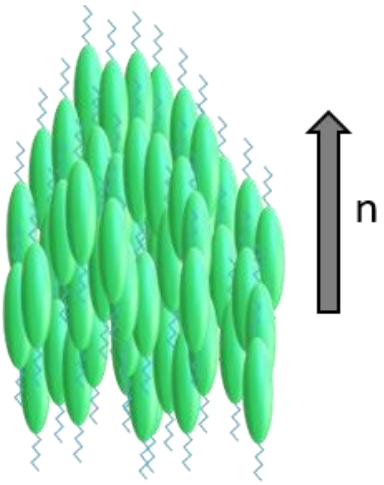

Figure 1-4. The Nematic liquid crystal phase. The molecules locally orient in a common direction, defined by the director *n* (The director shows the local average orientation of the molecules, which tend to point in the same direction as their neighbors)

Another important type of liquid crystal phase is smectic liquid crystal. Smectics have an additional degree of translational order (1D positional order), which it isn't present in the nematic phase. Smectics are like nematics in terms of molecular orientation but differ in molecular position. Smectic liquid crystal molecules tend to arrange themselves in planes or layers of rod-like molecules stacked on one another [29]. Among the many types of smectic materials, there are two main classes: 1) Smectic A (SmA) where the nematic director in each layer is oriented parallel to the layer and 2) Smectic C (SmC), where the molecules are arranged as in SmA, except that the director tilts away from the layer normal. (Figure 1-5)

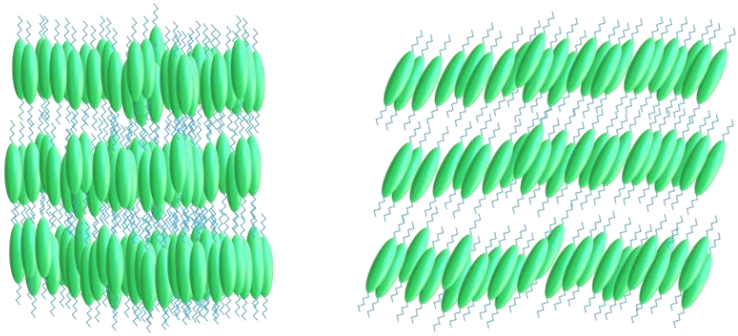

Figure 1-5. Schematic orientation of molecules in the smectic C and smectic A phases.

Another common type of liquid crystal is a cholesteric liquid crystal, also known as the chiral nematic phase. In a cholesteric phase, molecular orientation varies continuously as you go through the material (Figure 1-6). The distance it takes the molecules undergo one full rotation is called the pitch. The pitch of a cholesteric liquid crystal can change based on properties such as temperature.

Figure 1-6. Illustration of the ordering of molecules in a cholesteric LC. The nematic director twists along an axis perpendicular to the long molecular axis.

1.3 Nematic Liquid Crystal

In this research I focused on the nematic phase, which is the most well-known and widely used liquid crystal phase. Nematic is derived from the Greek word for "thread". Nematic liquid crystals are known to easily align with applied electric fields [30,31]. This is due to their dielectric anisotropy. In an electric field, an electric dipole forms long the length of the molecule. This property has led the nematic to be used for a variety of applications, such as lenses [32], optical switches [33], and displays [34]. Nematic liquid crystals are spatially non-polar. That is, there is no defined difference if a molecule is pointed in the +x direction or -x direction. Since there is no defined spatial polarity, liquid crystals have their spatial directions characterized by an order parameter. This order parameter is a scalar number that relates the directions of the liquid molecules to a preferred direction. Liquid crystals also experience diverse types of deformation, so I need a way of characterizing these deformations. Finally, liquid crystals are very sensitive to temperature, i.e. liquid crystal molecules are subject to thermal fluctuations on the order of kT (Where k is the Boltzmann constant).

1.4 Nematic Orientational Order

Nematic orientation is characterized by the scalar order parameter S, a measure of how molecules are locally aligned with the director. Nematic liquid crystals tend to, on average, align in a particular direction, defined as the director. While there is an average direction, since the liquid crystal is in a fluid phase and nematic molecules can freely move and fluctuate, individual molecules will make an angle with respect to the director's axis. This variation in molecular angle is characterized by the nematic order parameter, S (which indicates the degree of orientational order of LCs [35], which measures how the molecules are aligned with the director. Nematic molecules do not fully line up with the director due to thermal fluctuations [36], so the scalar order parameter is a way of accounting for those thermal fluctuations. The scalar order parameter for the nematic phase represents the average molecular orientation around the director, θ and is defined as,

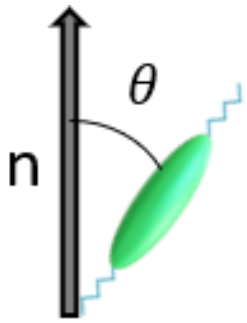

Figure 1-7. Represents the angle between a liquid crystal molecule and the director.

$$\boldsymbol{S = \frac{1}{2} < 3\cos\theta^2 - 1 >} \qquad \textbf{Equation 1-1}$$

where θ is the angle between the long axis of an individual LC molecule and the nematic director ***n***. (Figure 1.7). Equation 1-1 represents how to quantify the scalar order parameter and the angular brackets represents an average. If I decrease the temperature from an isotropic (liquid) phase to a nematic phase, the molecules will go from no positional and orientational order to only an orientational order, in which the order parameter changes from S = 0 when the molecules are in an isotropic (liquid) phase to 0 < S < 1. If S = 1, the molecules are perfectly aligned parallel to each other. In the nematic LC phase, the value of the order parameter, S, for most LCs is generally in the range between 0.4 and 0.65 [37].

1.5 Phase Transitions

5CB is a thermotropic liquid crystal, meaning that its phase transitions are induced by changing temperature. When 5CB goes from the isotropic to the nematic phase, it goes through a first order phase transition. A first order phase transition occurs when the order parameter is discontinuous across the phase boundary at a specific temperature. At a first order phase transition point, phases A and B will coexist during the period of transition. By adding heat energy to increase the temperature of a system, the free energy increases. Since systems trend toward their lowest free energy state, there will come a point where the system spontaneously reorders itself to decrease this energy and this is considered a first order phase transition. Considering phase transitions in liquid crystals and their order parameters, the order parameter is zero in the isotropic liquid phase because the molecules are randomly oriented at different directions then average value is zero. For crystalline structures I have a value of one for the order parameter, since the molecules exhibit long range order. When material go through the I-N phase transition, the molecules locally align with each other, increasing their order parameter.

The following plot (Figure 1-8) shows the first order phase transition, as you can see if your system is at the nematic phase and you start to increase the temperature the order parameter will slightly decrease until it reaches a temperature T_{NI} where the system

goes from nematic to isotropic phase. Molecules then randomize and the order parameter decreases to zero, creating a discontinuous plot of order parameter vs. temperature. I can observe this phase transition using two techniques: polarized optical microscopy to directly observe the N-I phase transition with birefringence and differential scanning calorimetry.

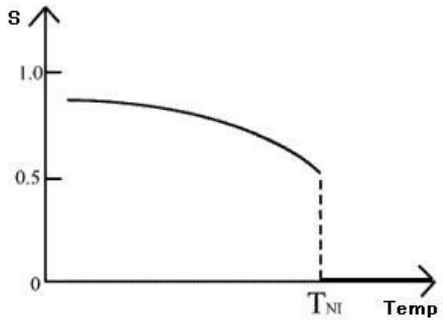

Figure 1-8. A first order phase transition; plot of order parameter vs. temperature showing the discontinuity at transition temperature T_{NI}.

1.6 Topological Defects

By now I have enough ingredients to discuss topological defects in the nematic phase. Liquid crystals are often composed of rod-like molecules and by changing temperature, or applying an external electric field, I can change their degree of positional and orientational order. The nematic phase normally doesn't possess a director that points in the same direction at all points (uniform alignment). In certain regions it might point in one direction and elsewhere it might point in a different direction. In such a situation, there is typically a location between these two misaligned regions where the director changes over a very short distance. It is impossible to define the direction that the director is pointing at the place of abrupt change, so this place represents a defect; a line or point where the director's structure changes abruptly.

Defects of various types naturally occur in various mesophases and I can observe them in the polarizing microscope as defect textures. To look at defects present in a liquid crystal, I use an optical microscope and place the material between crossed polarizers. The director points in different directions at different sites within the sample. Areas where the director orients parallel or perpendicular to the axes of the polarizers appear dark, while areas where the director makes an angle from zero to 90 degrees to the polarizers' axes appears bright (Figure 1-9). This image shows that there are many places where image intensity changes abruptly, indicating that the orientation of the director must also change abruptly. These lines are called disclinations and are located where the director is undefined (i.e. it points in many directions within an extremely small area). Such topological defects, areas of orientational frustration in a liquid crystal, can occur spontaneously in a bulk nematic as the material is cooled through the isotropic to nematic phase transition, or because of specific confining surface treatment or geometric restriction [16].

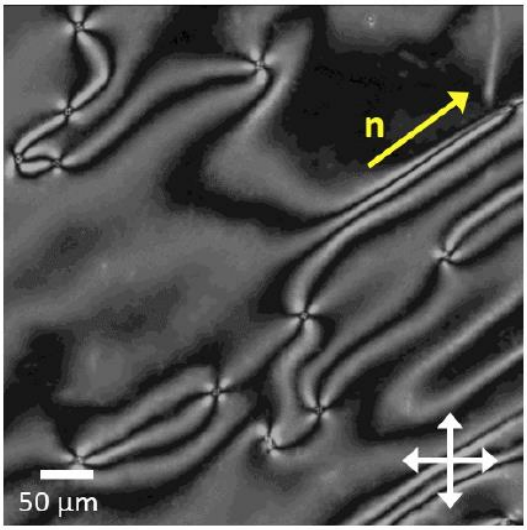

Figure 1-9. Schlieren texture in a nematic liquid crystal imaged using polarized optical microscopy [38]. The cross sign represents the orientation of the cross polarizers and if the direction of director is in direction of any polarizers then I see black (extinction). For the lighter areas the director (*n*) lies at an angle between the polarizers, revealing the texture.

Another reason to understand defects in a liquid crystal is that they affect the optics, contrast, and performance of display devices. So, for removing or reducing defects in liquid crystal cells, understanding the structure of defects becomes very important. Defects can occur in the following situations:

1) During symmetry breaking phase transitions

2) Under an external field

3) Because of impurities or dispersions of particles

These defects appear in the liquid crystal as either point defects or line defects depending on the liquid crystal's average molecular shape. A point defect is one where the directions of rod-like molecules are pointing in different directions from around that point. If I have spherical droplets of nematic liquid crystal, based on the direction of the liquid crystal director inside of droplet, I will have two configurations, depending on whether the liquid crystal prefers to align parallel or perpendicular to the surface of the droplet. In the case of parallel alignment, I have two-point defects, while for perpendicular alignment I have one-point defect in the center of the droplet (Figure 1.10a). Another example of a point defect is in the thin capillary tube where molecules orient themselves perpendicular to the cylindrical surface of tube (Figure 1.10b).

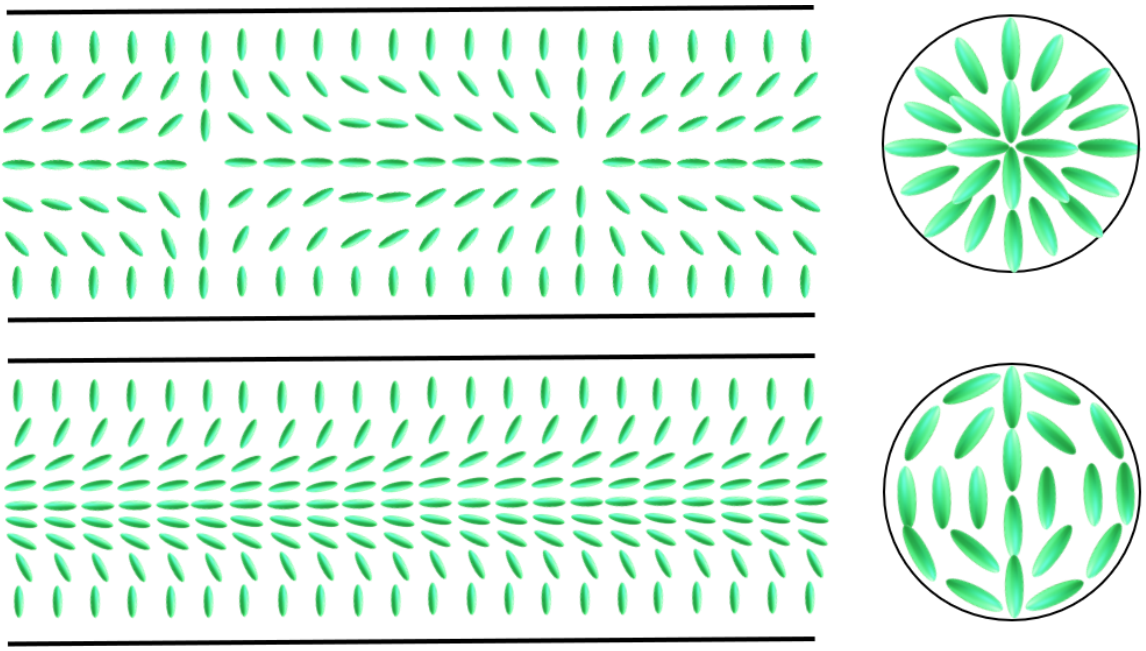

Figure 1-10. a) Defects in a capillary tube. Two-point defects are shown, one of which is opposite to the other b) the two possible director configurations inside the droplets [39].

Another possibility for the capillary tube with direction perpendicular to the surface is a line defect along the center of the tube. Many different disclinations are possible. To classify them, I examine the director's configuration in a plane perpendicular to direction of molecules and attribute a "charge" to them. (Figure 1.11). I will now discuss how I label topological defects and distinguish between them. To distinguish different topological defects, I use the Burgers circuit [40]. I will impose a circuit around a topological defect in Figure 1-12.

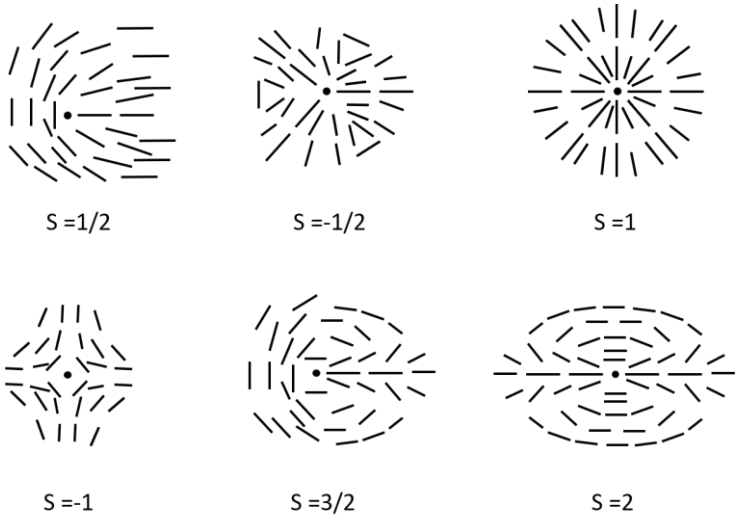

Figure 1-11. Six different types of point defect [39].

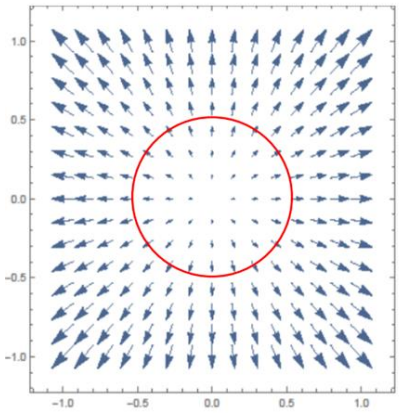

Figure 1-12. Burgers circuit around a defect point. The circuit is followed around in the counterclockwise direction. In this case we have a +1 defect.

I can identify the type of defect present by giving the defect a topological charge. To obtain this charge, I follow the circuit around the counterclockwise direction and see how the director rotates while following the path. In Figure 1-13, beginning on the right side of the circuit, I follow the director direction as I follow a circle from north, west, south, and back to east (counterclockwise). The director makes one full rotation as I follow the circuit in this direction, so I label this defect as having a +1 charge. [41]. In comparison, if the director rotates 360 degrees in the clockwise direction while I travel 360 degrees in the counterclockwise direction, I produce a -1 defect.

Each defect is therefore assigned a number, which shows the strength of disclination, and the plus and minus signs indicate which disclinations are opposite in charge. For example, textures around S=+1 and S=-1 defects look the same (dark) between crossed polarizers. They can be distinguished by slightly rotating the polarizer, because, as you can see from the figure, the dark strip rotates in the opposite direction for defects of the opposite sign (Figure 1-12).

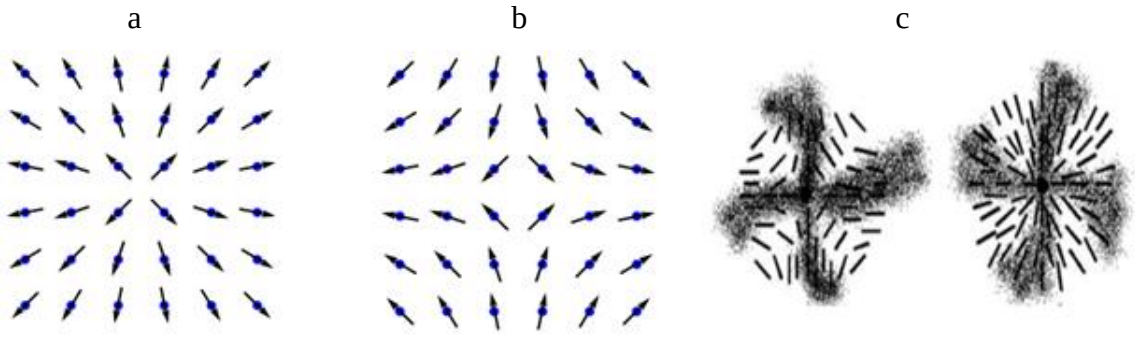

Figure 1-13. (a-b) Different director orientations for +1 and -1 topological defects, (c-d) next to their appearance under the polarizing microscope with slightly uncrossed polarizers [42].

To look at defects present in a liquid crystal, I use a light microscope and put the sample between the crossed polarizers. The director points in different directions at different points within the sample. Areas where the director orients parallel or perpendicular to axes of polarizers appear dark, while areas where the director makes an angle with polarizers' axes appears bright. There are many places where brightness changes abruptly, indicating that the orientation of the director must also change abruptly. These disclination lines are located where the director is undefined, since it points in many directions within an extremely small region (Figure 1-13).

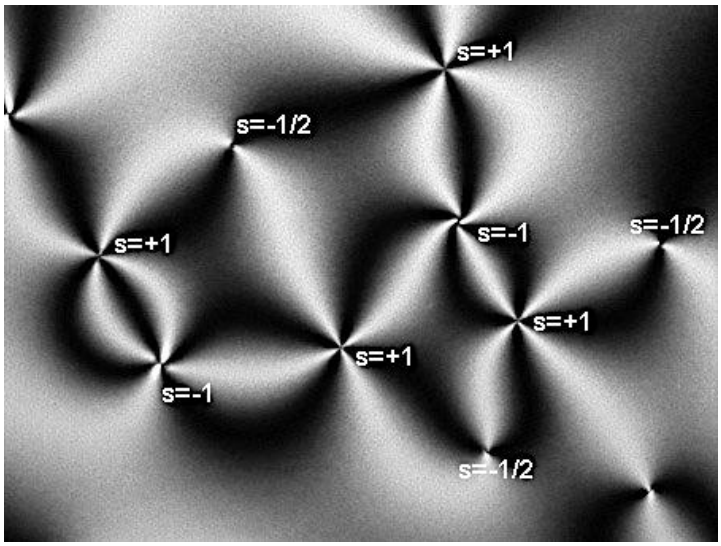

Figure 1-14. **Schlieren texture in nematic liquid crystal including defects labelled by their topological charge [43].**

1.7 Nanoparticles

Nanoparticles are the most fundamental building block for fabricating nanostructures. They are a relatively new form of material with many applications depending on their properties, although their uses in colored glasses do date back to the ancient Greeks. NPs are already being used commercially from applications as varied as in catalytic converters in cars to domestic skin care products. Nanoparticle sizes can range from 1 to 500nm, with a vast array of shapes possible - from synthetic rods and dots to the varied forms of virus capsid shapes [44].

.

There are three main categories of synthetic nanoparticles: magnetic, semiconducting, and metallic. All these types of NPs have shown potential for practical applications due to their physical properties. For example, semiconducting and metallic NPs are good for medical and electronic applications because of their unique optical properties. Metallic NPs have different chemical and physical properties compared to bulk metals. They have higher surface area, lower melting point, higher mechanical strengths, better magnetization properties, and specific optical properties compared to bulk metals. The many physical differences between nanomaterials and their bulk analogs are due to

their small size. This increases their relative surface area, produces quantum confinement effects, and produces for fast diffusion in solution. With these properties, NPs have had significant impact on a range of application such as modifying vehicles for gene and drug delivery [45,46,47], biotechnology [48], developing electronic storage systems [45], magnetic separation, and targeted drug delivery [46,47]. Semiconducting NPs, which are the main NPs used in this thesis, are small crystalline particles, which have optical as well as physical properties that are conserved across other small sized nanoparticles. The optical and electronic properties of semiconductor NPs are size-dependent [49,50,51]. They have narrow emission and broad absorption profiles with a high quantum yield [52,53]. This makes them favorable for sensing, labeling, and tracking applications *in vivo* and *in vitro*. Another important optical property of semiconductor NPs is their resistance to photo bleaching when compared to organic fluorescent dyes [54,55]. Semiconductor nanocrystals are typically fabricated as colloids suspended in solution, electrostatically defined, strain defined, cleaved edge over growth, and as epitaxial structures grown on solid crystalline substrates.

1.8 Quantum Dots

Colloidal QDs are nano-sized semiconductor particles/crystals that are chemically grown in solution. Since they are chemically synthesized, they can be manufactured at sizes less than 50 nm in large cost-effective batches. Colloidal QDs are fluorescent because their small size induces quantum confinement effects, meaning the optical property of NPs is size-dependent (equation 1-2). QDs have narrow emission and broad absorption peaks, making them useful for optoelectronic applications [56,57,58] such as solar cells and light-emitting diodes. Additionally, these properties have very broad application prospects as biological fluorescent probes and functionalized particles. Therefore, QDs have been widely used in the field of life sciences as fluorescent markers [59,60]. Figure 1-15 shows a transmission electron microscope (TEM) image of QDs. In the next section, I briefly review the basic properties of QDs.

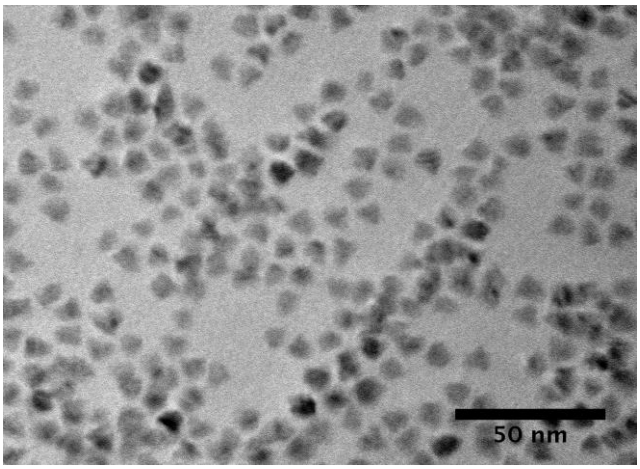

Figure 1-15. Transmission electron Microscopy (TEM) image of quantum dot nanoparticles

1.9 Optical Properties of Quantum Dots

Due to quantum confinement effects, the optical properties of colloidal QDs are governed by their size. When semiconductor QDs at a specific size are excited by a light at a known wavelength, the photons are absorbed. Individual atoms have discrete electron orbitals that require electrons to have a certain quantized energy. When atoms come together to form the crystal, these orbitals interact and overlap. The spatial over-lapping of the atomic orbitals leads to the formation of energy bands of the allowed electron states (The conduction band and the valence band) separated by a forbidden energy gap called the band gap [49]. Semiconducting properties of nanoparticles arise from the periodic arrangement of atoms in a crystalline lattice [59] (Figure 1-16). An electron excited from the valence band by the absorption of a quantum of light moves to the conduction band, leaving a positive charge (a hole) [61]. Electrons occupy the material in distinct bands of energy levels, but because they are fermi particles, they can only occupy quantum states distinct from one another. The lowest filled state is called the valance band. When an electron is imparted enough energy to leave the filled state it is excited to the conduction band, a region unfilled by electrons. The absorbed photon can excite an electron by a discrete amount of energy. If this discrete energy is greater than the band gap, the electron will move to the conduction band. When the electron drops back to the valence band to recombine with the hole, after losing energy by various dissipative mechanisms, it emits a photon with less energy and a longer wavelength. As the size of the QD increases the bandgap energy decreases. Figure 1-17 shows the effect on the emission spectrum due to the change in bandgap energy with change in size.

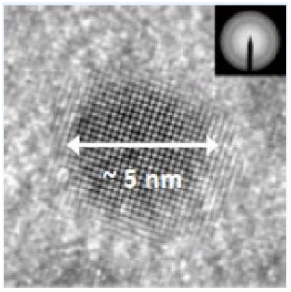

Figure 1-16. Transmission electron microscope image of a quantum dot [62].

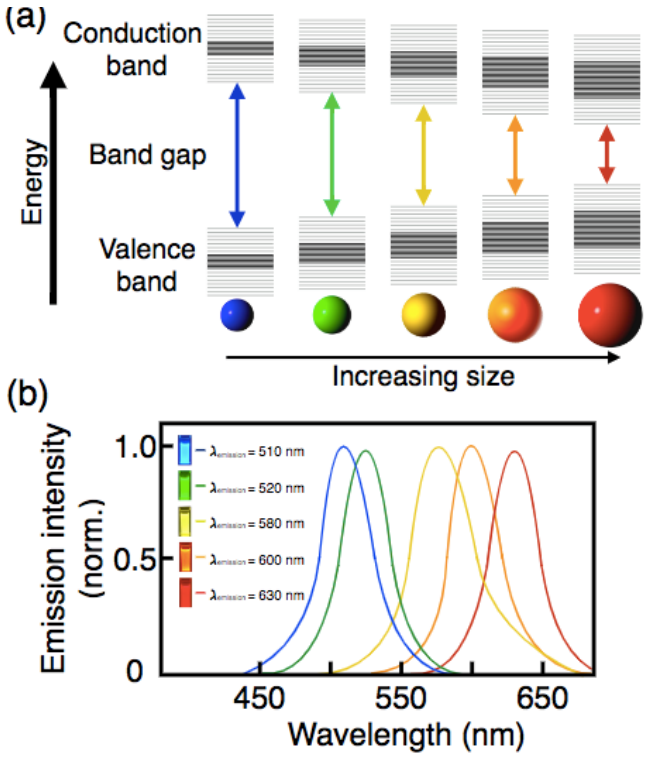

Figure 1-17. a) Increasing the size of quantum dots, the semiconductor band gap decreases. Splitting the energy level due to the quantum confinement effect b) emission spectra of different size of QDs [63].

The Brus equation [64] shows the emitted photon energy from a QD. This equation, gives an approximate relationship between the bandgap energy and particle size [49],

$$E_{gap}^{QD} \approx E_{gap} + \frac{\pi^2 \hbar^2}{2L^2}\left(\frac{1}{m_e} + \frac{1}{m_h}\right) \qquad \textbf{Equation 1- 2}$$

where E_g is the bulk band gap, h is Planck's constant, r is the particle (QDs) radius, m_e is the effective mass of the electron and m_h, is the effective mass of a hole.

The energy levels in a QD can be modeled like a particle-in-a-box, in which the different energy states depend on the size of the box. The particle-in-a-box model considers an arbitrary particle of mass m in a potential well of length L. where the potential is:

$$V(x) = 0 \quad \text{for } 0 < x < L \qquad \textbf{Equation 1-3}$$
$$V(x) = \infty \quad \text{for } x < 0 \text{ and } x > L$$

Solving the Schrodinger equation with boundary condition results in wave functions:

$$\psi_n(x) = \sqrt{2/L}\sin\left(\frac{2\pi n}{L}\right) \qquad \textbf{Equation 1-4}$$

Where n identifies the energy level. The energy of the particle is therefore given by:

$$E_n = \frac{\pi^2 \hbar^2}{2mL^2} n^2 \qquad \textbf{Equation 1-5}$$

Note that the energy of the particle is proportional to $1/L^2$ and is thus strongly dependent on the size of the particle.

The Brus equation clearly shows that the band gap is a function of the radius of the QD. Thus, as QD size decreases, the band gap of the particle increases. By using the Brus equation, I can relate this energy to the wavelength of emitted light by $E = \frac{hc}{\lambda}$, and see that larger QDs will emit light at longer wavelengths when excited. Figure 1-17b shows absorption spectra for CdSe QDs, with sizes ranging from 1.7 nm to 15 nm along with sharp inter-band transitions. The graph illustrates how the bandgap increases, as evidenced by the blue shift of the absorption curve with decrease in QD size. More precisely, size variation of CdSe quantum dots can tune the bandgap from 3.1 eV to 1.8 eV, which corresponds to a shift in wavelength from 400 nm to 700 nm. Therefore, tuning the size-dependent bandgap of QDs brings the benefits of fluorescence emission tunability. This property makes them good candidates for self-assembly into tunable new structures.

The QD's broad absorption spectrum and narrow emission spectrum gives it unique utility compared to most organic dyes in preventing emission bleed over. In general, the optical properties of QDs can be tuned by changing the size, for example the narrow fluorescence emission spectra of QDs scales from a 1 nm radius emitting a blue photon and a 6 nm radius emitting a red photon. The fluorescence intensity of QDs is 20 times that of the well-known organic fluorescent dye, Rhodamine 6G, with a greatly enhances stability [65]. Another significant optical property of QDs when compared with organic dye is their high capacity to resist photobleaching [65]. Photobleaching is a phenomenon that decreases the emission intensity due to optical excitation. The photobleaching rate of organic fluorescent dyes is very fast - on the order of minutes. On the other hand, the photobleaching rate of QDs is much lower, as their larger size makes them more robust compared to single molecule structures. Utilizing this property, colloidal QDs have been successfully used for labeling cells, organs, and proteins, allowing the observation of emission over long time scales. [66,67].

This chapter has presented a general overview of semiconductor nanoparticles (in particular QDs) and liquid crystals. Both have unique and interesting properties, liquid crystals themselves have been an important tool in the field of self-assembly since I am able to control factors such as molecular orientation, phase change behavior, and various other parameters. In Chapter 2, more focus will be placed on the interaction between NPs and liquid crystal including relevant optical properties of liquid crystals and their usage in experimental techniques.

I will focus on the theory behind liquid crystal and QDs in Chapter 2. Chapter 3 explains the different experimental methods used in this work in detail. Chapter 4 will talk about the library of pro-mesogenic ligands, ligand exchange and characterization. Chapter

5 describes the mechanism of assembly of NPs into 3D structures and parameters to control their size.

Chapter 2

Theory

2.1 Orientational Order Parameter

In Chapter 1, I reviewed a simple equation for quantifying the local orientation of an anisotropic material called the order parameter. In this chapter I will discuss from first principles why rod-like molecules align parallel to each other and explain the physics of the nematic liquid crystal phase. In order to understand the liquid crystal phase a material's orientational order is our starting point. To quantify this orientation, I take the average direction of long axis of the rod like molecules, which I called the director, and measure the average angle between it and each constituent particle. To describe the orientation of a rigid elongated liquid crystal molecule, I define three axes: long molecular axis and two short axes perpendicular to the long molecular axis. As you can see from figure 2.1, there is no preferred direction for the short axes, so nematic liquid crystal is uniaxial.

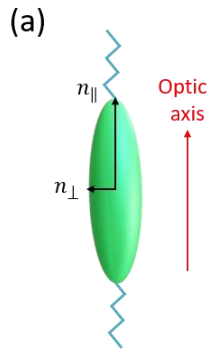

Figure 2-1. A rigid rod-like shape of an elongated liquid crystal molecule with three axes.

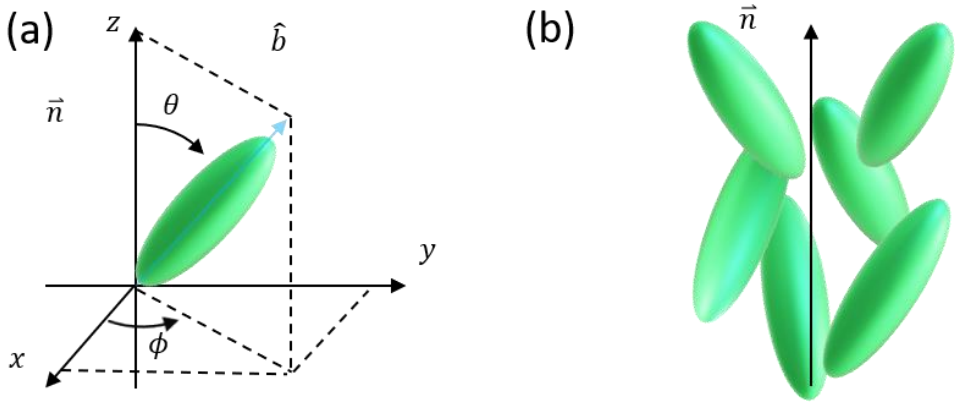

Figure 2-2. Schematic diagram showing the orientation of a rod like molecule

For the uniaxial liquid crystal, I only consider the orientation along the long axis molecule. The orientation of a rod like molecule can be represented by a unit vector $\hat{b}$ which is attached to the molecule and parallel to long axis. For nematic liquid crystal I define the liquid crystal director with unit vector $\vec{n}$ which is the average direction of long molecular axes. Figure 2-2 represents the 3D orientation of unit vector $\hat{b}$ with azimuthal angle ϕ and polar angle θ where the unit vector $\vec{n}$ chosen to be in z direction. In general, the orientation of a unit vector $\hat{b}$ is specified by an orientational distribution function k (θ,ϕ). For isotropic state, the k (θ, ϕ) = constant since the unit vector $\hat{b}$ has equal probability of pointing in any direction. For uniaxial liquid crystal, there is no preferred orientation in the azimuthal direction, thus k is only function of polar angle θ, k=k (θ).

I define the order parameter to quantitatively specify the orientational order. The order parameter is defined in a way that when the temperature is high the value becomes zero (for unordered phase) and when the temperature is low the order parameter is non-zero (ordered phase) (See figure 2.3). This concept is like the orientation magnetic moments in ferromagnetism, where the magnetization can be summarized by M, and represents the average alignment of the individual dipoles. Even though orientation of the order parameter matters in magnetism, it does not play role in nematic phase

$$< \boldsymbol{cos\theta} > = \frac{\int_0^{\pi} \boldsymbol{cos\theta f(\theta) sin\theta d\theta}}{\int_0^{\pi} \boldsymbol{f(\theta) sin\theta d\theta}} \qquad \textbf{Equation 2-1}$$

θ is the angle of long axis of molecule with respect to the director and $\cos\theta$ is the first order Legendre polynomial. For the nematic phase the probability of molecule oriented at angle θ and π-θ is the same, k (θ)= k(π-θ) so the ,$\langle \cos\theta \rangle = 0$ and for isotropic phase the molecules are randomly oriented and , $\langle \cos\theta \rangle = 0$; therefore the first-order Legendre polynomial provides no information about the orientational order parameter. I consider the second-order Legendre polynomial:

. $$\boldsymbol{S = < P_2(cos\theta) > = \frac{1}{2}\,(3cos^2\theta - 1) = \frac{\int_0^{\pi} \frac{1}{2}(3cos^2\theta - 1) f(\theta) sin\theta d\theta}{\int_0^{\pi} f(\theta) sin\theta d\theta}} \qquad \textbf{Equation 2-2}$$

For the isotropic phase f (θ) = constant, for the nematic phase the orientational distribution function depends on θ. For a perfectly ordered nematic phase f (θ) = δ (θ) then,

$$\boldsymbol{sin\theta\delta(\theta) = \begin{cases} \infty & \theta = 0 \\ 0 & \theta \neq 0 \end{cases}} \qquad \textbf{Equation 2-3}$$

$$\boldsymbol{\int_0^{\pi} \delta(\theta)\ sin\theta d\theta = 1}, \qquad \textbf{Equation 2-4}$$

, and the order parameter $S = 1$.

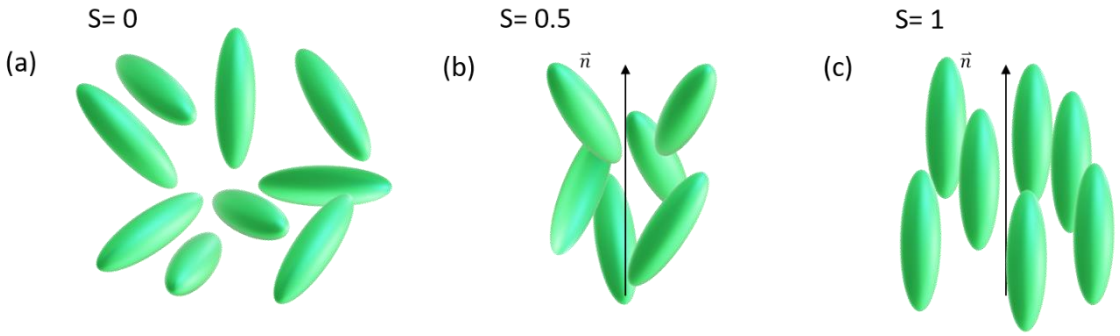

Figure 2-3. Schematic of order parameter for different state; isotropic (a), liquid crystal (b), and crystal (c)

2.2 Elastic Properties of Nematic Liquid Crystal

In a liquid crystal the local director direction, ***n*** may change spatially due to the external fields or confinement. The spatial variation of this director represents a deformation in the molecular structure and incurs an energy cost. When orientational variation in the LC occurs on length scales much greater than the molecular size, I can describe this in a similar way to elastic solids, using a contuum elastic theory. The elastic energy required to deform the LC is proportional to square of the spatial displacement, in a manner similar to Hooke's Law. When I distort LC in the nematic phase, the director can be deformed in three ways. These deformations are called either twist, bend, or splay. Figure 2-4 shows the three types of deformation. These three deformations are better understood if I consider the director to be in cylindrical coordinates. In this coordinate system the director is along the z axis. The director can tilt in either the radial direction ρ as shown in (Figure 2-4 a) or the director tilts toward the azimuthal direction ϕ as shown in (Figure 2-4 b) or it can both tilt in ρ while it being displaced in the z direction (Figure 2-4 c).

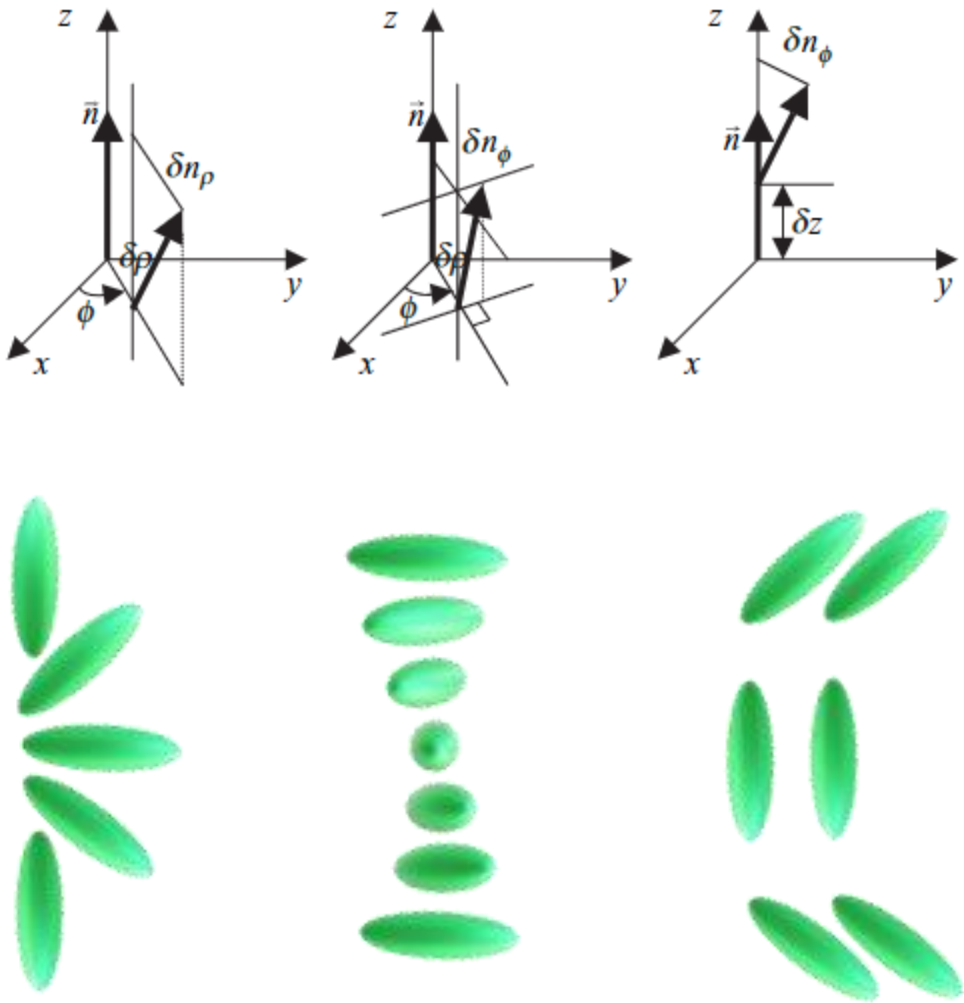

Figure 2-4. These are most commonly known as splay, twist, and bend. Splay occurs when molecular orientation is perpendicular to a gradient direction. Twist occurs when molecular orientation changes as you travel through different axis. And bend occurs when molecular orientation is parallel to a gradient direction.

I can model the director using equation 2-4 in order to consider our splay deformation. For first deformation (Figure 2-4a) I have infinitesimal changes in ρ and z.

$$\boldsymbol{n_z = \hat{z}} \qquad \textbf{Equation 2-5}$$

$$\boldsymbol{\vec{n}\,(\delta\rho,\ z=0) = \delta n_\rho\,(\delta\rho)\,\hat{\rho} + [1+\delta n_z\,(\delta\rho)]\,\hat{z}} \qquad \textbf{Equation 2-6}$$

Where the change, (δ), in n_ρ, or n_z is much less than one. Because $|\vec{n}|^2 = n_\rho^2 + n_\phi^2 + n_z^2 = (\delta n_\rho)^2 + (1+\delta n_z)^2 = 1$, then $\delta n_z = -(\delta n_\rho)^2/2$, where δn_z is a higher order term and can be left

out. To find the change in direction I take the partial variation $\delta n_\rho/\delta\rho$ and consider that the units are the same as energy, and this term is therefore the energy of elastic deformation

$$\boldsymbol{f_{splay} = \frac{1}{2} K_{11} (\frac{\partial n_\rho}{\partial n_\rho})} \qquad \textbf{Equation 2-7}$$

Where K_{11} is the splay elastic constant. For the second deformation (figure 2-4 b), called twist, the director varies in azimuthal angle, I can write the vector as:

$$\boldsymbol{\vec{n}\big(\,\delta_\rho, \emptyset, z = 0\big) = \,\delta\rho_\emptyset(\delta\rho)\hat{\emptyset} + [1 + \delta n_z(\delta\rho)]\hat{z}} \quad \textbf{Equation 2-8}$$

Since δn_ρ is much less than 1 and using the equivalent method for equation, $\delta n_z = -(\delta n_\emptyset)^2/2$ I can find elastic energy by again seeing its change in direction and taking the partial range, $\partial n_\emptyset/\delta\rho$ that gives us equation 2-9.

$$\boldsymbol{f_{twist} = \frac{1}{2} K_{22} (\frac{\partial n_\emptyset}{\partial \rho})} \qquad \textbf{Equation 2-9}$$

Where K_{22} is the twist elastic constant. When moving in the z direction, there is only one possible mode of variation, as shown in figure 2.4c, which is called bend. The director at (ρ=0,ϕ, δz) is

$$\boldsymbol{\vec{n}(\,\rho = 0, \emptyset, \delta z) = \,\delta n_\rho(\delta z)\hat{\rho} + [1 + \delta n_z(\delta z)]\hat{z}} \qquad \textbf{Equation 2-10}$$

Where δn_ρ is much less than 1 and $\delta n_z = -\big(\delta n_\rho\big)^2/2$, is a higher order term which can be neglected. Note that when ρ=0, the azimuthal angle is not well defined, and I can choose the coordinate such that the director tilts toward the radial direction. The corresponding elastic energy is

$$\boldsymbol{f_{bend} = \frac{1}{2} K_{33} (\frac{\partial n_\rho}{\partial z})} \qquad \textbf{Equation 2-11}$$

Where K_{33} is the bend elastic constant. Putting all the three terms together, using various vector operator identities, I obtain the elastic energy density:

$$\boldsymbol{f_{elastic} = \frac{1}{2} K_{11} (\nabla . \vec{n})^2 + \frac{1}{2} K_{22} (\vec{n} . \nabla \times \vec{n})^2 + \frac{1}{2} K_{33} (\vec{n} \times \nabla \times \vec{n})^2} \quad \textbf{Equation 2-12}$$

This elastic energy term is called the Oseen-Frank energy where K_{11}, K_{22}, and K_{33} are referred to as the Frank elastic constants [68]. Experiments show that usually the bend elastic constant K_{33} is the largest constant and the twist elastic constant K_{22} is the smallest. As an example, at room temperature the liquid crystal 5CB has the elastic constants: K_{11}= 0.64 x 10^{-11} N, K_{22}= 0.3 x 10^{-11} N, and K_{33}= 1x 10^{-11} N.

When I insert QDs in a liquid crystal, the phase of liquid crystal will guide the motion of QDs. For the majority of experiments in this thesis, I inserted the QD in isotropic liquid crystal and, as expected, don't disperse very well, they tend to cluster together [16]. If I place nanoparticles in the liquid crystal they would disturb the order of the LC, creating more defects and raising the energy of the system. Because of this, nanoparticles tend to gather at topological defects (via Brownian motion) to reduce the net energy cost of

insertion per QD. Nanoparticles are driven to defect points due to the elastic forces, and this elastic deformation is governed by the Frank elastic energy (Equation 2-12). Such effects make uniform particle dispersion in LC a serious challenge. As we will see in the following chapters, and in our previous work, this problem can be addressed by modifying the surface of QDs with a mesogen-like ligand which is similar in shape to the liquid crystal (5CB).

2.3 Propagation of Light in Anisotropic Optical Media

When I consider light propagation through a material, I can model it as electromagnetic waves [69,70,71]. These electromagnetic waves can break into four fundamental components: electric field, electric displacement, magnetic field, and magnetic induction. Those quantities are vectors. In a medium where light passes through the material, I can relate the electric displacement to the electric field by

$$\vec{\boldsymbol{D}} = \boldsymbol{\varepsilon_0}\overleftrightarrow{\boldsymbol{\varepsilon}}.\vec{\boldsymbol{E}} \qquad \textbf{Equation 2-13}$$

Where ε_0=8.85 × 10^{-12} F/m and $\overleftrightarrow{\varepsilon}$ is the dielectric tensor of the medium. The magnetic induction is related to the magnetic field by

$$\vec{\boldsymbol{B}} = \mu_0\overleftrightarrow{\mu}.\vec{\boldsymbol{H}} \qquad \textbf{Equation 2-14}$$

Where μ_0=4π×10^{-7} H/m is the permeability of vacuum and $\overleftrightarrow{\mu}$ is the permeability tensor of the medium. LCs are non-magnetic media, with permeability close to 1. In a medium without free charge, electromagnetic waves are governed by the Maxwell equation

$$\boldsymbol{\nabla}.\vec{\boldsymbol{D}} = \mathbf{0} \qquad \textbf{Equation 2-15}$$

$$\boldsymbol{\nabla}.\vec{\boldsymbol{B}} = \mathbf{0} \qquad \textbf{Equation 2-16}$$

$$\boldsymbol{\nabla}\times\vec{\boldsymbol{E}} = -\frac{\boldsymbol{\partial}\vec{\boldsymbol{B}}}{\boldsymbol{\partial t}} \qquad \textbf{Equation 2-17}$$

$$\boldsymbol{\nabla}\times\vec{\boldsymbol{H}} = -\frac{\boldsymbol{\partial}\vec{\boldsymbol{D}}}{\boldsymbol{\partial t}} \qquad \textbf{Equation 2-18}$$

When light propagating in an isotropic uniform medium $\vec{D} = \varepsilon_0\overleftrightarrow{\varepsilon}.\vec{E}$ and$\vec{B} = \mu_0\overleftrightarrow{\mu}.\vec{H}$, Maxwell's equations becomes

$$\boldsymbol{\nabla}.\vec{\boldsymbol{D}} = \boldsymbol{\nabla}.\left(\boldsymbol{\varepsilon_0\varepsilon}\vec{\boldsymbol{E}}\right) = \boldsymbol{\varepsilon_0\varepsilon\nabla}.\vec{\boldsymbol{E}} = \mathbf{0} \qquad \textbf{Equation 2-19}$$

$$\boldsymbol{\nabla}.\vec{\boldsymbol{B}} = \boldsymbol{\nabla}.\left(\boldsymbol{\mu_0\mu}\vec{\boldsymbol{E}}\right) = \boldsymbol{\mu_0\mu\nabla}.\vec{\boldsymbol{H}} = \mathbf{0} \qquad \textbf{Equation 2-20}$$

$$\boldsymbol{\nabla}\times\vec{\boldsymbol{E}} = -\frac{\boldsymbol{\partial}\vec{\boldsymbol{B}}}{\boldsymbol{\partial t}} = -\boldsymbol{\mu_0\mu}\,\frac{\boldsymbol{\partial}\vec{\boldsymbol{H}}}{\boldsymbol{\partial t}} \qquad \textbf{Equation 2-21}$$

$$\boldsymbol{\nabla}\times\vec{\boldsymbol{H}} = \frac{\boldsymbol{\partial}\vec{\boldsymbol{D}}}{\boldsymbol{\partial t}} = \boldsymbol{\varepsilon_0\varepsilon}\,\frac{\boldsymbol{\partial}\vec{\boldsymbol{E}}}{\boldsymbol{\partial t}} \qquad \textbf{Equation 2-22}$$

From equation 2-21 and equation 2-22, I have a wave equation in the form of equation 2-22

$$\nabla \times \left(\nabla \times \vec{E}\right) = \nabla\left(\nabla . \vec{\mathbf{E}}\right) - \nabla^2 \vec{\mathbf{E}} = -\nabla^2 \vec{\mathbf{E}} = -\mu_0 \mu \nabla \times \frac{\partial \vec{H}}{\partial t} = -\mu_0 \mu \frac{\partial\left(\nabla \times \vec{H}\right)}{\partial t}$$
$$= -\varepsilon_0 \varepsilon \mu_0 \mu \frac{\partial^2 \vec{E}}{\partial^2 t}$$

$$\nabla^2 \vec{E} = \varepsilon_0 \varepsilon \mu_0 \mu \frac{\partial^2 \vec{E}}{\partial^2 t} \qquad \textbf{Equation 2-23}$$

By solving this differential equation, I get the solution for a monochromatic wave as

$$\vec{E}(\vec{r}, t) = \overrightarrow{E_0} e^{i(\omega t - \vec{k}.\vec{r})} \qquad \textbf{Equation 2-24}$$

Where ω is the angular frequency and k=2π/λ is the wave vector. The real part of the electric field vector in the equation above is the actual electric field of the light. If I combine our solution with the equation, I get this relationship.

$$\frac{\omega^2}{k^2} = \frac{1}{\varepsilon_0 \mu_0 \varepsilon \mu} \qquad \textbf{Equation 2-25}$$

$$v = \frac{\omega}{k} = \sqrt{\frac{1}{\varepsilon_0 \mu_0 \varepsilon \mu}} \qquad \textbf{Equation 2-26}$$

Where v is the velocity of the wave. In vacuum, ε =1 and $\mu = 1$ $v = c = 3 \times 10^8$ m/s, the speed of light, and in a non-magnetic medium, $v = \frac{c}{\sqrt{\varepsilon}} = c/n$, where $n = \sqrt{\varepsilon}$ is the refractive index. Here ε is the dielectric constant that is usually frequency dependent. The wave vector is

$$k = \frac{\omega}{v} = \frac{\omega}{c/n} = 2\pi n/\lambda_0 \qquad \textbf{Equation 2-27}$$

Where λ_0 is the wavelength in vacuum. From equation 2-12, I have

$$\nabla . \vec{D} = -i\vec{k} . \overrightarrow{D_0} e^{i(\omega t - \vec{k}.\vec{r})} = 0 \qquad \textbf{Equation 2-28}$$

Because the electric displacement vector is perpendicular to the propagation direction, even in an anisotropic media light is a transverse wave. The electric field vector is perpendicular to the wavevector in isotropic media, but not in anisotropic media. When light propagates in a homogeneous isotropic medium, all the fields have the same form as equation 2-24.

2.4 Polarization

When light of a single wavelength (monochromatic) moves through an isotropic medium, I can consider the electric field to be.

$$\vec{E} = \vec{A}e^{i(\omega t - \vec{k}.\vec{r})} \qquad \textbf{Equation 2-29}$$

Where A is a constant and all other quantities can be calculated from this equation. Since the equation 2-29 is a vector and has direction this is our polarization state. When the electromagnetic wave moves a z-axis I can break up the field to two components (along the x and the y axes) [71,72]:

$$E_x = A_x \cos(\omega t - kz + \delta_x) \qquad \textbf{Equation 2-30}$$

$$E_y = A_y \cos(\omega t - kz + \delta_y) \qquad \textbf{Equation 2-31}$$

Where A_x and A_y are positive numbers representing the amplitudes; δ_x and δ_y are the phases which, are defined in the range $-\pi < \delta_i < \pi$ (i=1, 2).

$$\delta = \delta_y - \delta_x \qquad \textbf{Equation 2-32}$$

Linear Polarization States

When the electromagnetic wave moves in the direction z, the electric component of the field oscillates in the x-y plane. When this vibration is in a constant direction, I say that it is linearly polarized and that $\delta=0$ or $\delta=\pi$.

2.5 Circular Polarization States

Circular polarization occurs if the amplitude in x-y plane is the same but out of phase by $\delta= \pi/2$, when you compute the total vector I rotates in plane.

$$E_x = A\cos(\omega t - kz) \qquad \textbf{Equation 2-33}$$

$$E_y = A\cos\left(\omega t - kz + \frac{\pi}{2}\right) = -A\sin(\omega t - kz) \qquad \textbf{Equation 2-34}$$

At a fixed position, say z=0, E_x=A cos (ωt) and E_y=- A sin (ωt). The endpoint of the electric field vector will trace out a circle clockwise on the x-y plane (light coming toward the observer). At a given time, say t = 0, E_x= A cos (kz) and E_y= A sin (kz). The endpoint of the electric vector along a line in the propagation direction traces out a right-handed helix in space. The polarization is referred to as right-handed circular polarization. If δ= -π/2, at a given time, the endpoint of the electric vector will trace out a left-handed helix in space. This is referred to as a left-handed circular polarization.

2.6 Propagation of Light in Uniform Anisotropic Optical Media

Liquid crystal is isotropic in the liquid phase and anisotropic in liquid crystal phases. In order to understand how light propagates in a liquid crystal I need to understand how it generally propagates in an anisotropic media. The speed of light depends on the direction of electric field compared to medium. Since the dielectric constant depends on the optical axis, I must model it as a tensor. Now I consider the propagation of light in uniform non-magnetic anisotropic media [71,73]. The optical properties of an anisotropic medium are described by the dielectric tensor ε :

$$\vec{\vec{\varepsilon}} = \begin{pmatrix} \boldsymbol{\varepsilon_{11}} & \boldsymbol{\varepsilon_{12}} & \boldsymbol{\varepsilon_{13}} \\ \boldsymbol{\varepsilon_{21}} & \boldsymbol{\varepsilon_{22}} & \boldsymbol{\varepsilon_{23}} \\ \boldsymbol{\varepsilon_{31}} & \boldsymbol{\varepsilon_{32}} & \boldsymbol{\varepsilon_{33}} \end{pmatrix} \qquad \textbf{Equation 2-35}$$

If the medium does not absorb the light then, the dielectric tensor is real and symmetric ($\varepsilon_{ij} = \varepsilon_{ji}$). I choose the reference frame that makes 2.35 into equation 2.36:

$$\vec{\vec{\varepsilon}} = \begin{pmatrix} \boldsymbol{\varepsilon_x} & \mathbf{0} & \mathbf{0} \\ \mathbf{0} & \boldsymbol{\varepsilon_x} & \mathbf{0} \\ \mathbf{0} & \mathbf{0} & \boldsymbol{\varepsilon_z} \end{pmatrix} \qquad \textbf{Equation 2-36}$$

Birefringence in conventional LC has the special case which are tensor is: In case of uniaxial materials, such as conventional nematic liquid crystals, $\varepsilon_1 = \varepsilon_2 = \varepsilon_\perp$, and $\varepsilon_3 = \varepsilon_{||}$

$$\hat{\boldsymbol{\varepsilon}} = \begin{pmatrix} \boldsymbol{n_\perp^2} & \mathbf{0} & \mathbf{0} \\ \mathbf{0} & \boldsymbol{n_\perp^2} & \mathbf{0} \\ \mathbf{0} & \mathbf{0} & \boldsymbol{n_{||}^2} \end{pmatrix} \qquad \textbf{Equation 2-37}$$

If the anisotropy of a material persists in a range longer than the wavelength of the light, the material will be optically anisotropic. In this case, the propagation through the

material depends on the direction of propagation and of the variation of the electric vector. The speed of light is determined by the refractive index n, which for uniaxial materials will be different along $\boldsymbol{n}$ and perpendicular to the director $\boldsymbol{n}$ the numerical difference Δn between these refractive indices is called "birefringence". The birefringence depends on the wavelength of the light (dispersion), which in the visible and near infrared region typically can be approximated by the Cauchy formula: $\Delta n = A + B/\lambda^2$, A and B are Cauchy coefficients. Calamitic (rod-like) thermotropic liquid crystals in the visible range typically have positive Δn, being in the range of 0 and 0.45. Very low birefringence is characterized for materials made from bucyclohexanes, whereas the most birefringent nematic is made of biphenyl-diacetylenics. Generally, the anisotropy is high if two or more benzene rings are connected by conjugated bonds. The sign of Δn is related to the direction of the molecular dipole with respect to molecular long axis.

The birefringence of lyotropic liquid crystals is almost an order of magnitude smaller due to their water content and because of their flexible hydrocarbon chains, which make up a relatively large part of the amphiphilic molecules, contributing to birefringence only weakly.

2.7 Birefringence

The optical anisotropy in nematic LC is caused by its physical anisotropy, how the shape of the object differs along one axis compared to another. Looking at the 5CB molecule (figure 1.3), it has a rod-like shape as the molecular structure consists of two aromatic rings. 5CB has two aromatic rings along the z axis, if light passes parallel to the z axis then it will go through both rings but if passes perpendicular to z axis then it only goes through one ring. This means that when light passes through the molecule the light has a different interaction with one axis compared by the other, as the long axis has two aromatic rings with carbon tails while the other just has a singular aromatic ring. When I define the different refractive indices of a material I do so in relation to its optic axis, the axis along which there is no birefringence. When light passes through a material there will be light whose polarization refracts perpendicular and parallel to the optic axis. Light that is polarized perpendicular to the optic axis is called the "ordinary" refractive index (n_o), while light in the direction of the axis is "extraordinary (n_e). The difference between the n_o and n_e is the birefringence:

$$\Delta \boldsymbol{n} = \boldsymbol{n_e} - \boldsymbol{n_o} \qquad \textbf{Equation 2-38}$$

Chapter 3

Methods

3.1 Polarized Optical Microscopy

Because liquid crystals exhibit birefringence, polarized optical microscopy is a useful technique for imaging their defect textures and identifying the point of phase transitions. (figure 3.1)

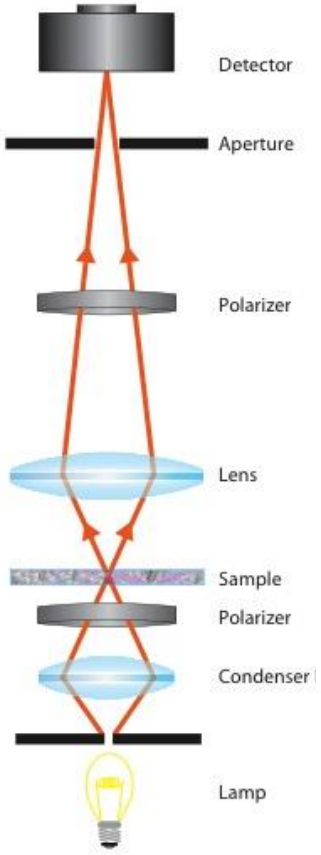

Figure 3-1. Schematic of a polarized optical microscope [74]

To visualize a liquid crystal texture under POM, the samples are prepared as a thin film between glass coverslips that can optionally be surface treated. When a sample is in a liquid crystal phase, the local direction of the molecules can modulate the polarization of incident light. By observing the intensity pattern that emerges from the sample through crossed polarizers, one can usually identify a material's phases despite not having the resolution to identify individual molecules. To use this technique for phase identification, it is essential to be familiar with the different textures each phase can exhibit (Figure 3-2).

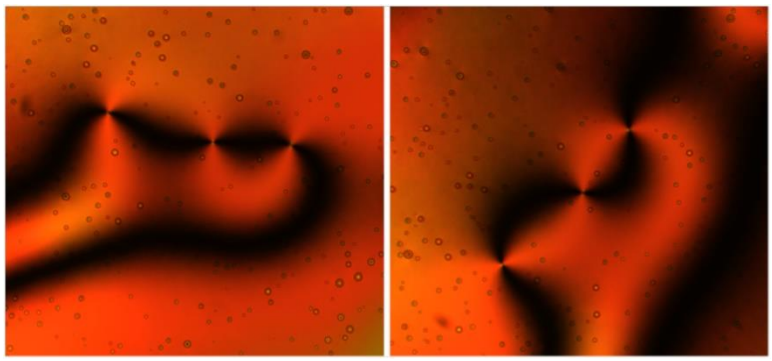

Figure 3-2. Two different polarized optical microscopic images of the same brush defect in the nematic phase taken at two different arbitrary angles 45° apart. [74]

Figure 3-2 shows two images of the same liquid crystal defects, but the images were recorded with sample orientations 45 degrees apart. Notice that the intensity distribution on the images is not exactly the same. While the overall pattern is the same, some areas that are light on the left-hand side are dark on the right-hand side. Areas of the sample in which the director is not aligned with either polarizer in the first image (and let some light through the crossed polarizers), become aligned in the second image and appear dark.

In Figure 3-3, I can see a more detailed view of the liquid crystal slab and the polarizers. Figure 3.3 shows the orientation of the polarizers relative to the sample. We can start by considering the incoming light as an unpolarized monochromatic plane wave. When the light encounters the polarizer orientated in the y direction, it eliminates any vector components that are in the x direction. This polarized light is incident on the liquid crystal slab, where the local orientation of the crystal acts a waveplate, forming two waves polarized in orthogonal directions, with amplitudes A$\sin\theta$ and A$\cos\theta$. As indicated in figure 3.3, θ is the angle between the liquid crystal director and the polarizer (P1) direction. I can treat these orthogonal components independently as they propagate through the light crystal slab. The filed component parallel to the director travel with an amplitude of

$$\boldsymbol{A\cos\theta\cos\left(\omega t-\frac{2\pi}{\lambda}n_e d\right)} \qquad \textbf{Equation 3-1}$$

and the component polarized perpendicular to the director will have an amplitude of

$$\boldsymbol{A\sin\theta\cos\left(\omega t-\frac{2\pi}{\lambda}n_o d\right)} \qquad \textbf{Equation 3-2}$$

after passing through the analyzer (P2). Aligned in the x direction, the two transmitted wave components will have amplitudes

$$\mathrm{A}\boldsymbol{\cos\theta\sin\theta\cos\left(\omega t-\frac{2\pi}{\lambda}n_e d\right)} \qquad \textbf{Equation 3-2}$$

$$\mathrm{A}\boldsymbol{\cos\theta\sin\theta\cos\left(\omega t-\frac{2\pi}{\lambda}n_o d\right)} \qquad \textbf{Equation 3-3}$$

by squaring the sum of these amplitudes, you can find the total intensity passing through the crossed polarizers,

$$I = I_o \sin 2\theta^2 \sin(\frac{\pi d}{\lambda}\Delta n)^2 \qquad \textbf{Equation 3-4}$$

where Δn is the birefringence (n_e-n_o). From this result, I can clearly see that as the liquid crystal sample is rotated between the polarizers, angle θ will vary and therefore the transmitted intensity varies as a $\sin 2\theta^2$ function from zero, when the director is aligned with either polarizer, to a maximum value after a rotation of 45°.

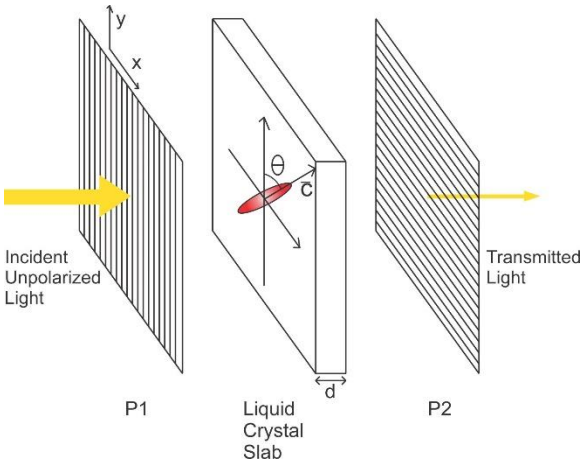

Figure 3-3**. The geometry of a liquid crystal slab rotated between crossed polarizers. [74]**

Changing the angle of the director by rotating the sample I see bright and dark areas, which is dependent on the orientation of director related to the cross polarizers (figure 3.4 a). When I place a slab of liquid crystal between two cross polarizers, if the direction of director is in same direction as either polarizer then I will not see anything. If however it makes an angle with both polarizers then I can see transmitted light. Polarized optical microscopy can be used as an imaging technique to visualize the direction of the director. The maximum intensity on the image will be observed if the director is at 45º to the polarizers, wheras the darkest areas (extinction) are observed where the director is parallel to one of the polarizers. Figure 3.4 (b and d) shows two different common molecular alignments in a liquid crystal cell; Planar and Homeotropic. For the planar alignment (molecules orient parallel to the image plane), if I rotate the sample between the polarizers, bright areas becomes dark when the director becomes parallel with one the polarizers (figure 3.4 c). For homeotropic alignment (molecules orient perpendicular to the image plane) the material is not birefringence and the light behaves as if there are only the two cross polarizers (i.e. no sample), completely blocking the transmission of light (figure 3.4 e).

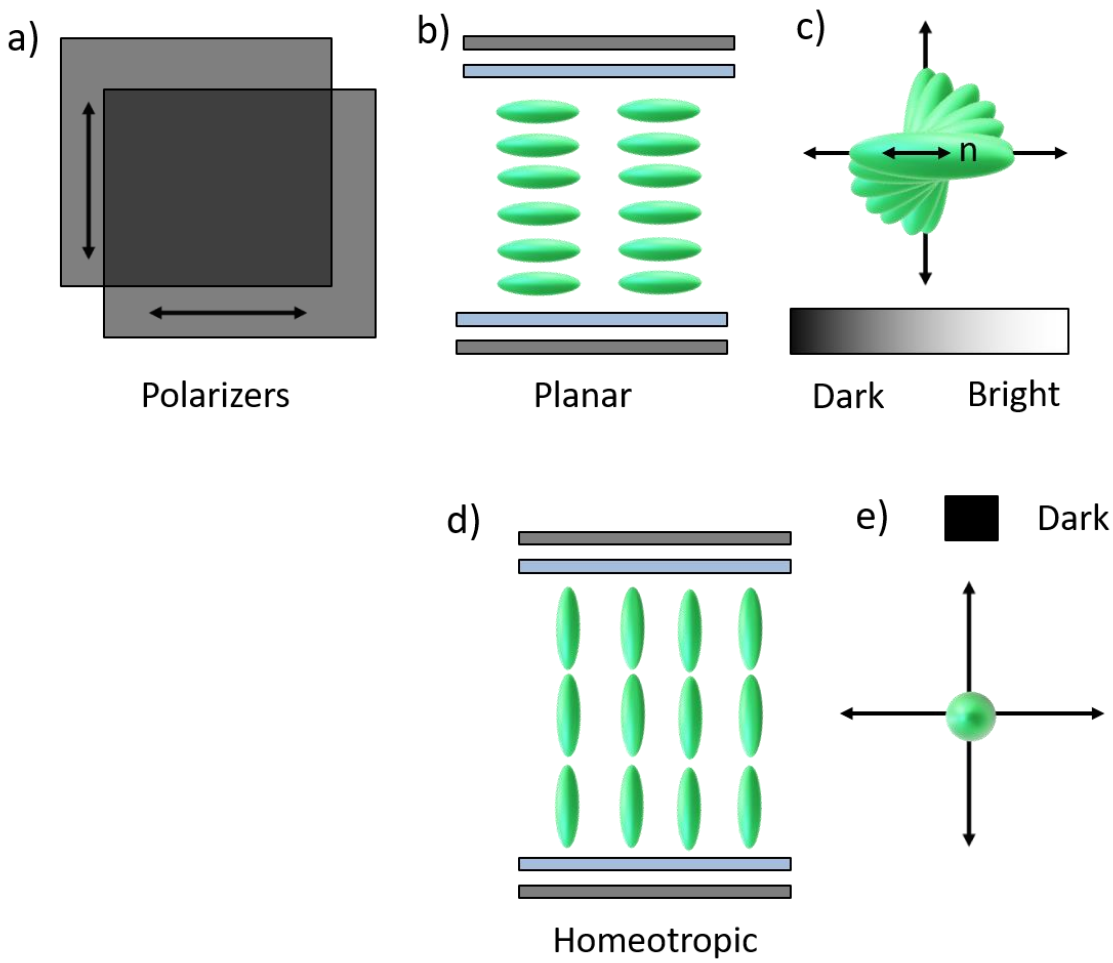

Figure 3-4. Schematic presentation of nematic liquid crystal alignment in cell with (b) planar and (d) Homeotropic anchoring

3.2 Fluorescence Microscopy

I use fluorescence microscopy to visualize the nanoparticle composites investigated in this thesis at the micron level. Fluorescence microscopy uses light that has been absorbed and re-emitted by a material to create an image. I can use fluorescence microscopy in different areas of science such as: engineering, physics, medical science, biology, and material science. Figure 3.5 illustrates the basic principles of fluorescence microscopy. Incident white light passes through an excitation filter to select for a narrow excitation band. After passing through the filter, the light will reflect off a dichroic mirror and focus into a beam that strikes the sample surface. The fluorescent specimen is excited by the incident wavelength, then light is re-emitted at a longer wavelength. The emitted light then

passes through an emission filter before reaching the detector to block reflected (non-absorbed) light from the excitation band.

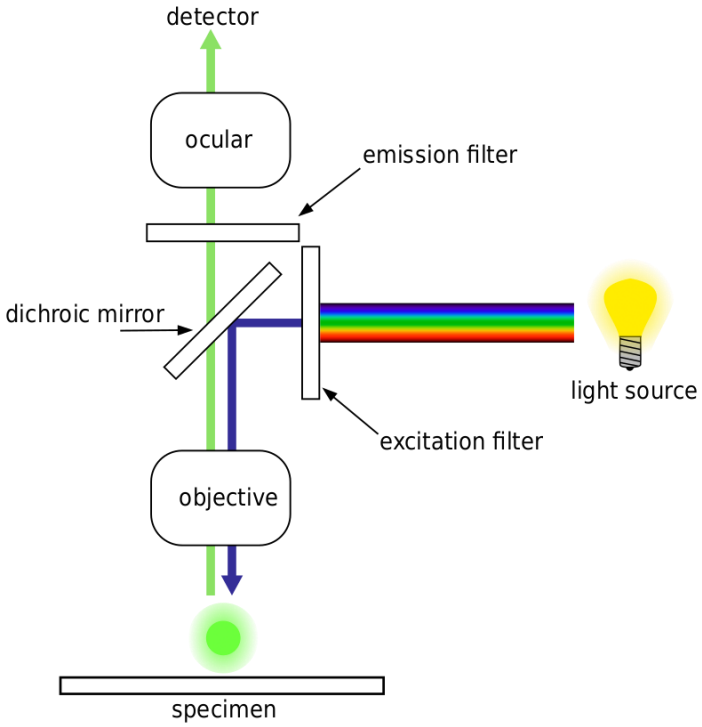

Figure 3-5. Schematic for a fluorescence microscope [63]

3.2.1 Confocal Microscopy

To image a very well-defined focal plane, we can use confocal microscopy. A confocal microscope is a fluorescence microscope that uses pinholes to selectively image a narrow foca plane. One of the main limitations of standard microscopy is existence of background image noise due to the detection of fluorescence from out-of-focus sample planes. I can eliminate this noise and get more detailed, higher quality images, and better contrast by using confocal microscopy compared to the standard microscope. Also, I can use confocal microscopy to obtain 3D images of materials [75]. Figure 3-6 is a schematic of a confocal microscope.

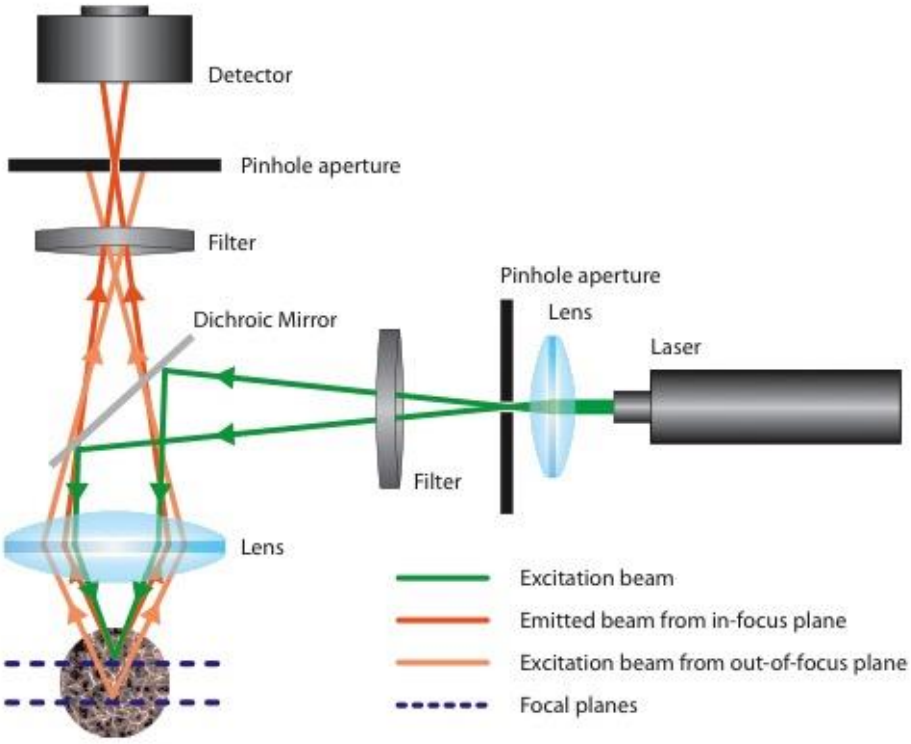

Figure 3-6. The schematic of confocal microscopy [74]

The basic configuration of the confocal microscope is as follows. An excitation beam is emitted from a laser source. A dichroic mirror reflects the beam before it passes through a pinhole aperture. The excitation beam is focused by the objective lens at the desired focal plane in the sample. The emitted fluorescence is collected by the objective lens and passes through a second pinhole aperture to be imaged by a detector. In the standard fluorescence microscope, a large depth of field is illuminated, and all of the light from that focal depth is included in the image, including heights above and below the focal plane of interest. The second pinhole in the confocal configuration will only allow emitted light from the desired focal plane to pass (See Figure 3-6). [78M]. The confocal images in this thesis were taken by the Zeiss LSM700 at UC Merced.

3.3 Introduction to proton NMR

Nuclear Magnetic Resonance (NMR) spectroscopy is a general technique used for component characterization and determining molecular structure. I can tune the NMR spectrometer to a specific nucleus such as: ^{1}H, ^{13}C, ^{19}F, and ^{31}P. In this study, I have tuned to the proton (^{1}H) for the purpose of these of experiments. I picked ^{1}H NMR because it is simple and effective. Almost all organic molecules contain hydrogen and carbon. Since our ligand is an organic molecule, it contains hydrogen and carbon.

Schematic 3-7 shows the operation of a basic NMR spectrometer; a sample containing protons (hydrogen nuclei) is placed in a strong magnetic field, where the nucleus of our sample is hit with a pulse that contains a different range of frequencies. If the frequency of that pulse which is emitted is just right, it will excite the nuclei from the spin-up state to the spin-down state. The spins tend to return to their lower state, producing a small amount of radiation after the strong radiofrequency signal is switched off. The change in the frequency of nuclei is called the chemical shift of our atom. Different atoms have different chemical shifts, if we know the chemical shift of each atom, we can place our unknown components into the NMR and determine all the changes in frequency value and that will tell us the type of atom inside our unknown compounds. Basically, just the right frequency is required for our nuclei to jump and transition between the quantum states, this is known as resonance.

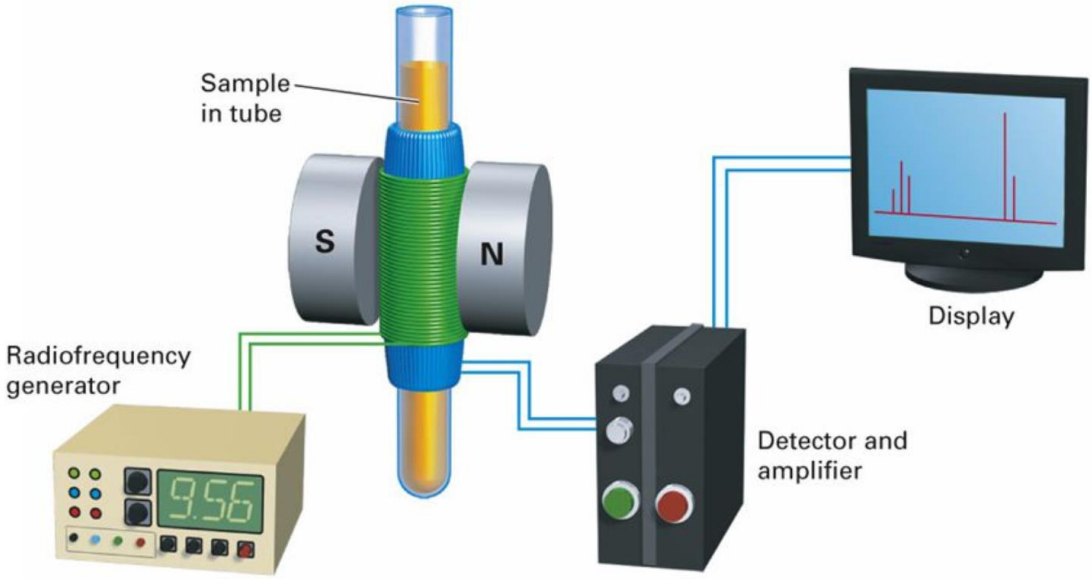

Figure 3-7. Schematic operation of a basic NMR spectrometer [63]

3.3.1 Nuclear Equivalence

Why should the nuclei in different compounds behave differently in an NMR experiment?

When I apply a magnetic field to the sample, the protons experience a smaller net magnetic field due to the shielding electrons. Circulating electrons around the proton produce an induced magnetic field in the opposite direction, which lowers the effective magnetic field experienced by the proton. The difference between the applied magnetic field and the field that nuclei experience (B effective) is called nuclear shielding (B induced). By increasing the density around the proton then you would increase the shielding of that proton and decrease the amount of effective magnetic field.

As an example, there is no electron for ionized hydrogen, so the de-shielded proton is going to experience the full effect of applied magnetic field. Another example is methane. I have 4 hydrogens and the shielded proton has a circulating electron density that creates a magnetic field - so the proton feels a smaller effective field.

In this study, NMR spectra were obtained on Agilent spectrometers at UC Merced. ^{1}H NMR spectra were obtained at 400 MHz and referenced to the residual CHCl3 singlet at 7.26 ppm unless otherwise noted.

3.4 Scanning Electron Microscope:

To characterize the surface morphology of our system I used Scanning Electron Microscopy (SEM). After forming micro shells and extracting them from the liquid crystal medium I inserted them onto the indium tin oxide (ITO)/ silicon wafer and used the FE-SEM (Field Emission- SEM), Zeiss Gemini SEM 500, to image. The FE-SEM operated at voltage 3kV for validating morphology and also used the in-lens detector. To enhance the quality of the images I used Zeiss Gemini SEM software to change the contrast and brightness.

An SEM uses an electron beam to image the sample. To focus the beam, I use a series of electromagnetic lenses. I cannot use glass lenses like an optical microscope because electron beams will not pass through the glass, however since the electrons are charged and, in this instance, moving, they can be influenced by an applied magnetic field. Electrons pass through an anode, which is positively charged, after they come out of the gun, then a magnetic lens helps to condense the beam. The sample is located on a stage that is positively charged which helps keep the electron beam on target. When the electron hits the surface of the sample, we have three different types of electron: reflected, absorbed, and secondary. When the electrons from the gun hit the surface of sample, they can be absorbed or reflected. An atom on the sample surface can be excited by the electron beam. The excited surface atom will release another electron which we called secondary electron release. The secondary electrons are coming from the surface of the sample and hence can be used to map the surface features. Back scattered electrons are simply electrons that have hit the sample and bounced off. Some regions of the sample will absorb electrons and this effect can be used to map the surface features.

I used two detectors, which pick up electrons: The back-scattered electron detector and a secondary electron detector. The detector uses the information from the electron to form an image. By using two different detectors I can observe both varieties of electron (absorbed and reflected) and construct an image of the samples surface structure.

3.4 Transmission Electron Microscopy

Transmission Electron Microscopy is another electron-based technique that I used to measure the distance between nanoparticles. I used this to get images at the nano level with the high resolution. TEM images were obtained with a JEOL-2010 TEM equipped

with a LaB6 filament and operated at 200kV in the Imaging and Microscopy Facility at UC Merced. TEM samples were prepared by depositing 0.2μL of solution on a TEM copper grid with carbon film (400 mesh, Ted Pella Inc), wicking the excess solvent and placing the TEM grid in a vacuum oven at 40 °C, -25 mmHg, for 3h to remove residual solvent.

3.5 Small Angle X-ray Scattering

X-rays have wavelengths in the range of 0.01 to 10nm, which is comparable to the size of nanoparticles. I used this electromagnetic radiation to study the structural arrangement of nanoparticles. Figure 3.8 shows the schematic of Bragg scattering, in which constructive interference between photons scattered form ordered layers produces a characteristic diffraction pattern. When x-rays are incident on a material, they may be elastically scattered due to their interaction with the electrons in the material. For elastic scattering the x-ray wavelength does not change and only momentum is transferred. For nanoscale materials packed closely (e.g. nanoparticles in our microshells), I use small angle x-ray scattering to obtain structural information on the material. This technique helps us to understand the arrangement of nanoparticles in our sample by studying the scattering pattern. X-rays scattered from nanoparticles in aggregates and microshells create a diffraction pattern and despite the lack of long-range order. The first Bragg peak can usually be observed, characteristic of the average particle separation. Diffraction patterns often can be interpreted by the Bragg equation:

$$n\lambda = 2d \sin\theta \qquad \textbf{Equation 3-5}$$

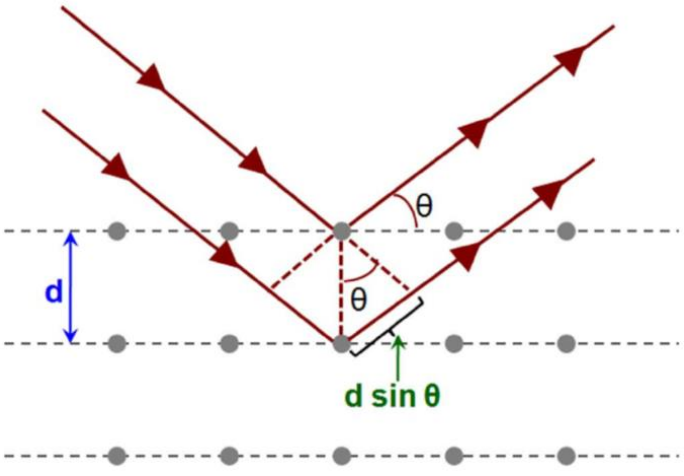

Figure 3-8. Scattering geometry of Bragg diffraction

Small angle x-ray scattering (SAXS) measurements (See figure 3.9) were performed at the Advanced Light Source (ALS), beamline 7-3-3, Lawrence Berkeley National Laboratory. Measurements were carried out in a transmission configuration at 10KeV for 1second per exposure at 3 spatially different points using drop-cast films on thin Mylar films and in a 1mm quartz capillary for solutions. Beam size was 1mm x 3mm at the sample. SAXS gives us a plot of intensity vs. $q=2\pi/d$ (the distance of diffraction ring from the center), by analyzing the graph I can get the value of d spacing (average distance between nanoparticles in the assembly).

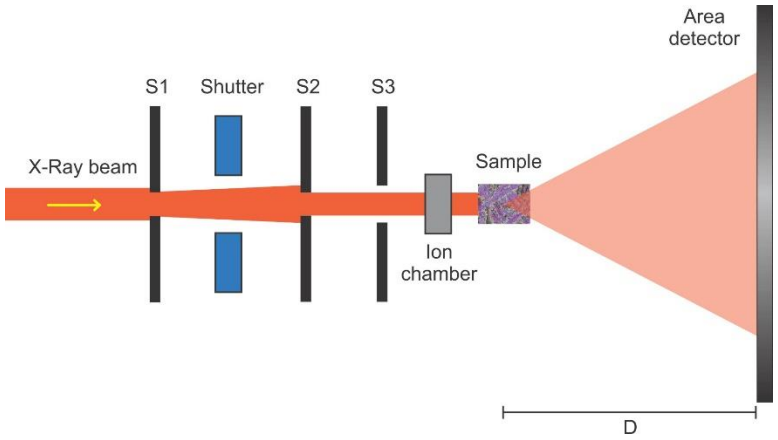

Figure 3-9. Schematic of a typical transmission x-ray scattering beam-line [74]. S1-3 are slits to define the beam and D is the sample to detector distance.

3.6 Differential Scanning Calorimetry (DSC)

DSC is a thermal characterization technique that allows us to study the phase transitions of liquid crystals. When I apply heat to a material, its temperature changes linearly as a function of applied thermal energy. The following equation shows the amount of heat flow (ΔQ) into a material as the temperature changes (ΔT):

$$\Delta \boldsymbol{Q} = \boldsymbol{mc}\Delta \boldsymbol{T} \qquad \textbf{Equation 3-6}$$

Where *c* is the specific heat of the material, and *m* is the mass.

The DSC apparatus has two chambers (See Figure 3.11), one of them contains the sample and the other one is empty as a reference. The instrument is calibrated such that temperature difference between the sample and the reference is zero as they are heated at a fixed rate (°C/min)..

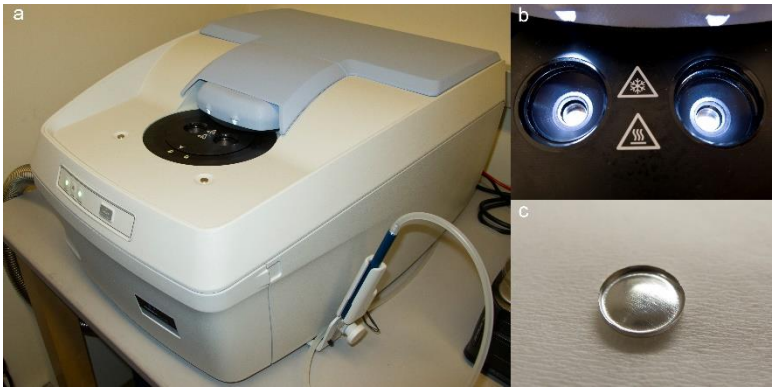

Figure 3-10. A high-sensitivity differential scanning calorimeter typically used for liquid crystal materials is shown in (a) and a close-up picture of the two furnaces in (b). Picture (c) shows an aluminum sample pan used to encapsulate the sample. These sample pans hold a few milligrams of material. [74]

The instrument gives us a baseline heat flow curve as a function of the temperature as I heat or cool the material. If the material (solid, liquid) undergoes a phase transition during heating, I observe a sudden change on the graph. The area under the curve represents the total energy transfer to into or out of the material during the phase transition. At a phase transition, the sample's response to changes in heat energy is altered as this energy is reordering the intramolecular bonds. For example, if you were to heat water, the temperature will increase until the water boils, the heat energy going into breaking the bonds between the molecules. Since the sample's temperature change is kept at a constant rate (C/min) this leads to a rapid change in the amount of energy required to affect change in the temperature. Figure 3.12 shows one example of DSC measurement of LC (8CB).

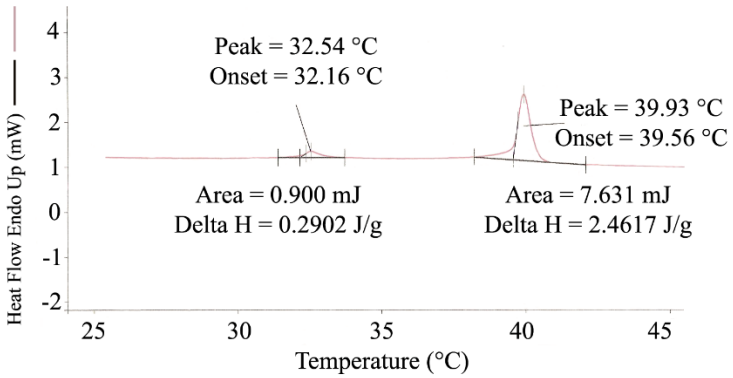

Figure 3-11. an example of differential scanning calorimetric data for a thermotropic liquid crystal (8CB), the first peak is the smectic A to nematic phase transition and second peak is the nematic to isotropic liquid phase transition. Delta H is the enthalpy of the transitions. [74]

Chapter 4

Designing ligands for robust micro-capsule formation

4.1 Introduction

Closely packed assemblies of NPs can exhibit differing electronic, magnetic, and photonic properties [76,77] when compared to those of isolated single particles. However, controlling particle spacing well requires a strategy. Van der Waals attractions between bare nanoparticles can make it very difficult to control dispersion and so ligands are commonly used to both enhance dispersion in different solvents and to tune assembly with a defined inter-particle spacing.

In this chapter, I introduce the properties, and performance of a new class of promesogenic calamitic side-tethering organic ligands used to direct quantum dot nanoparticle self-assembly via nematic templating. Attaching the new ligands to quantum dots and dispersing them in a liquid crystal host affords hollow micron-sized capsules via nematic templating. The capsules resist thermal decomposition up to 350 °C — significantly higher than any previously reported microcapsules assembled from side-tethering calamitic ligand-functionalized nanoparticles. These novel ligands can be used in encapsulation applications where stability under high temperature is required. Evaluation of the capsules by small-angle X-ray scattering shows that interparticle spacing varies from 10–13 nm depending on the ligand used and is correlated to amino alkyl chain length.

Liquid crystal materials are ordered fluids characterized by their anisotropic properties and in this dissertation, I focus on a strategy for particle assembly using the nematic liquid crystal phase. Molecules in the nematic phase have short-range orientational order, defined by a local director, **n**, and no positional order. Many nematic liquid crystal materials have the ability to respond to an applied electric field and switchable electronic displays represent their primary application. However, liquid crystal science intersects the boundaries between several fundamental scientific disciplines and has already made some very important contributions to nanoscience and nanotechnology, in particular in the field of nanocomposites. Surface functionalized nanoparticles can be dispersed in liquid crystal media, creating a hybrid material that uses self-assembly to control dispersion [78,79]. Stable dispersion over long timescales is an important goal for soft tunable photonic devices such as the liquid crystal laser. Recently, significant efforts have been devoted to developing hybrid liquid crystal nanocomposites [80]; materials that incorporate nanoparticles into a liquid crystal phase in a controlled fashion. By combining the switchable, fluid capabilities of liquid crystal materials with the added functionality of nanoparticles there is huge potential to create exciting multifunctional new systems. Recent studies have looked at creating stable dispersions of magnetic, metallic, and semiconductor particles in the smectic [81,82], nematic [83,84], columnar [85,86] thermotropic phases [87]. The most promising of these studies include modification of surface ligands on the nanoparticle to achieve increased particle stability against precipitation [17]. In other work the goal has been not to produce a uniform dispersion of isolated particles in liquid crystal, but to design a system in which the particles assemble in defined clusters or three-dimensional structures.

A wide variety of small organic molecules have been employed as surface-modifying ligands for metallic or semi-conducting nanoparticles. [88,89,90,91,92]. Metal nanoparticles functionalized with mesogenic (liquid crystalline) or promesogenic organic ligands bearing a motif consisting of multiple closely linked aromatic rings—likened to a molecular 'rod' (calamitic) and an orthogonal nucleophilic tethering arm self-assemble [93] into different two- and three-dimensional mesoscale morphologies like rods, spheres, and capsules . [94,17 ,18 ,20 ,19 ,95].The derived morphologies are envisioned for use in biochemical sensors,[96,97] optoelectronic and photovoltaic devices,[98,99,100,101] and LED's [102]. Rather few side-attaching ligands have been systematically evaluated as mediators of nanoparticle self-assembly. In one example, using three different ligands, Pociecha and coworkers showed that varying the length of the alkyl chain connected to the thiol can direct the self-assembly of the resultant ligand-modified gold nanoparticles into various morphologies upon evaporation of toluene [103]. After attaching ligand to core–shell quantum dots, micron-sized discrete capsules form following nucleation and growth of the nematic phase at the isotropic–nematic transition temperature of a liquid crystal host, such as 4-cyano-4'-pentylbiphenyl (5CB) [17,95]—a process we refer to as nematic templating. The process takes advantage of the differential solubility of the ligand-modified particles in the nematic and isotropic phases of a liquid crystal (such as the commonly used 5CB). Initially, ligand- modified NPs are uniformly dispersed in the isotropic phase. The composite system is then cooled rapidly into the nematic phase, where the system phase nucleation followed by growth within the shrinking isotropic domains results in particle segregation to the domain interfaces, and ultimately a variety of hollow structures, [104] including the capsules reported here.

A fundamental challenge for nanoscience is to find a way to organize different type of nanoparticles into defined distributions such as well dispersed distributions of particles in a fluid phase, closed-packed assemblies, and dynamic clusters of different particles. In a recent study, our lab developed a unique assembly method for mesogen-functionalized quantum dots using nematic liquid crystal as a host phase [16]. Mesogenic ligands can be used to control clustering, dispersion stability [105] and particle assembly at the liquid crystal transition [18]. In this system a liquid-crystal like ligand was attached to the QD surface and these modified particles were dispersed in the isotopic phase of a nematic liquid crystal. The resulting composite system produced remarkable vesicle-like microcapsules (micro-shells) when the liquid crystal was cooled into the nematic phase. The shells are robust and can tolerate temperatures up to 110 ^{o}C, and extraction from the liquid crystal medium.

Hollow micron-scale capsules constructed from closely packed quantum dots [18] and metallic nanoparticles [19] have been previously demonstrated by our group in which the mesogenic ligands (See Figure 4-1) were designed for low temperature encapsulation applications. Metallic nanoparticle capsules were designed to produce an optically triggered release by taking advantage of plasmonic heating. For the new ligand series reported here, we employ a different ligand core structure designed to form capsules by the same mechanism, while supporting high temperature applications. The new capsules are much more robust to extreme temperatures, yet still capable of triggered release by

alternative methods such as mechanical shear. Ligand designs favor a stronger π–π interaction between the nanoparticles, owing to reduced flexibility in the ligand core.

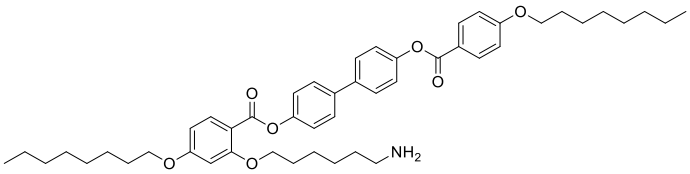

Figure 4-1. Schematic of molecular structure of mesogenic ligand

4.2 Molecular Structure of Ligands

Table 4-1 shows the molecular structure of ligands which are composed of a rigid rod-like segment with flexible arm sections. The flexible part has two sides; the amine group (-NH2) is on the right side of molecules and another arm is on the left side of alkyl chains.

Molecular Structure	Chemical Name
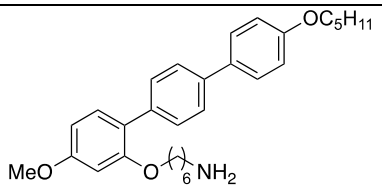	*4-methoxy-4''-(pentyloxy)-[1,1':4',1''-terphenyl]-2-yl) oxy)hexan-1-amine* 4a
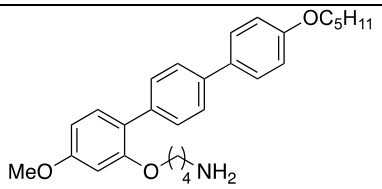	*4-methoxy-4''-(pentyloxy)-[1,1':4',1''-terphenyl]-2-yl) oxy)butan-1-amine* 4b
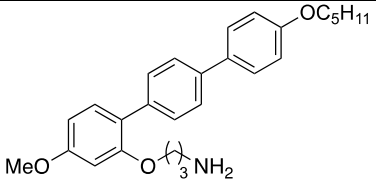	*4-methoxy-4''-(pentyloxy)-[1,1':4',1''-terphenyl]-2-yl) oxy)propan-1-amine* 4c
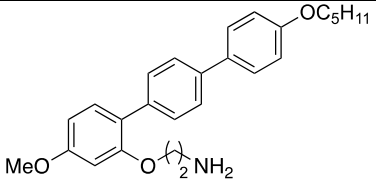	*4-methoxy-4''-(pentyloxy)-[1,1':4',1''-terphenyl]-2-yl) oxy)ethan-1-amine* 4d

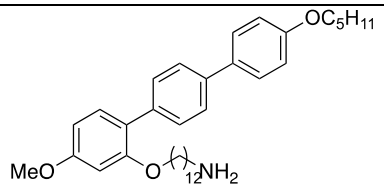	*4-methoxy-4''-(pentyloxy)-[1,1':4',1''-terphenyl]-2-yl) oxy)dodecan-1-amine* 4e
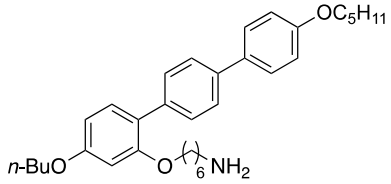	*4-butoxy-4''-(pentyloxy)-[1,1':4',1''-terphenyl]-2-yl) oxy)hexan-1-amine* 4f
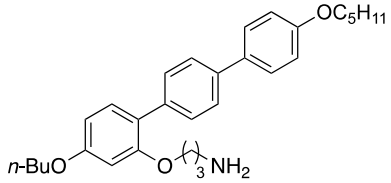	*4-butoxy-4''-(pentyloxy)-[1,1':4',1''-terphenyl]-2-yl) oxy)propan-1-amine* 4g
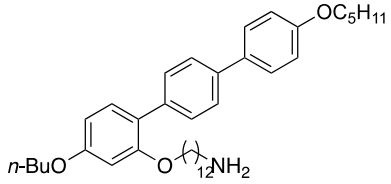	*4-butoxy-4''-(pentyloxy)-[1,1':4',1''-terphenyl]-2-yl) oxy)dodecan-1-amine* 4h
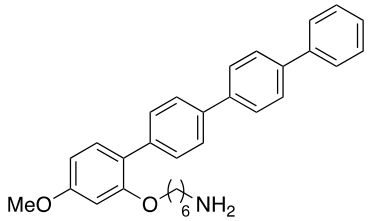	*4-methoxy-[1,1':4',1'':4'',1'''-quaterphenyl]-2-yl) oxy)hexan-1-amine* 4i
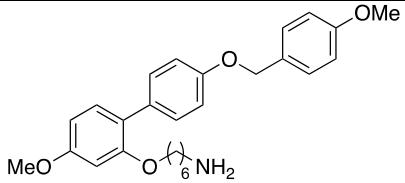	*4-methoxy-4'-((4-methoxybenzyl) oxy)-[1,1'-biphenyl]-2-yl) oxy)hexan-1-amine* 4j
L16 Sulfur 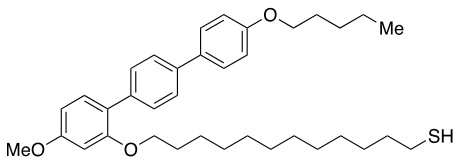	12-((4-methoxy-4"-(pentyloxy)-[1,1':4',1"-terphenyl]-2-yl) oxy)dodecane-1-thiol

Table 4-1 Calamitic ligands used for ligand-modified metal nanoparticle self-assembly.

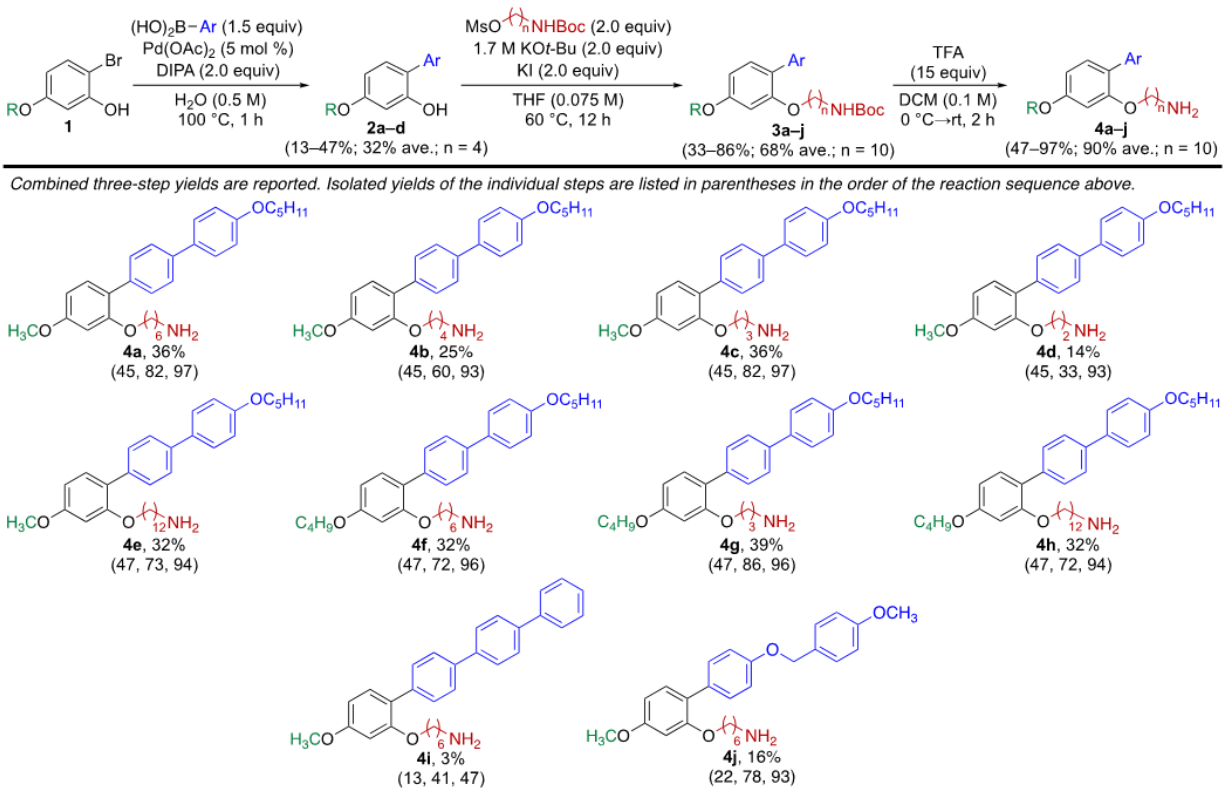

Figure 4-2. Ligand library synthesis, "Reproduced with permission from the American Chemical Society" [106]

4.3 Characterization of Ligands using Polarized Optical Microscopy

A thin film of each ligand was enclosed between a standard glass slide and cover slip, and slowly heated to the isotropic phase. The films were then cooled into the crystal phase and reheated several times on a Linkam microscopy heating stage to identify a reversible phase sequence on the polarized optical microscope. Of the ligands synthesized, 4a–4h exhibit crystal morphologies as visualized by polarized optical microscopy (POM) (Figure 4-3.), though no evidence of a liquid crystal phase is ever detected: all ligands visually transition directly from crystal to isotropic liquid. Using differential scanning calorimetry (DSC), only a single transition was observed for 4a–4h (Figure 4-3., inset in each POM image), and which I ascribe to melting from the solid to the isotropic liquid phase (see figure 4-4) for DSC traces. In contrast, mesogens like C (Figure 4-1) and others exhibit multiple phase transitions by POM and DSC. Interestingly, ligand 4c exhibited a higher melting point than any other ligand, which may be attributed to shorter alkyl chain lengths within the amine tether (red) and aryl ether (green). Similarly, ligand 4g exhibits a higher melting point than 4f and 4h.

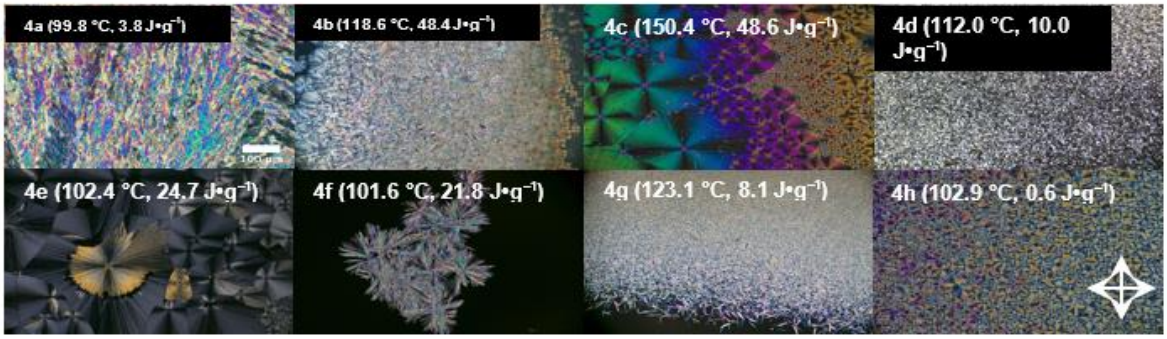

Figure 4-3. Birefringence textures of 4a–h observed using polarized optical microscopy (10X objective). Transition temperature (T_{trans}) and latent heat (ΔH_{trans}) of the only observed differential scanning calorimetry event for each ligand are included in parentheses. Crossed arrows indicate polarizer directions. "Reproduced with permission from the American Chemical Society" [106]

4.4 Differential Scanning Calorimetry of Ligands

Small amounts (6–10 mg) of ligand in the crystal phase were encapsulated in an aluminum pan and cycled through melting and recrystallization at least once before recording a DSC trace. All data was collected on melting with a temperature ramp rate of 10 °C /min. An empty pan was used for the reference material. Enthalpies for each transition are calculated as the area under each peak.

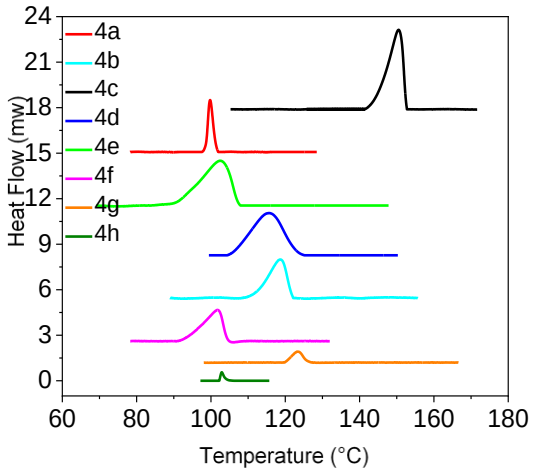

Figure 4-4. Differential scanning calorimetry traces for pure ligands showing baseline corrected heat flow as a function of temperature. Each ligand exhibits a single peak indicative of a direct phase transition from the crystal to isotropic liquid phase. " Reproduced with permission from the American Chemical Society" [106]

4.5 Ligand Exchange Process

For surface modification of quantum dots, I exchanged the ODA ligand with a mesogenic ligand (LC-QDs). This exchange involves 1 ml of quantum dot (CdSe/ZnS nanocrystal) solution with an octadecylamine ligand (ODA) attached and mixed with 1 mL of acetone. Free ligand was removed by centrifugation at 7000 rpm for 10 mins. The supernatant was discarded and then the last step was repeated again with the precipitate two times by adding 1 mL of acetone. Once washing is done, the precipitate was dissolved in 1 mL of chloroform and mixed with 1 mL solution of the synthesized ligand in chloroform (0.01 g/ml). ODA was then exchanged with the new ligand on the QD surface by heating at 40 °C and stirring the solution at 200 rpm for 5 hours. The mixture was then removed from the heating stage and left to cool to room temperature. The free ligand was removed by washing it with 1 mL of acetone and centrifuged for 10 min, and then washed again twice by adding 1 mL of acetone. Finally, the precipitate was dissolved in 1 mL toluene.

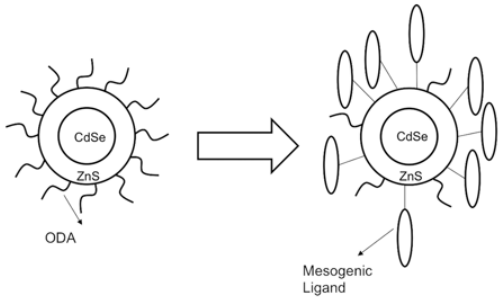

Figure 4-5. Schematic representation of non-mesogenic ODA ligands and modified surface of QDs with mesogenic and ODA ligands (LC-QDs),

4.6 Nuclear Magnetic Resonance (NMR) Spectroscopy

Nuclear magnetic resonance spectroscopy (NMR) has emerged as an important tool for determining the chemical structure of organic molecules. NMR can quantitatively analyze a mixture of known compounds. There are varieties of NMR techniques that can be used for quantification of samples. For example; ^{1}H NMR is the most common NMR experiment that provides information about the number of protons in a sample. Amir Keshavarz performed ^{1}H NMR studies to quantify the ligand exchange process. Data was collected before and after ligand exchange to verify the completion of the reaction. NMR spectra for the ODA, the isolated mesogenic ligand, and the newly ligand-exchanged LC-QD were also used to calculate the average ratio of mesogenic ligand to remaining ODA ligand on the particle surface.

The mesogenic ligand was synthesized by Amir Keshavarz. NMR spectra were obtained by Amir in CDCl3 solution on Agilent spectrometers, with ^{1}H NMR spectra obtained at 500 MHz and referenced to the residual $CDCl_3$ singlet at 7.26 ppm. ^{13}C NMR spectra were obtained by Amir at 125 MHz and referenced to the centerline of the residual

$CDCl_3$ triplet at 77.1 ppm. Selected spectral data were also collected for commercial ODA–QD: ^{1}H NMR ($CDCl_3$, 500 MHz) δ ; ^{13}C NMR ($CDCl_3$, 500 MHz) δ.

As shown in figure 4-6: Amir Keshavarz used the triplet (CH_2 next to the amine) to obtain the ratio of mesogen: ODA on the particle surface. The CH_2 next to the amine of the free ligand has a chemical shift at 2.69 ppm in deuterated chloroform (Amir use deuterated solvents to prevent unwanted solvent signals). However, this chemical shift changes to 3.26 ppm when the amine is attached to the quantum dot. The CH_2 next to the amine of the commercially available ODA-QD has a chemical shift of 2.36 ppm in $CDCl_3$. Based on these values, after each ligand exchange, Amir obtained this ratio by measuring the peak height relative to a line drawn through the base of the peak.

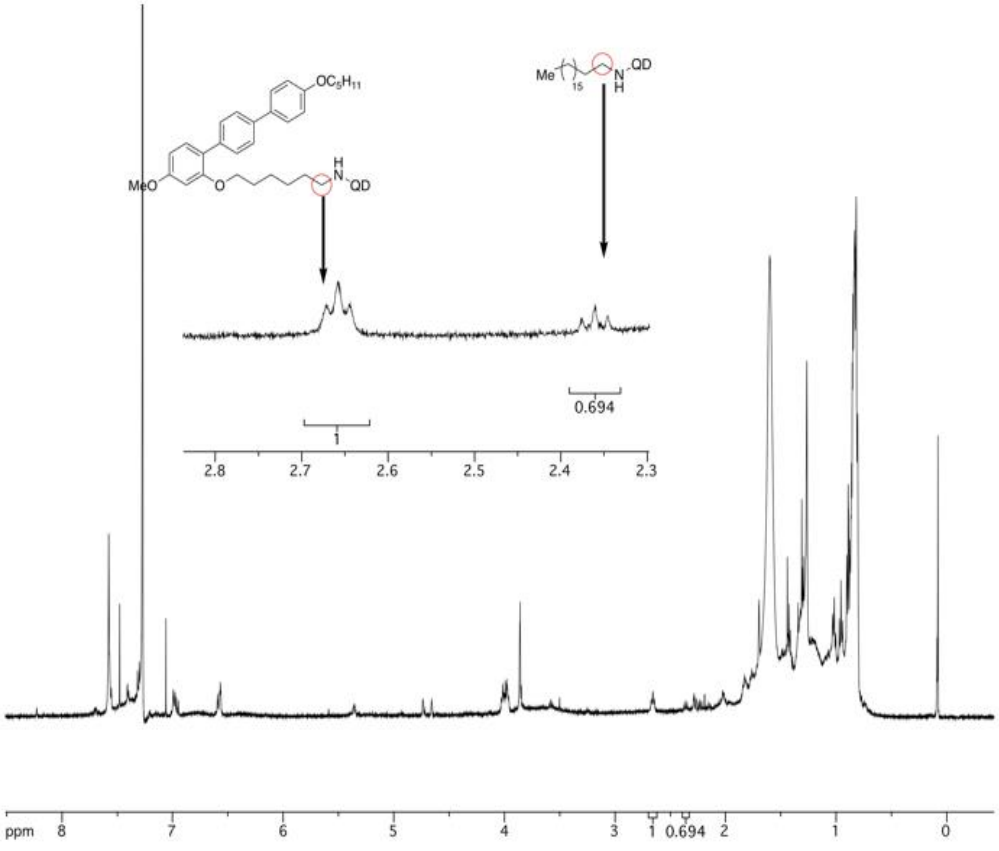

Figure 4-6. The ^{1}H NMR spectrum after ligand exchange obtained at 500 MHz in CDCl3. "Reproduced with permission from the American Chemical Society" [106]

4.7 Liquid Crystal/Quantum Dot Mixtures

After completing and quantifying the surface modification, I proceeded to prepare the nanocomposite by mixing the hard material (LC-QDs) with the soft liquid crystal host. To achieve a good initial dispersion, I take a small quantity of LC-QD in toluene and add this to 4'-pentyl'4-biphenylcarbonitrile (5CB) to produce mixtures at different LC-QD weight percentages (0.075 - 0.3 wt %). The LC/toluene/QD mixture is placed into a water bath sonicator and heated to 43^{o}C (above the clearing point for 5CB). The mixture is sonicated for 3-8 hours to achieve a homogeneous dispersion of QDs in the isotropic LC phase and to evaporate excess toluene from the system. For low QD concentrations, below 0.1 wt %, the amount of added toluene will evaporate within 2 hours of sonication. If any toluene remains, it will lower the isotropic to nematic transition temperature, and if there is excess of toluene present, the nematic phase will no longer be present at room temperature. In general, it is important to test the transition temperature of the LC to ensure the solvent has been completely removed. Once dispersion is complete the mixture is removed from the sonicator and briefly stored in a 50^{o}C oven.

To prepare microscope slides for observation, glass slides and cover slips are first washed with soap and water then sonicated in a progression of acetone, methanol and ethanol for 20 minutes each. Finally, the glass is blown dry with ultra-high purity nitrogen the material is sandwiched between a standard glass slide and I tuned the thickness of cover slip by using a polymer spacer film.

The composite material is transferred to a microscope slide at 50^{o}C to maintain the isotropic phase then these slides are moved to a heated stage, to control the cooling rate of the slide. At 34.3°C, the transition from isotropic to nematic in the composites is present, similar to that for pure 5CB. QD dynamics can be observed using a Leica DM2500P upright microscope in epi-fluorescence mode, equipped with a Q-image Retiga camera. Luminescence of the QDs enables us to follow the movement and distribution of nanoparticles as a function of time. To provide controlled cooling in these experiments, I used a Linkham LTS350 hot stage with custom liquid nitrogen cooled-air attachment. This apparatus allowed us to observe the phase transition at 7°C/min, 15°C/min, 20°C/min, and 30°C/min.

4.8 Shell Formation Procedure

I attached ligands 4a–4c and 4e–4h to commercially available 6.2 nm octadecylamine (ODA)-functionalized quantum dots (QDs) using the ligand exchange reaction previously reported In the case of 4a, ^{1}H NMR analysis of the QDs following ligand exchange revealed a 60:40 ratio of ligand 4a to ODA bound on the QD's. Interestingly, in our previous study using ligand C (Figure 4.1), the same exchange procedure led to a 90:10 ratio. Each of the ligand-modified quantum dots that I prepared readily dispersed in 4-cyano-4'-pentylbiphenyl above the clearing point (34 °C). Upon cooling from the isotropic to nematic phase, the ligand modified QD's all spontaneously assemble into microcapsules similar to those previously observed using QD's modified with ligand C (Figure 4.1). The ligand is understood to promote uniform particle dispersion

in the isotropic phase8 and stabilize capsule formation via nematic phase templating. Figure 4.8a shows a fluorescence microscope image of mesostructures formed using QD's functionalized with ligand 4a (for other ligands, see the figure 4.9. Reheating to above the nematic phase clearing point of 34 °C and recooling did not destroy the capsules (Figure 4.7b), nor did heating to the maximum temperature allowed by our experimental setup (350 °C, Figure 4.7c). For comparison, QD's functionalized with ligand C (Figure 4.1) decompose at just 120 °C.9 The thermostability of QD's functionalized with 4a bodes well for potential materials applications [107,108].

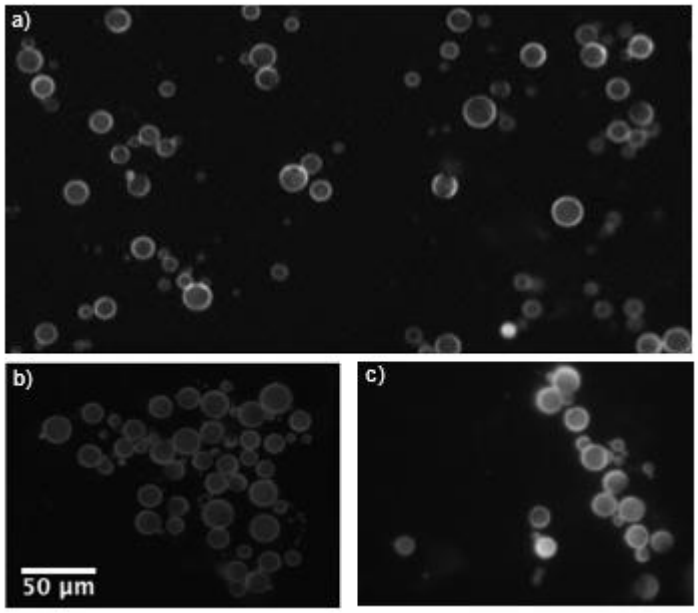

Figure 4-7**. Same-slide ambient temperature fluorescence microscope images of QD mesostructures formed from 6.2 nm CdSe/ZnS QDs (λmax= 540 nm) functionalized with ligand 4a following disper-sion in 4-cyano-4'-pentylbiphenyl (0.15 wt %) after a) depositing on the slide; b) reheating the slide through the clearing point; and c) reheating the slide to 350 °C. Images record total fluorescence emission intensity following excitation at λ_{max}= 540 nm. "Reproduced with permission from the American Chemical Society" [106]**

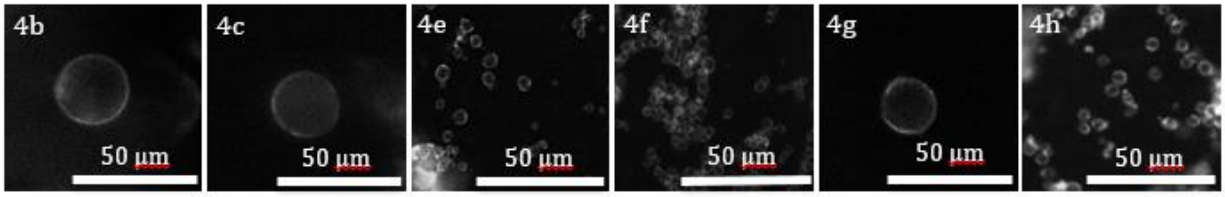

Figure 4-8. Fluorescence microscopy images of QD mesostructures formed from 6 nm CdSe/ZnS QDs (λmax= 540 nm) functionalized with different ligands. "Reproduced with permission from the American Chemical Society" [106]

4.9 Preparation for SEM Imaging

To further characterize the nanoscale morphology of the QD shells, scanning electron microscopy (SEM) images were captured. 0.2 µl of liquid crystal-functionalized QDs mixture was pipetted onto a copper grid with 300 mesh carbon film, while holding the composite material at a temperature above the nematic–isotropic phase transition point. The grid was then cooled into the nematic phase, forming shells suspended in 5CB directly on the grid. Finally the 5CB was washed from the grid with acetone by pipetting a droplet onto the grid surface then wicking and evaporating the excess solvent.

Figure 4.9 shows two representative SEM images from the same sample grid: one of an intact shell composed of densely packed functionalized QD's (Figure 4.9a), and one of a fractured shell (Figure 4.9b). The latter confirms that the microstructure is indeed hollow, with a relatively thin wall. Approximately 15% of the shells observed using SEM are fractured, presumably as a result of mechanical shear during sample preparation.

Mechanical methods independent of temperature can in fact be used to break the capsules, using fast shearing for example. I propose that these novel ligands can be applied to high temperature applications where encapsulation stability under high temperature is required. Such a property distinguishes these capsules from other, more temperature sensitive encapsulation technologies such as polymersomes and liposomes, or the thermally sensitive capsules from our group's earlier work.

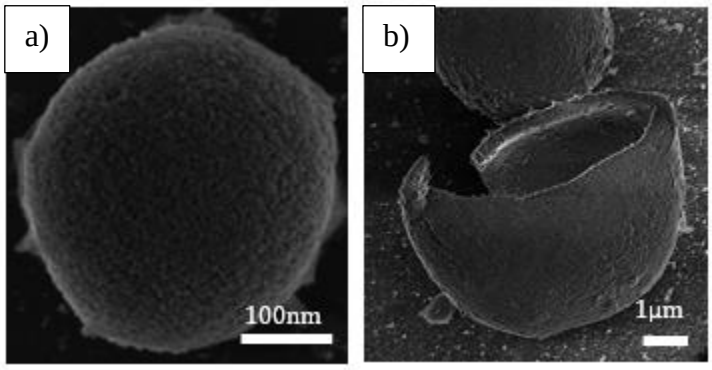

Figure 4-9. Scanning electron microscope images of a) intact and b) fractured QD capsules formed from 540 nm CdSe/ZnS QDs functionalized with ligand 4a. "Reproduced with permission from the American Chemical Society" [106]

4.10 SAXS Analysis of Shells

I next quantified nanoparticle packing in the shell wall using small-angle x-ray scattering (SAXS) measurements following our established method [20]. Figure 4.10 shows scattering intensity as a function of the scattering vector, **q**. The observed peaks are related to the average quantum dot separation within a shell wall, d, as $q = 2\pi/d$. For each sample, I observed a broad diffraction peak (the positions of which were determined by subtracting a baseline from the raw data and fitting a Gaussian). As shown in Figure 4.10,

linker arm length has a significant effect on inter-particle separation. The homologous series of ligands 4c, 4b, 4a, and 4e, employing 3-, 4-, 6-, and 12-carbon aminoalkyl linkers, respectively, afforded inter-dot separations of 10.15nm, 11.79nm, 12.94nm, and 13.25 nm an apparent logarithmic correlation between inter-dot separation and aminoalkyl chain length (inset, Figure 4.10). Interestingly, when the ethereal arm (green, Table 1) is changed from CH_3 to C_4H_9, the aminoalkyl chain length no longer correlates to interparticle spacing; in fact, the ligand bearing the most aliphatic carbons that I evaluated (4h) affords microcapsules with the closest average inter-dot distance (10.11 nm).

Microcapsules were prepared via nematic templating by heating 0.15 wt % of functionalized quantum dots in 4-cyano-4'-pentylbiphenyl above the nematic–isotropic transition point (34 ^{0}C), then cooling back to the nematic phase in an Eppendorf tube. After gentle centrifugation, the shells were inserted into 1.5 mm borate glass x-ray capillaries, and further centrifuged to form a pellet at the bottom of capillary.

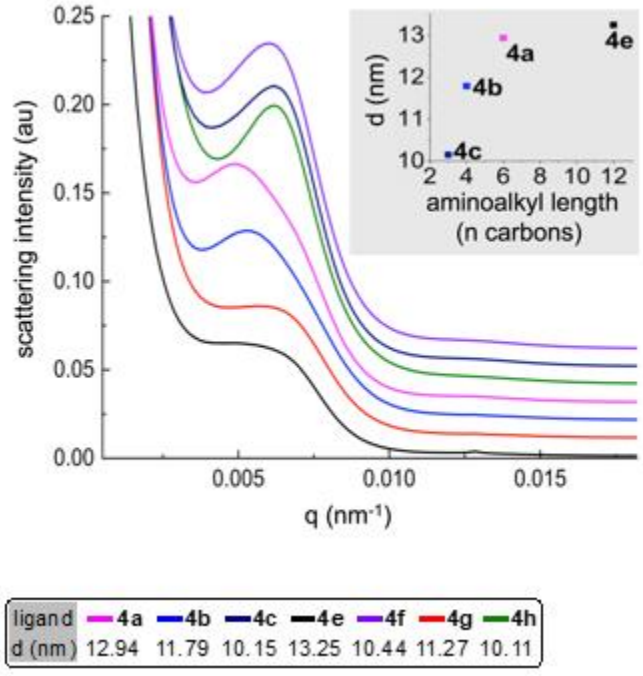

Figure 4-10. Small-angle x-ray scattering (SAXS) data collected at 10 keV with 1 s exposure for assembled quantum dot microshells suspended in nematic liquid crystal prepared at 0.15 wt %, and plotted as relative intensity as a function of scattering vector, q. The characteristic interparticle spacing, d, is calculated from each peak position as 2π/q. Insert shows interparticle spacing (d) as a function of ligand aminoalkyl chain length. "Reproduced with permission from the American Chemical Society" [106]

In our previous work, QD emission spectra and fluorescence lifetimes where characterized using drop-cast films and nanoparticle clusters of the same particles in liquid

crystal.[109] I found that mesogenic ligands of different alkyl chain lengths can be used to tune the QD emission spectrum by modulating Förster resonance energy transfer (FRET) between QDs. In some cases, FRET could be avoided by using a ligand which produced an average NP spacing greater than 10 nm. The SAXS data presented in Figure 4.10 strongly supports functionality for the new ligands. Additional possibilities for spectral modification are possible by encapsulating dye molecules within the optically active capsules.

Given the ability of the capsule structures to remain intact up to very high temperatures, for practical optical applications using QDs thermal luminescence quenching becomes a concern. Isolated QDs lose luminescence intensity significantly at high temperatures and irreversible quenching mechanisms can degrade performance over time under temperature cycling [110]. For example, in high temperature applications such as high-power LEDs for lighting, the operating temperature can be up to 200^{o}C. To test for thermal quenching in the capsule geometry I performed preliminary testing to characterize the effects of heating to 300^{o}C and cooling back to room temperature (See figure 4.11). Although a degree of irreversible quenching is observed, the capsules retain some luminescence up to 300^{o}C. Loss of capping ligands at high temperatures is a well-known mechanism for irreversible QD quenching but in this solid-like capsule configuration, where the ligands interact and stabilize the structure such a mechanism is not expected to dominate.

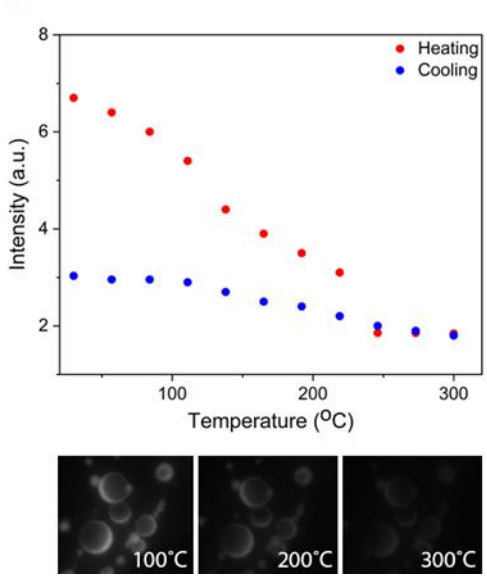

Figure 4-11. Quenching effect of temperature on QD Luminescence. "Reproduced with permission from the American Chemical Society" [106]

4.11 Conclusions

In previous work our group presented a new method to control the micro-scale assembly of nanoparticles using nematic liquid crystal as a host phase. For this purpose, I needed to modify the surface of the quantum dots with a mesogenic ligand. This step

increased dispersion stabilization in the liquid crystal, while providing an attractive short-range interaction between particles.

In summary, I have developed a rapid, modular synthesis of new side-attaching calamitic promesogenic ligands. Their attachment to quantum dots and subsequent self-assembly in a liquid crystal host demonstrates the broad applicability of nematic templating. In addition to its modularity and scalability, the new ligand scaffold is noteworthy for its ability to deliver remarkably thermostable quantum dot microcapsules. Due to the unique thermal stability of our capsules, they may be well-suited for a wide range of applications in various fields, particularly encapsulations. Empowered by this scalable and modular ligand synthesis, future studies will endeavor to investigate the influence of ligand structure on shell formation, stability, and porosity.

Chapter 5

Nanoparticle-based hollow microstructures formed by two-stage nematic nucleation and phase separation

5.1 Introduction

Materials with hollow microstructures such as spherical shells, networks, and tubes have many useful technological applications in areas such as catalysis, sensing, batteries, and encapsulation/controlled release [111,112]. Top-down synthetic strategies to produce hollow microstructures include the use of soft or hard templates [113], spray techniques [114], and microfluidic methods [115]. Hollow structures can also be formed via template-free self-assembly. A popular one-pot synthesis technique takes advantage of Ostwald ripening [116], where crystals initially nucleate as solid spheres arranged in a porous, polycrystalline texture, and then subsequently become hollow as smaller grains in the interior dissolve and recrystallize to larger grains on the exterior, forming spherical shells or tubes. One drawback of this method is that Ostwald ripening is slow, and typically requires hours of processing time. I report a template-free, rapid synthetic method to produce hollow microstructures composed of nanoparticles that self-assemble in less than 1s into tightly packed hollow spheres, foams, and tubular networks. Our method is based on the use of a liquid crystal solvent which undergoes a two-stage nucleation process on cooling through the isotropic–nematic phase transition.

Dispersion and controlled assembly of nanoparticles in a soft material (i.e., polymer or liquid crystal) can produce a diverse array of interesting structured materials. Unlike conventional liquids, soft phases with orientational order can organize nanoparticles by aggregation (e.g., at topological defects.) The resulting composite material may retain advantageous physical properties of the matrix (elasticity, birefringence, electro-optic actuation, etc.). Alternately, stable nanostructures can be harvested by removal from the host phase.

Liquid crystals (LCs) are optically anisotropic fluids in which the constituent molecules exhibit local orientational order. LCs are particularly useful for display and photonics applications, because surface anchoring conditions and confinement can be used to manipulate global molecular orientation and produce macroscopic domains with a defined optic axis. When particles are dispersed into an aligned nematic liquid crystal phase, depending on surface anchoring conditions on the particle, an elastic deformation of the LC director may be imposed. Ligands can be used to define surface anchoring and force the surrounding LC molecules to align at an angle relative to the surface (perpendicular to a spherical particle for example). This means the inclusion of a particle creates spatial frustration, relaxed by the formation of topological defects. Recently, there has been much interest in nanoparticle and colloidal assembly at interfaces [117] and via topological defect lines and points in the nematic phase [118,119].

In recent years the field of soft nanocomposites has grown rapidly. Materials that combine nanoparticles with a fluid-like host show great potential for generation of soft-phase templated meta-materials [120,121,122,123] (e.g., biopolymers[124,125],

biomolecules[126,127], or block copolymers[128,129,130]). These applications take advantage of a soft material's ability to spontaneously segregate and organize particles by their chemical and/or physical properties. Although soft host materials are complex fluids—intrinsically weakly ordered or disordered on the molecular scale—they often exhibit nano-to-micron-scale repeat units, as seen in the phase-separated microstructures of block copolymers [131], or the defect lattices of the LC blue phase [132]. Nanoparticle assembly can be achieved via particle patterning in topological defects or interfaces and many applications do not require a highly ordered particle lattice. Hence soft-phase assembly methods represent an attractive, fast, and low-cost approach to produce interesting mesoscale hollow materials from nanoparticles.

Nanoparticle aggregation can also be driven by a phase transition in the host phase. In a series of seminal papers, Terentjev and colleagues [133,134,135] first reported the formation of micron-scale particle networks and cellular structures assembled at the isotropic-to-nematic phase transition using an elastically driven liquid crystal phase separation effect. They used the growth of ordered domains to generate a porous structure as colloidal particles were expelled from the nematic phase.

I expand on this pioneering work and use a dynamic two- stage nucleation and growth process to spatially organize nano- particles, which are subsequently stabilized into a family of hollow structures. The method is rapid and template-free, performed close to room temperature using a widely available LC material, and, in principle, can be adapted to any nanoparticle type with appropriate surface modification. Instead of the micron-to-120 nm radius colloids used by Terentjev and colleagues [133,134,135], I report experiments using much smaller nanoparticles—6 nm diameter quantum dots. When dissolved in an LC host, such small particles depress the isotropic-to-nematic transition temperature [136] and exhibit high solubility in the isotropic phase but low solubility in the nematic phase. This combination of material properties gives rise to a two-stage nucleation process on cooling. The net Frank elastic energy cost for a particle to be located in the anisotropic nematic phase when compared to location in the isotropic phase provides an interesting mechanism for nano- particle spatial organization [137, 18, 138]. When the temperature drops below the isotropic–nematic transition point, particles are expelled from nucleating nematic domains and segregate to isotropic domains. Due to the high nanoparticle (NP) concentration, these domains remain in the isotropic state as the isotropic–nematic transition temperature is locally depressed. On further cooling, the NP-rich isotropic domains undergo secondary nematic nucleation at a lower temperature. During this second stage of nucleation, NPs spontaneously segregate to the surface of the isotropic domains, thus forming hollow microstructures. This two-stage isotropic–nematic transition thus provides a mechanism to create hollow structures. To enable this process, our NPs are functionized with ligands selected to both promote solubility in the isotropic phase and enhance local attractive particle–particle interactions for final structure stability. Control over final morphology and pore size depends on the cooling rate though T_{NI} and initial particle concentration in the liquid crystal solvent. The two-stage process is easier to control than the Ostwald ripening method, which depends on grain size distribution and diffusion rates. Besides proceeding much more rapidly and providing morphological control by changing the NP density and cooling rate, one can also select a different LC

solvent, or mixture of solvents, and/or change the species of ligands coating the NPs. These options open a broad chemical design space to optimize the process for any desired application.

5.2 Results

Formation of hollow nanoparticle-based microstructures. The two basic elements of the liquid crystal/nanoparticle system used in this research are a nematic liquid crystal (5CB, 4'-pentyl-4- biphenylcarbonitrile, Sigma Aldrich) and ligand-modified CdSe/ ZnS core/shell quantum dots (LC-QDs) (NN Labs, core diameter 6.2 nm, absorption peak, λ_{max} = 620 nm). The mesogenic ligand 8 [17], inspired by the liquid crystals employed by the groups of Dunmur [139] and Vashchenko [140], was prepared by Amir Keshavarz using the sequence of reactions shown in Figure. 5-1d.

The octadecylamine (ODA) surface ligands of the commercial QDs were exchanged with mesogenic ligand 8. The mesogenic ligand's flexible amine tether is thought to encourage alignment with the local liquid crystal director 5CB, increasing dispersability in the isotropic phase, while the rod-like aromatic motif may enable attractive interaction between closely packed particles. The degree of ligand exchange was quantified using ^{1}H nuclear magnetic resonance (NMR) spectroscopy, revealing a 9:1 surface ratio of 8 to ODA.

Figure 5-1 shows representative fluorescence images of three distinct nanoparticle micro-morphologies: a branching network of tube-like structures (a); multi-compartment droplets of closed- cell foam (b); and single compartment hollow capsules (c). The structures are imaged suspended in nematic liquid crystal at room temperature. In the case of the individual capsules and the foam, liquid crystal is present throughout the structure (inside and outside the enclosed compartments), which I verified by cross- polarized microscopy. The final solid structures exhibit stable shapes insensitive to thermal fluctuations—that are retained even if the host liquid crystal phase is heated above the isotropic transition point.

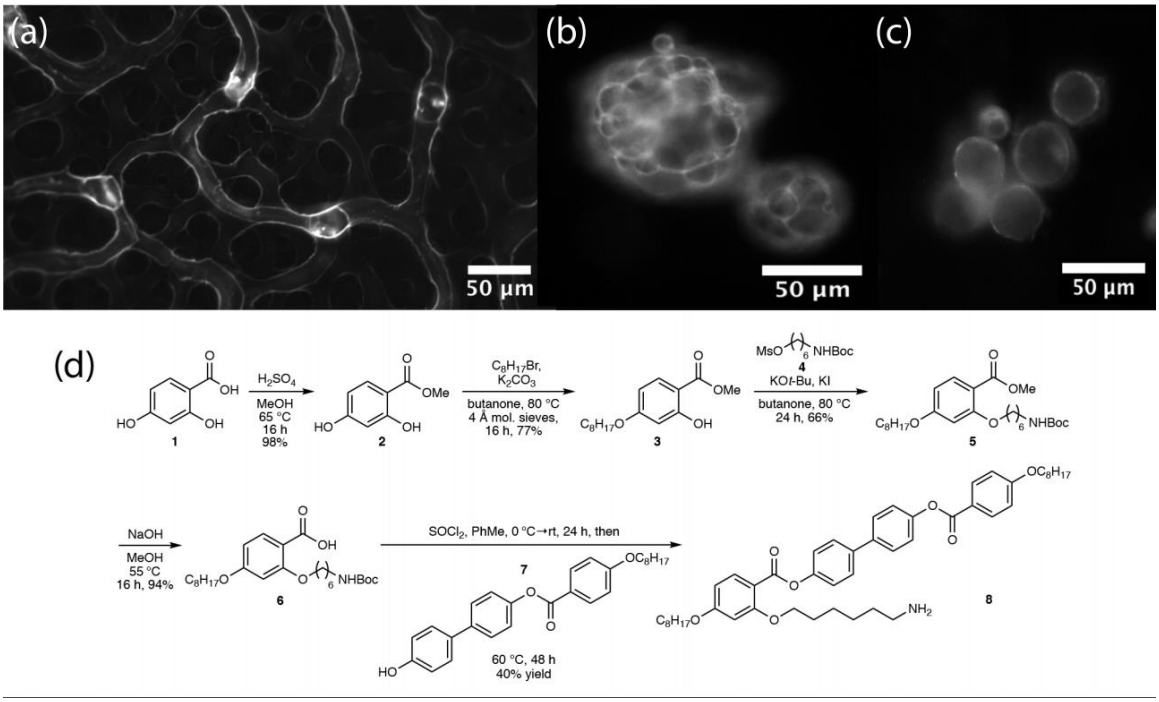

Figure 5-1. Hollow nanoparticle-based microstructures formed from ligand-modified quantum dots. Fluorescence microscopy imaging demonstrates the three distinct quantum dot structures formed under different conditions: a branching tubular network, formed at 1 °C min^{-1}, b solid closed-cell foam-like structures formed at 30 °C min^{-1}, and c hollow shell capsules formed at 200 °C min^{-1}. All structures are composed of 620 nm CdSe/ZnS ligand-modified quantum dots, suspended in nematic liquid crystal initially at 0.15 wt% at room temperature. d Sequence of reactions used to prepare the mesogenic ligand (8) for nanoparticle attachment. "Reproduced with permission from the Nature Publishing Group" [104]

Qualitative observations initially revealed that final structure type and size could be controlled by varying either the initial particle concentration or the cooling rate through the isotropic-to-nematic transition. To examine these trends, I constructed a qualitative morphological phase diagram as a function of these parameters, and measured the size dependence of the final structures. In Fig. 5-2 a–c, d–f, respectively, representative fluorescence images of the hollow shell morphology demonstrate the dependence of spherical shell and foam droplet size on cooling rate and concentration. To quantitatively analyze these data, I imaged many shells and foam droplets. Figure 5-2 h, i plots separately the outer dimensions of the assembled structures as a function of cooling rate and particle concentration. Structure diameters were measured using *Image J* software, and an average was taken over all structures formed under the same conditions.

For each data point shown on the graphs (Figure. 5-2 h, i), the total number of measured structures, *n*, ranged from 10 to 183. In some cases, low numbers were measured because a particularly large size (e.g., >50 μm in diameter at 7 °C min^{-1}, 0.3 wt%, Figure. 5-2 a) produced fewer structures per microscope slide. In the case of multi- compartment foam droplets (Figure. 5-1b for example), the outer diameter was measured in several places, and an average value for each droplet was used (rather than the value of individual internal voids).

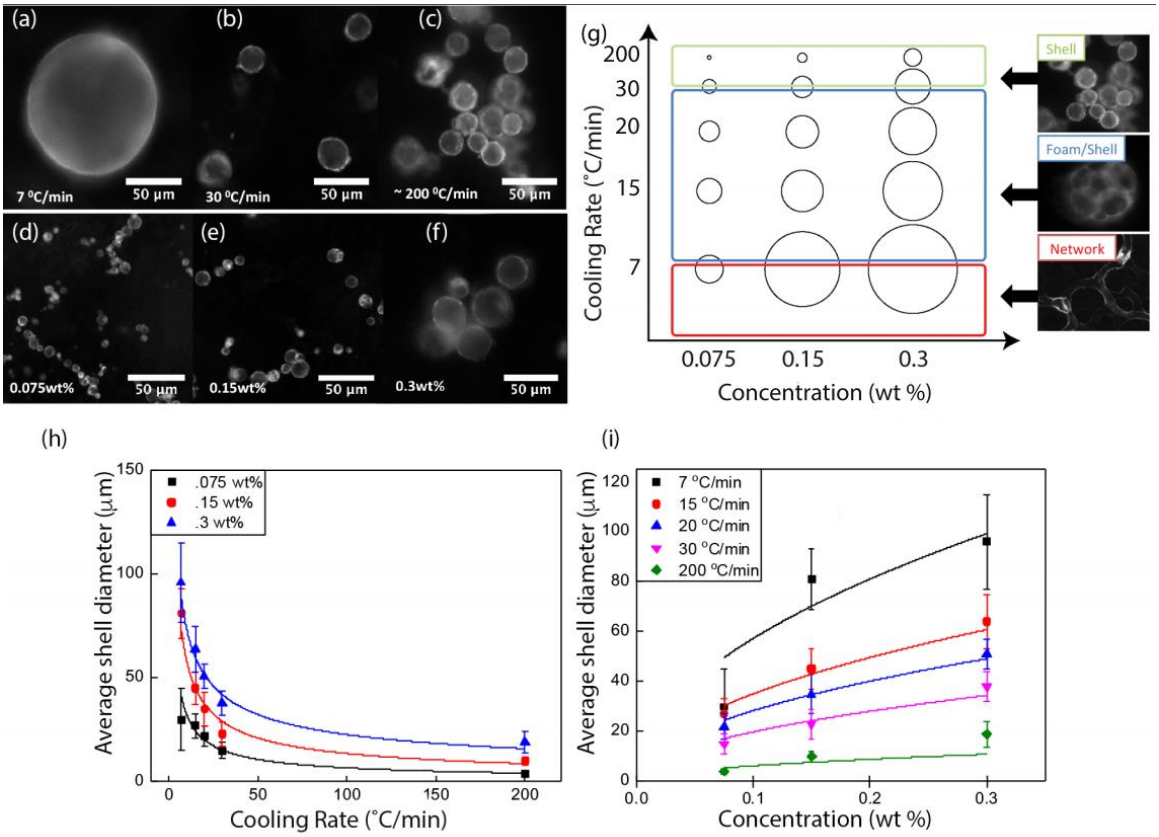

Figure 5-2. Size dependence of cooling (quench) rate and nanoparticle concentration. Representative fluorescence microscopy images of spherical shells formed from ligand-modified quantum dots (LC-QDs) at a–c fixed LC-QD concentration of 0.3 wt% in 5CB, varying cooling rate, and d–f fixed cooling rate of 200 °C min^{-1}, varying LC-QD concentration in 5CB. g Qualitative phase diagram for the three distinct morphologies predominantly observed as a function of cooling rate and concentration. General morphological zones on the diagram are indicated by the colored boxes with circle size representative of structure size. h, i Plots of average shell diameter vs. cooling rate and concentration respectively, with error bars indicating standard deviation (s.d.); the total number of measured structures, *n*, ranged from 10 to 183. "Reproduced with permission from the Nature Publishing Group" [104]

The diagram in Figure. 5-2 g shows two important trends. Firstly, structural morphology is dependent on system cooling rate and, secondly, particle concentration is a factor in morphological size control. At high cooling rates (~200 °C min^{-1}), single hollow shells predominate, while at the lowest cooling rates, individual macrostructures do not stabilize, resulting in the network morphology. The intermediate range is particularly interesting: between cooling rates of 7 and 30 °C min^{-1}, I observed a surprising 'foam' structure: discrete compartmentalized 'droplets' suspended in the nematic host phase (Figure. 5-1b), with a closed-cell foam-like morphology. In the intermediate region of the diagram in Figure. 5-2 g (indicated by the blue box), I often observed a mixture of individual capsules and foam-like structures (the colored boxes are a guide to indicate general behavior, not a discrete structural change). The network region was only observed at cooling rates below 7 °C min^{-1}; a characteristic length scale in that case was not measured.

Figure 5-3 shows more detailed confocal fluorescence imaging of the foam-like structure. In general, these multi-compartment structures form as discrete droplets (Figure. 5-3 a–e), although more extended bulk foams, particularly near the edges of the formation chamber (Figure. 5-3f), are also observed. On first observation, foam droplets initially appeared to be composed of several shells fused together, but microscope observations of single compartment shells over time provided no evidence that fusion can take place after formation. The shells are mechanically quite rigid with walls that can be in a solid phase. Inner compartments were sometimes observed to merge during the formation process while the particles remained dispersed in the isotropic fluid.

There is an interfacial tension between the nematic and isotropic phases, and as isotropic domains shrink, they tend to minimize their free energy by adopting minimal surface geometries either spherical capsules or, in the case of the foam, a network of minimal interfaces. Our observations provide evidence that nanoparticles in shrinking domains remain in a dispersed fluid state until the point of arrest.

Size dependence on cooling rate and nematic phase coarsening. Figure 5-4 a–d shows snapshots from a high-speed fluorescence movie (captured using a Phantom VEO-410L camera), recording the distribution of quantum dots in our composite material as the nematic phase nucleates, grows, and merges to leave shrinking isotropic domains. Lighter regions indicate isotropic domains and dark regions highlight nematic domains, depleted of particles. The images in Figure.5-4 highlight the stages of structure formation: initial phase separation (Figure. 5-4 a), nematic domain growth (Figure. 5-4 b), growth and merging of the nematic domains and transitioning to the point where the shrinking isotropic domains separate (Figure. 5-4 c), and lastly shrinkage of those isotropic domains into capsules (Figure. 5-4 d). This sequence leads to the formation of mostly single compartment shells. The time-point in Figure. 5-4 c is notable as it indicates a stage where the isotropic domains pinch off into droplets. These separating isotropic domains contain the particles that go on to form the final foams and capsules and I noted a qualitative relationship between early coarsening length scales and final capsule/foam size.

The process of initial nematic nucleation and growth can be described by a universal growth law, $L(t) \sim t^d$, where t is the time after an initial temperature quench, L is the domain diameter, and d the growth exponent. Experimentally, this growth exponent, d,

has been measured to lie between 0.5 and 1.0 for the I–N phase transition, depending on quench depth [141]. In a more recent numerical study, Bradač et al.[142] predicted the influence of quench time t_q on early-stage I–N coarsening dynamics to be a power law, relating the average size of protodomains, ξ, to the quench time, in the form, $\xi \sim t_q^n$. When ξ was measured at a fixed time for different quenches, the power law was obtained as $n = 0.25$. Quench time (i.e., time over which a quench crosses the transition) is inversely related to cooling rate, and hence I can expect the characteristic size of our assembled structure, (ξ_r) to increase as cooling rate decreases. It is not obvious how these nucleation and growth models apply to our system where particle concentration is time dependent. In the initial stages of nematic nucleation and coarsening (wherein particle concentrations are still relatively low), however, I can focus on the dependence of domain length scales with cooling rate. Fitting a power law to the data shown in Figure. 5.2 h produced a fit of the form $\xi_r \sim c^{-n}$, where n = 0.51, 0.63, and 0.69, and c represents cooling rate, for three different particle concentrations, respectively. It is likely that larger shells arrest at an earlier time because they more rapidly reach maximum particle density at the shrinking spherical interface, given a constant cooling rate. A $y = x^{0.5}$ fit to the data in Figure. 5-2 i supports this hypothesis.

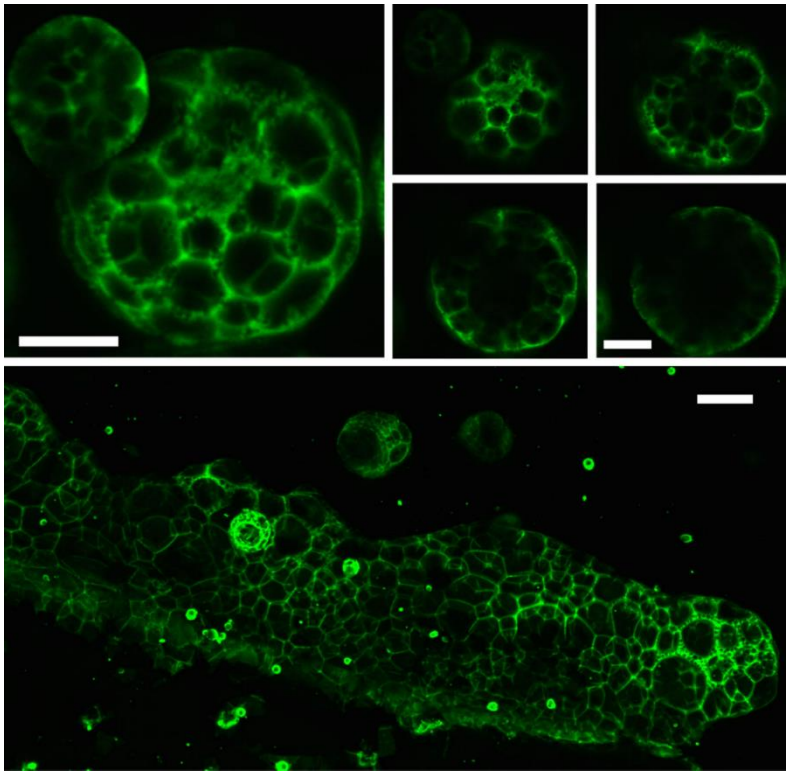

Figure 5-3. Confocal imaging of foam structures. Confocal microscope *z*-projection images of a quantum dot foam droplet (*z* depth = 23.13 μm) with four representative slices (b–e) at *z* intervals of 0.665 μm; and f a large foam structure (*z* depth = 91.90 μm). Scale bars for b–e are 50 μm. "Reproduced with permission from the Nature Publishing Group" [104]

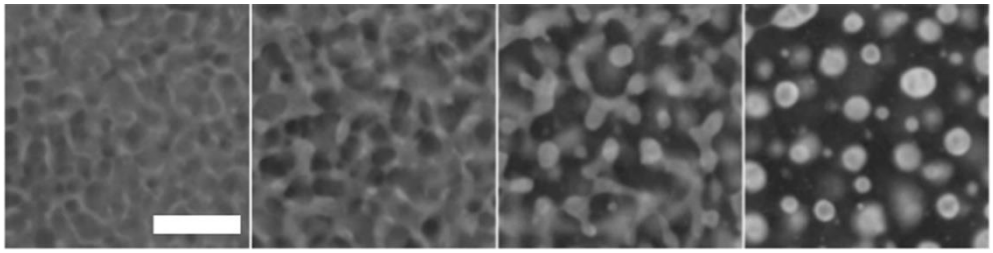

Figure 5-4. a–d Experimental high-speed video imaging snapshots representative of four stages in nematic nucleation and growth during the process: a initial nucleation and growth, b coarsening, c domain separation, and d secondary nucleation. Scale bars is 50 μm. "Reproduced with permission from the Nature Publishing Group" [104]

Mechanism for structure differentiation. To better elucidate the governing mechanisms behind network, foam, and capsule formation, I carried out fluorescence microscope video imaging during the formation process. This technique allowed us to track particle distribution throughout the transition a significant advance over previous related studies. Our observations revealed that the process for all three possible structures can be broken into three stages: (1) particle sorting, in which the initial nematic domains nucleate and grow (concentrating the QDs into shrinking isotropic phase domains), (2) Secondary nematic nucleation, where nematic domains appear inside the shrinking isotropic domains and (3) concentration-induced morphological arrest where particles interact via short range ligand–ligand attraction. As I speculated in a recent publication this arrest likely occurs due to stabilizing intermolecular π interactions between the benzene rings of the ligands as the particles are pushed together. The third step is the key to stabilizing the final structure size, but additional explanation is needed to understand the formation of the three distinct structures under different cooling rates.

Figure 5-5 shows a time sequence for foam formation (Figure. 5-5 a–f and close up, Figure. 5-5g). These snapshots reveal an important observation: while the bright isotropic domain is shrinking (but still extended and amorphous in shape), several nematic domains can be seen to simultaneously nucleate and grow inside (Figure. 5-5g). These secondary domains subsequently grow, leading to multiple inner compartments. This early secondary nucleation is necessary to produce multi-compartment structures. The internal domains grow, pushing the particles together at multiple interior interfaces in a process that produces multiple thin-walled compartments, the particles concentrate and arrest-hence the solid-walled foam-like morphology. In the case of capsules, I observe that the isotropic domains adopt a spherical shape before the secondary nematic nucleation is observed.

The important question then arises: why do faster cooling rates lead to single compartment shells and slower rates lead to the foam and network morphologies? A critical factor appears to be the timing of secondary nematic nucleation with respect to overall isotropic domain shape evolution. The secondary nematic nucleation drives the particles into their final arrested configurations, but why does this secondary, delayed nucleation occur at all? I can understand this effect simply by considering the effect of impurities on the isotropic-to-nematic phase transition temperature. The nanoparticles in our experiment are ~6 nm in size, a comparable length scale to that of the host nematic molecules, and

therefore I can consider them as impurities that will depress the I–N transition temperature [136]. In a microscopy study of the I–N phase transition as a function of particle concentration, I demonstrate that increasing particle concentration in 5CB from 0.01 to 0.6 wt% depresses the transition temperature by approximately 6 °C. Given the expected higher concentrations of QDs in the shrinking isotropic domains after a quench (compared to the initial low concentration state where the first nematic nucleation occurs), I can expect those interior particle-rich isotropic regions to transition later—provided this step can be considered as analogous to a quasi-static compression with a uniform particle distribution maintained during domain shrinkage. This assumption possibly highlights a key difference between our work and the earlier work by Terentjev and colleagues [133,134,135] in which 120–150 nm particles were used. In our experiments I were able to image the complete phase separation process, directly verifying uniform particle distribution throughout.

All three structures begin at the same initial condition, with particles uniformly distributed in the isotropic liquid crystal phase. In the first nucleation stage, nematic domains form and grow, concentrating the particles in the remaining isotropic phase. This stage is demonstrated in Fig. 5-5 b–d for the foam. Coupled to this process via local particle concentration is the secondary nematic nucleation. This secondary nucleation step ultimately leads to compaction of the particles, arrest, and structure stabilization in either a network, foam, or capsule. Figure 5-5 e, g captures the process as it happens for a structure that ultimately results in the foam morphology. As I can see in both cases, nematic domains form within the bright isotropic domain. I have observed that the relative timing of the two nucleation steps is critical in determining the final arrested structure. If secondary nematic nucleation occurs while the particle-rich isotropic domain is still in a connected network (for example, as represented in Figure. 5-5i, left, nematic phase shown in grey), the secondary domains will grow and push the particles to form connected tubes. If secondary nucleation occurs at the stage shown in Figure. 5-5g (large, non-spherical isotropic domains, Figure. 5-5i, center) I can see multi-compartment foam-like structures. Finally, if secondary nucleation occurs at the spherical domain stage (Figure. 5-5i, right), single compartment shells will likely form.

5.3 Discussion

Growth rates of the primary and secondary nematic nucleation are coupled by an interesting concentration effect. As the primary nematic domains grow and evolve in morphology, simultaneously local particle concentration increases in the isotropic domain. In a fast quench, the nematic phase rapidly nucleates and the system phase separates into many shrinking small spherical isotropic domains, each containing a high concentration of particles. These high local particle concentrations cause the secondary nematic nucleation to occur later since the I–N transition temperature is decreased by several degrees. In comparison, a slow quench produces a lower growth exponent for the initial nematic nucleation. This results in larger domains and less rapid concentration of the particles the secondary nucleation will occur with a shorter time lag, before the system evolves all the way to spherical isotropic domains. Our findings therefore suggest that control of the

cooling rate not only provides control over structure size due to coarsening dynamics, but also provides control over the timing of the secondary nucleation and thus final morphology (shell, foam, or network).

The reported process of nucleation-and-growth-templating using a liquid crystal phase transition can be compared to the ice-crystal growth templating method used in polymer hydrogel formation [143]. In such systems, the growth of solid crystal domains throughout the material forces dissolved polymers to migrate to the shrinking surrounding fluid phase and porous polymeric hydrogels can be formed. In our liquid crystal system, instead of using a growing solid phase to redistribute dispersed material, I use the nucleation of the fluid nematic phase to expel nanoparticles, as initially reported in larger particle systems[133,144] and subsequently studied by our group and others [137, 138]. In a related experimental system, Yamamoto and Tanaka [145] demonstrated the existence of a second nematic transition using a micro emulsion of nanoscale inverse micelles with strong surface anchoring and a biphasic region in the phase diagram. The authors were somewhat speculative on the mechanism, but it seems that a phase separation process does result from the growth of nematic domains. Further work will be needed to explore the connection between this work and our own. In our system, particle-induced secondary nematic nucleation provides a route to a rich array of porous structures. The process is not dependent on particle type, and therefore it can be adapted to a variety of photonic and electromagnetic applications where nanoparticle assembly on the mesoscale is advantageous.

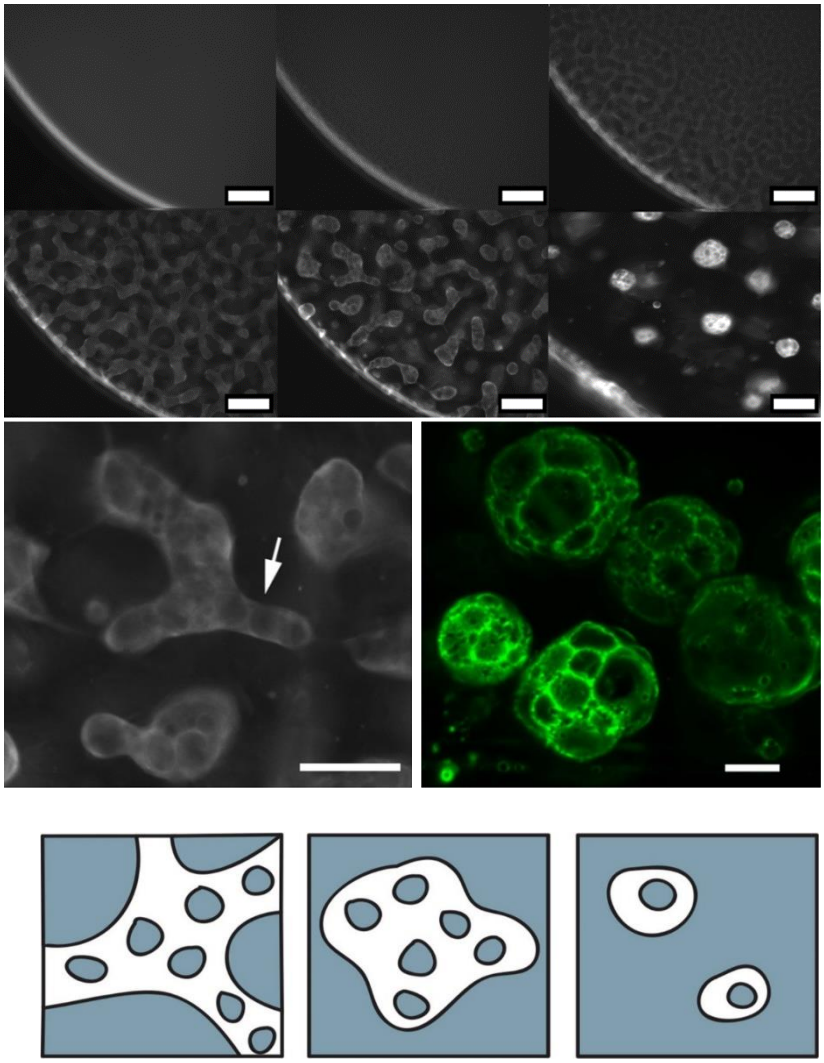

Figure 5-5. Understanding the mechanism for structure differentiation. (a–f) Series of snapshots taken from a fluorescence microscope movie demonstrating the foam formation process in a droplet of liquid crystal with initially well-dispersed quantum dots (QDs). In these images, QD-rich areas appear light and QD- poor areas appear dark. The curved white line in these images is the edge of the droplet, with liquid crystal on the right of this curve. Scale bars for (a–f) are 100 μm. g A zoomed-in view from e with the arrow indicating inner nematic domain nucleation. h A confocal microscope image of several foam structures suspended in 5CB. Images taken from stack of 40 images, Max projected and false colored using Fiji software. i schematics illustrating the role of secondary nucleation on final structure showing the particle-rich isotropic phase as white and the nematic phase as gray left: secondary domains nucleate early on while the isotropic domain is still connected, center: secondary domains nucleate after isotropic domains have separated, and right: secondary domains nucleate late, when isotropic domains have already reached a small size. "Reproduced with permission from the Nature Publishing Group" [104]

Using two-stage nucleation and growth of nematic domains in an isotropic liquid crystal host phase containing dispersed ligand-modified nanoparticles, I can generate stable nanoparticle superstructures. These structures include extended solid foams and individual capsules ranging from 1 to 50 μm in size. These structures are formed entirely as a response to the isotropic-to-nematic phase transition in a single component liquid crystal host phase with no additional substrate for the nanoparticles or solvent. Our results demonstrate the surprising versatility of this nematic-to-isotropic transition templating approach.

Liquid crystal nanocomposites represent an emerging field with many new phenomena to explore. In particular, structure formation based on domain nucleation and growth in liquid crystals is largely undeveloped. In the liquid crystal family of materials, there is great variation in structure, from the simple nematic phase, to highly complicated structures such as the blue phases, bicontinuous gyroid structures in lyotropic systems, and the many different smectic variant phases. Each of these phases exhibits different growth morphologies related to domain nucleation, and thus I see the potential to generate a large family of LC growth templated structures based on this process.

5.4 Methods

5.4.1 NMR nanoparticle characterization.

^{1}H NMR spectra of purified nanoparticles were collected by Amir Keshavarz before and after ligand exchange following established procedure [20]. Using this procedure, Amir Keshavarz calculated the average ratio of mesogenic ligand to remaining ODA ligand on the particle surface, γ, as the ratio of *X*:*Y* where *X* is the area under the triplet corresponding to the mesogenic ligand and *Y* is the area under the triplet corresponding to the ODA ligand. As before all the results presented in this chapter were produced with a nanoparticle γ ratio of 9:1.

5.4.2 Nanocomposite preparation.

Different amounts of mesogen-modified QDs in toluene (0.075–0.3 wt%) were mixed with 5CB and bath sonicated at 43 °C (in isotropic phase for the 5CB host) for 3–8 h. This produced a homogeneous dispersion of particles in the liquid crystal and ensured evaporation of any residual toluene. For low QD concentrations (below 0.1 wt%), the amount of added toluene evaporated within 2 h of sonication. Toluene removal was verified by checking the isotropic-to-nematic phase transition temperature. At higher QD concentrations, it was important to test this transition temperature to ensure adequate solvent removal. After dispersion, the mixtures were moved to a 50 °C oven.

To prepare the QD microstructures, clean glass slides and coverslips were coated with an alignment layer to produce the desired LC orientation. For planar alignment (molecules lie parallel to the glass) glass was dip coated with a 1 wt% aqueous polyvinyl alcohol solution, dried, and rubbed with a velvet cloth to induce an alignment direction. The thickness between glass slide and cover slip was tuned to ~120 μm, using a spacer

film. All microscope slides were assembled at 50 °C oven to maintain the system's isotropic phase above 34.3 °C. Cooling rate was carefully controlled in these experiments using a Linkham LTS350 hot stage equipped with an in-house designed liquid nitrogen cooled air system. I used several different cooling rates; 7 °C min^{-1}, 15 °C min^{-1}, 20 °C min^{-1}, and 30 °C min^{-1} with this apparatus. In addition, I used a room temperature quenching method to achieve a cooling rate of ~200 °C min^{-1}. This was carried out by removing the microscope slide from the hot stage and placing it on a room temperature lab bench. QD fluorescence and the corresponding LC textures were observed using a Leica DM2500P upright microscope equipped with a Q-image Retiga camera. Experiments were performed at three different QD concentrations in liquid crystal; 0.075 wt%, 0.15 wt%, and 0.3 wt%.

5.5 Conclusion

Using two-stage nucleation and growth of nematic domains in an isotropic liquid crystal host phase containing dispersed ligand-modified nanoparticles, I can generate stable nanoparticle superstructures. These structures include extended solid foams and individual capsules ranging from 1–50 μm in size. These structures are formed entirely as a response to the isotropic to nematic phase transition in a single component liquid crystal host phase with no additional substrate for the nanoparticles or solvent. Our results demonstrate the surprising versatility of this nematic-to-isotropic transition templating approach.

Liquid crystal nanocomposites represent an emerging field with many new phenomena to explore. In particular, exploration of structure formation based on domain nucleation and growth in liquid crystals is largely unexplored. In the liquid crystal family of materials, there is great variation in structure, from the simple nematic phase, to highly complicated structures such as the blue phases, bicontinuous gyroid structures in lyotropic systems, and the many different smectic variant phases. Each of these phases exhibits different growth morphologies related to domain nucleation, thus I see the potential to generate a large family of LC growth templated structures based on this process.

Chapter 6

Future work

In this thesis, I described our discoveries related to phase-transition-templated control of micro-shells formed from nanoparticles dispersed in a liquid crystal host. By changing the nanoparticle concentration and cooling rate of samples, to modulate how they transitioned from the isotropic to nematic phase, I were able to change the diameter of shells. In addition, this process led to the discovery of novel morphologies; nanoparticle foams and a new network structure, also controlled by tuning the process cooling rate. If I cool at a moderate rate (7-30°C/min) I obtain a foam structure and if I cool the system slower, I produce tube-like structures. Elucidation of how the same process can control the size of the shells and produce two new hollow microstructures made of closed packed nanoparticles lead to the development of a new model, based on secondary nematic nucleation.

An open question about this model centers on how the formation of the network structure be explained. Currently the model is based around the nucleation of secondary nematic domains. However, in the case of the network structures, the nanoparticle walls form along long sections of liquid crystal. How this formation occurs is still unclear and needs to be studies in more detail. One approach will be to record the formation of the network structure using a high-speed camera, as the entire process of formation happens in approximately 1 second, despite cooling the system through the transition at a very slow rate. As well as analyzing the dynamics of formation, SEM will be used to analyze the structure of the network to see how the nanoparticles pack and image the possible tube structures. Confocal microscopy can also be used to understand the internal structure of network phase. In addition, we need to investigate the foam structures in more detail, including the thickness of foam interfaces and find out how we can control this parameter. I believe having more information about the surface structure, it will help us to understand more the thermal stability of shell.

For the foam structure I am pursuing research into its applications, using it a gas sensor. Due to its large internal surface area, these materials can be used to detect trace chemicals in the air. CdSe particles aren’t useful for this endeavor, however the physics that guided the assembly of these nanoparticles into micro shells works regardless of composition of the particle. This means we can substitute it for a more effective particle, namely gold nanoparticles. The approach using gold nanoparticles is that under normal conditions the foam structures will have a certain conductivity, given an appropriate ligand design, and when atmospheric conditions change with the introduction of a foreign substance, the conductivity of the foam-based film will change as well.

Another promising avenue of future work will be to alter the ligands used to functionalize the nanoparticles for both liquid crystal and non-liquid crystal applications. Surface ligands are commonly used to prevent aggregation of nanomaterials in solution, but surface modification of QDs can also lead to greater chemical stability and increased particle longevity, as well as acting to modify optical and electronic properties. Mesogenic ligands, incorporating a rod-like core section can also be employed to assemble

nanoparticles into three-dimensional structures, facilitating a stable particle-particle linkage, or a thermally breakable connection or to produce bulk nanocomposite phases. The surface ligand exchange can also be carried out with a variety of end goals, such as suspension of QDs in water or water-based solvents for hydrophilic products and as a way to improve charge transport in photovoltaics. This can additionally be used to alter the spacing of individual particles, altering their interactions such as reducing the effects of FRET.

Bibliography

1. G. R. Desiraju, Crystal Engineering: The Design of Organic Solids (Elsevier, New York, 1989).

2. L. Isaacs, D. N. Chin, N. Bowden, Y. Xia, G. M. Whitesides, in Supramolecular Technology, D. N. Reinhoudt, Ed. (Wiley, New York, 1999), pp. 1–46.

3. S. Jakubith, H. H. Rotermund, W. Engel, A. von Oertzen, G. Ertl, Phys. Rev. Lett. 65, 3013 (1990).

4. B. Hess, Naturwissenschaften 87, 199 (2000).

5. J. Aizenberg, A. J. Black, G. M. Whitesides, Nature 398, 495 (1999).

6. A. van Blaaderen, R. Ruel, P. Wiltzius, Nature 385, 321 (1997).

7. Poulin, P.; Stark, H.; Lubensky, T. C.; Weitz, D. A. Novel Colloidal Interactions in Anisotropic Fluids. Science1997, 275, 1770–1773.

8. Fleury, J.-B.; Pires, D.; Galerne, Y. Self-Connected 3D Architecture of Microwires. Phys. Rev. Lett.2009, 103.76

9. Coursault, D.; Grand, J.; Zappone, B.; Ayeb, H.; Lévi, G.; Félidj, N.; Lacaze, E. Linear Self-Assembly of Nanoparticles Within Liquid Crystal Defect Arrays. Adv. Mater2012, 24, 1461–1465.

10. Blanc, C.; Coursault, D.; Lacaze, E. Ordering nano-and microparticle assemblies with liquid crystals. Liquid Crystals Reviews2013, 1, 83–109.73

11. Hegmann, T.; Qi, H.; Marx, V. M. Nanoparticles in Liquid Crystals: Synthesis, Self-Assembly, Defect Formation and Potential Applications. J Inorg. Organomet. Polym.2007, 17, 483–508.

12. Wang, X.; Miller, D. S.; Bukusoglu, E.; de Pablo, J. J.; Abbott, N. L. Topological defects in liquid crystals as templates for molecular self-assembly. Nat. Mater2016, 15, 106–112.

13. Škarabot, M.; Ravnik, M.; Žumer, S.; Tkalec, U.; Poberaj, I.; Babič, D.; Muševič, I. Hierarchical self-assembly of nematic colloidal superstructures. Physical Review E2008, 77.

14. Ramaswamy, S.; Nityananda, R.; Raghunathan, V. A.; Prost, J. Power-Law Forces Between Particles in a Nematic. Molecular Crystals and Liquid Crystals Science1996, 288, 175–180.

15. Muševič, I.; Škarabot, M.; Tkalec, U.; Ravnik, M.; Žumer, S. Two-Dimensional Nematic Colloidal Crystals Self-Assembled by Topological Defects. Science2006, 313, 954–958.

16. Rodarte, A. L.; Pandolfi, R. J.; Ghosh, S.; Hirst, L. S. Quantum dot/liquid crystal composite materials: self-assembly driven by liquid crystal phase transition templating. J. Mater. Chem. C2013, 1, 5527.

17. Rodarte, A. L.; Nuno, Z. S.; Cao, B. H.; Pandolfi, R. J.; Quint, M. T.; Ghosh, S.; Hein, J. E.; Hirst, L. S. Tuning Quantum-Dot Organization in Liquid Crystals forRobust Photonic Applications. Chem. Phys. Chem.2014, 15, 1413–1421.

18. Rodarte, A. L.; Cao, B. H.; Panesar, H.; Pandolfi, R. J.; Quint, M.; Edwards, L.; Ghosh, S.; Hein, J. E.; Hirst, L. S. Self-assembled nanoparticle micro-shells templated by liquid crystal sorting. Soft Matter 2015, 11, 1701–1707

19. Quint, M. T.; Sarang, S.;Quint, D. A.; Keshavarz, A.; Stokes, B. J.; Subramaniam, A. B.; Huang, K. C.; Gopinathan, A.; Hirst, L. S.; Ghosh, S. Plasmon-Actuated Nano-Assembled Microshells. Sci. Rep.2017

20. Riahinasab, S. T.; Elbaradei, A.; Keshavarz, A.; Stokes, B. J.; Hirst, L. S. Nanoparticle Microstructures Templated by Liquid Crystal Phase-Transition Dynamics, Proc. SPIE2017, 10125, 1012503-1012503-7.

21. F. Reinitzer, Monatsch. Chem., 9, 421 (1889).

22. O. Lehmann, Z. Phys. Chem., 4, 462 (1889).

23. T. Kato, Y. Hirai, S. Nakaso, M. Moriyama, Royal Society of Chemistry, (2007).

24. Helfrich, W.; Schadt, M. Voltage-dependent optical activity of a twisted nematic liquid crystal. In Crystals That Flow; Stegemeyer, H., Sluckin, T., Dunmur, D., Eds.; CRC Press, 2004; Vol. 2, pp. 537–541 ISBN 978-0-415-25789-3.

25. Chandrasekhar, S.; Sadashiva, B. K.; Suresh, K. A. Liquid crystals of disc-like molecules. Pramana1977, 9, 471–480.

26. A Saupe, A Jakli. One-And Two-Dimensional Fluids. NW: CRC Press, (2006).

27. Seo, D.; Iimura, Y.; Kobayashi, S. Temperature dependence of the polar anchoring strength of weakly rubbed polyimide films for the nematic liquid crystal (5CB). Applied Physics Letters1992, 61, 234–236.

28. Chaikin, P. M.; Lubensky, T. C. Principles of Condensed Matter Physics, 1st ed.; Cambridge University Press: University Printing House, Cambridge CB2 8BS, United Kingdom, 1995; ISBN 0-521-43224-3.

29. Lagerwall, J. P. F.; Giesselmann, F. Current Topics in Smectic Liquid Crystal Research. ChemPhysChem2006, 7, 20–45.

30. Gibbons, W. M.; Shannon, P. J.; Sun, S.-T.; Swetlin, B. J. Surface-mediated alignment of nematic liquid crystals with polarized laser light. Nature1991, 351, 49.75

31. Schiekel, M. F.; Fahrenschon, K. Deformation of Nematic Liquid Crystals with Vertical Orientation in Electrical Fields. Applied Physics Letters1971, 19, 391–393.

32. Nose, T.; Sato, S. A liquid crystal microlens obtained with a non-uniform electric field. Liquid Crystals1989, 5, 1425–1433.

33. Quint, M. T.; Delgado, S.; Paredes, J. H.; Nuno, Z. S.; Hirst, L. S.; Ghosh, S. All-optical switching of nematic liquid crystal films driven by localized surface plasmons. Optics Express2015, 23, 6888.

34. Brody, T. P.; Asars, J. A.; Dixon, G. D. A 6 #215; 6 inch 20 lines-per-inch liquid-crystal display panel. IEEE Transactions on Electron Devices1973, 20, 995–1001, doi:10.1109/T-ED.1973.17780.

35. Tsvetkov, V. N. & Mikhailov, G. M. Acta Physicochim. U. R. S. S. 8(1938).

36. Sengupta, A. Liquid Crystal Theory. In Topological Microfluidics; Springer International Publishing: Cham, 2013; pp. 7–36 ISBN 978-3-319-00857-8.

37. Ghosh, S. K. A model for the orientational order in liquid crystals. Il Nuovo CimentoD4,229–244 (Sept. 1984).

38. O. D. Lavrentovich, Nematic Liquid Crystals: Defects, (2001).

39. Collings, P.J. Liquid Crystal.Princeton: Princeton University Press, (2002).

40. Sengupta, A. Liquid Crystal Theory. In Topological Microfluidics; Springer International Publishing: Cham, 2013; pp. 7–36 ISBN 978-3-319-00857-8.

41. Nathan Melton, thesis, Phase-Templated Self-Assembly of Nanoparticles in Confined Liquid Crystal

42. I. Dierking, A review of polymer-stabilized ferroelectric liquid crystal, Materials, 7(5), 3568-3587 (2014).

43. J. Nehring, A. Saupe, On the schlieren texture in nematic and smectic liquid crystals, J. Chem. Soc., Faraday Trans. 2, 68, (1970).

44. Sant, S. B. Nanoparticles: From Theory to Applications.Materials and Manufactur-ing Processes27,1462–1463 (2012).

45. Kang, Y. S., Risbud, S., Rabolt, J. F. & Stroeve, P. Synthesis and Characterization ofNanometer-Size Fe3O4 and -Fe2O3 Particles.Chemistry of Materials8,2209–2211(1996).

46. Dobson, J. Gene therapy progress and prospects: magnetic nanoparticle-based genedelivery. Gene Therapy13,283–287 (2006).

47. Rudge, S.et al. Adsorption and desorption of chemotherapeutic drugs from a mag-netically targeted carrier (MTC). Journal of Controlled Release74.Proceeding ofthe International Symposium on Tumor Targeted Delivery Systems, 335–40. ISSN:0168-3659 (2001).

48. Pankhurst, Q. A., Connolly, J., Jones, S. K. & Dobson, J. Applications of magnetic nanoparticles in biomedicine.Journal of Physics D: Applied Physics36,R167(2003).

49. Brus, L. Electron-electron and electron-hole interactions in small semiconductor crystallites: The size dependence of the lowest excited electronic state.The Jour-nal of Chemical Physics80,14403–4409 (1984).

50. Bawendi, M. G., Steigerwald, M. L. & Brus, L. E. The Quantum Mechanics of Larger Semiconductor Clusters ("Quantum Dots"). Annual Review of Physical Che-mistry41,477–496 (Oct. 1990).

51. Alivisatos, A. P. Perspectives on the Physical Chemistry of Semiconductor Nanocrystals. The Journal of Physical Chemistry100,13226–13239 (1996).

52. Sukhanova, A.et al. Biocompatible fluorescent nanocrystals for immunolabeling ofmembrane proteins and cells. Analytical Biochemistry324,60–67. ISSN: 0003-2697(2004).

53. Resch-Genger, U., Grabolle, M., Cavaliere-Jaricot, S., Nitschke, R. & Nann, T.Quantum dots versus organic dyes as fluorescent labels.Nature methods5 9,763–75(2008).

54. He, Y.et al. Photo and pH Stable, Highly-Luminescent Silicon Nanospheres andTheir Bioconjugates for Immunofluorescent Cell Imaging.Journal of the AmericanChemical Society131.PMID: 19235931, 4434–4438 (2009).

55. Mason, J.et al.Novel fluorescence-based approaches for the study of biogenicamine transporter localization, activity, and regulation.Journal of Neuroscience Me-thods143.Studying Monoamine Transporters: Beyond Hypermonoaminaemia, 3–25.ISSN: 0165-0270 (2005).

56. Lin, C.-C.et al. Highly efficient CdS-quantum-dot-sensitized GaAs solar cells. Opt.Express20, A319–A326 (Mar. 2012).

57. Chen, K.-J.et al. Resonant-Enhanced Full-Color Emission of Quantum-Dot-BasedDisplay Technology Using a Pulsed Spray Method.Advanced Functional Materials22,5138–5143.ISSN: 1616-3028 (2012).

58. Kim, T.-H.et al. Full-colour quantum dot displays fabricated by transfer printing. Nature Photonics5,176–182 (Mar. 2011).

59. Saikia, K., Deb, P. & Kalita, E. Sensitive fluorescence response of ZnSe(S) quantumdots: an efficient fluorescence probe.87,065802 (June 2013).

60. Liu, S.-L.et al.Effectively and Efficiently Dissecting the Infection of InfluenzaVirus by Quantum -Dot -Based Single -Particle Tracking.ACS Nano6,141–150(2012).

61. Alivisatos, A. P. Semiconductor Clusters, Nanocrystals, and Quantum Dots.Science271,933–937.ISSN: 0036-8075 (1996)

62. Khalil E. J. Quantum dots solar cells. DOI: 10.5772/59159

63. Vastola, G.; Zhang, Y.-W.; Shenoy, V. B. Current Opinion in Solid State & Materials Science,2012,16(2),

64. Chukwuocha, E. O.; Onyeaju, M. C.; Harry, T. S. T. Theoretical Studies on the Effect of Confinement on Quantum Dots Using the Brus Equation. World Journal of Condensed Matter Physics2012, 02, 96–100.

65. Gao, X.et al. In vivo molecular and cellular imaging with quantum dots. CurrentOpinion in Biotechnology16.Analytical biotechnology, 63–72. ISSN: 0958-1669(2005).

66. Zrazhevskiy, P. & Gao, X. Multifunctional Quantum Dots for Personalized Medicine.Nano today4,414–428 (2009).

67. Lidke, D. S.et al. Quantum dot ligands provide new insights into erbB/HER receptor–mediated signal transduction. Nature Biotechnology22,198–203 (2004).

68. F. C. Frank, 'Liquid crystals. On the theory of liquid crystals', Discuss Faraday, 25, 19 (1958).

69. J. D. Jackson, Classical electrodynamics, 3rd edn. (John Wiley & Sons, Inc., New York, 1998).

70. M. Born and E. Wolf, Principles of optics: electromagnetic theory of propagation, interference and diffraction of light 7th edn (Cambridge University Press, Cambridge, 1999).

71. R. D. Guenther, Modern optics (John Wiley & Sons, Inc., New York, 1990).

72. P. Yeh and C. Gu, Optics of liquid crystal displays (John Wiley & Sons, Inc., New York, 1999).

73. A. Yariv and P. Yeh, Optical waves in crystals (John Wiley & Sons, Inc., New York, 1984).

74. L. S. Hirst, Fundamentals of soft matter science, CRC Press, 2012.

75.Nwaneshiudu, A.et al. Introduction to Confocal Microscopy. Journal of Investigative Dermatology132,1–5 (2012).

76. Quinten, M., Leitner, A., Krenn, J. R., Aussenegg, F. R., "Electromagnetic energy transport via linear chains of silver nanoparticles", Opt. Lett. 23(17), 1331-1333 (1998)

77. Cho, C. Y., Lee, S. J., Song, J.H., Hong, S. H., Lee, S. M., Cho, Y. H., Park, S. J., "Enhanced optical output power of green light-emitting diodes by surface plasmon of gold nanoparticles ", Appl. Phys. Lett. 98, 051106 (2011)

78. Rodarte, A. L., Ferri, C. G. L., Grey, C., Hirst, L. S., Ghosh, S., "Emerging Liquid Crystal Technologies VII", Proc. Of SPIE, 8279H (2012)

79. Verma,Y. K., Inman, R. H., Ferri, C. G. L., Mirafzal,H., Ghosh, S. N., Kelley, D. F., Hirst, L. S., Ghosh, S., Chin,W. C., "Electrical modulation of static and dynamic spectroscopic properties of coupled nanoscale GaSe quantum dot assemblies", Phys. Rev. B 82,165428 (2010)

80. Rodarte, A. L., Cisneros, F., Hein, J.E., Ghosh, S., Hirst, L.S., "Quantum Dot/Liquid Crystal Nanocomposites in Photonic Devices", Photonics. 2, 855-864 (2015)

81. Martinez-Miranda, L. J., McCarthy, K., Kurihara, L. K., "Effect of the surface coating on the magnetic nanoparticle smectic- A liquid crystal interaction", Appl. Phys. Lett. 89, 161917 (2006)

82. Pratibha, R., Park, W., Smalyukh, I. I., "Colloidal gold nanosphere dispersions in smectic liquid crystals thin nanoparticle-decorated smectic films", J. Appl. Phys. 107, 063511 (2010)

83. Hao, Q., Hegmann, T., "Formation of periodic patterns in nematic liquid crystals doped with functionalized gold nanoparticles", J. Matter. Chem. 16, 4197-4205 (2006)

84. Liu, Q. K., Cui, Y. X., Gardner, D., Li, X., He, S., Smalyyukh, I. I., “Self-alignment of plasmonic gold nanorods in reconfigurable anisotropic fluids for tunable bulk metamaterial applications”, Nano Lett. 10(4), 1347-1353 (2010)

85. Kumar, S., Sagari, L. K., “CdSe quantum dots in a columnar matrix”, Chem. Commun. 47, 12182-12184 (2011)

86. Kumar, S., Lakshminarayanan, V., “Inclusion of gold nanoparticles into a discotic liquid crystalline matrix”, chem. Commun. 1600-1601 (2004)

87. Mirzaei, J., Reznikov, M., Hegmann, T., “Quantum dots as liquid crystal dopants”, J. Mater. Chem. 22, 22350-22365 (2012)

88. Hines, D. A.; Kamat, P. V. Recent Advances in Quantum Dot Surface Chemistry. *ACS Appl. Mater. Interfaces*, 2014, *6*, 3041–3057.

89. Lewandowski, W.; Wójcik, M.; Górecka, E. Metal Nanoparticles with Liquid-Crystalline Ligands: Controlling Nanoparticle Superlattice Structure and Properties. *ChemPhysChem* 2014, *15*, 1283–1295.

90. Nealon, G. L.; Greget, R.; Dominguez, C.; Nagy, Z. T.; Guillon, D.; Gallani, J-L.; Donnio, B. Liquid-Crystalline Nanoparticles: Hydrid Design and Mesophase Structures. *Beilstein J. Org. Chem.* 2012, *8*, 349–370.

91. Yu, C. H.; Schubert, C. P. J.; Welch, C.; Tang, B. J.; Tamba, M.-G; Mehl, G. H. Design, Synthesis, and Characterization of Mesogenic Amine-Capped Nematic Gold Nanoparticles with Surface-Enhanced Plasmonic Resonances. *J. Am. Chem. Soc.* 2012, *134*, 5076–5079.

92. Mirzaei, J.; Reznikov, M.; Hegmann, T. Quantum dots as Liquid Crystal Dopants. *J. Mater. Chem.* 2012, *22*, 22350–22365.

93. Whitesides, G. M.; Grzybowski, B. Self-Assembly at all Scales. *Science* 2002, *295*, 2418–2421.

94. Prodanov, M. F.; Pogorelova, N. V.; Kryshtal, A. P.; Klymchenko, A. S.; Mely, Y.; Semynozhenko, V. P.; Krivoshey, A. I.; Reznikov, Y. A.; Yarmolenko, S. N.; Goodby, J. W.; Vashchenko, V. V. Thermodynamically Stable Dispersions of Quantum Dots in a Nematic Liquid Crystal. *Langmuir* 2013, *29*, 9301–9309.

95. Melton, C.; Riahinasab, S.; Keshavarz, A.; Stokes, B.; Hirst, L. Phase Transition-Driven Nanoparticle Assembly in Liquid Crystal Droplets. *Nanomaterials* 2018, *8*, 146.

96. Costa-Fernández, J. M.; Pereiro, R.; Sanz-Medel, A. The Use of Luminescent Quantum Dots for Optical Sensing. *Trends Anal. Chem.* 2006, *25*, 207–218.

97. Jaiswal, J. K.; Mattoussi, H.; Mauro, J. M.; Simon, S. M. Long-Term Multiple Color Imaging of Live Cells Using Quantum Dot Bioconjugates. *Nature Biotechnology* 2003, *21*, 47–51.

98. Dabbousi, B. O.; Rodriguez-Viejo, J.; Mikulec, F. V.; Heine, J. R.; Mattoussi, H.; Ober, R.; Jensen, K. F.; Bawendi, G. (CdSe)ZnS Core–Shell Quantum Dots: Synthesis and Characterization of a Size Series of Highly Luminescent Nanocrystallites. *J. Phys. Chem. B.* 1997, *101*, 9463–9475.

99. Brus, L. Quantum Crystalline and Nonlinear Optics. *Applied Physics A.* 1991, *53*, 465–474.

100. Nozik, A. J. Quantum Dot Solar Cells. *Physica E* 2002, *14*, 115–120.

101. Dayal, S.; Kopidakis, N.; Olson, D. C.; Ginley, D. S.; Rumbles, G. *Nano Lett.* 2010, *10*, 239–242.

102. Munro, A. M.; Bardecker, J. A.; Liu, M. S.; Cheng, Y-J.; Niu, Y-H.; Plante, I. J-L.; Jen, A. K.-Y.; Ginger, D. S. Colloidal CdSe Quantum Dot Electroluminescence: Ligands and Light-emitting diodes. *Microchim. Acta* 2008, *160*, 345–350.

103. Lewandowski, W.; Jatczak, K.; Pociecha, D.; Mieczkowski, J. Control of Gold Nanoparticle Superlattice Properties via Mesogenic Ligand Architecture. *Langmuir* 2013, *29*, 3404–3410.

104. Riahinasab, S. T.; Keshavarz, A.; Melton, C. N.; Elbaradei, A.; Warren, G. I.; Selinger, R. L. B.; Stokes, B. J.; Hirst, L. S. Nanoparticle-Based Hollow Microstructures Formed by Two-Stage Nematic Nucleation and Phase Separation. *Nat. Commun*. 2019, *10*, 894.

105. Prodanov, M. F., Pogorelova, N. V., Kryshtal, A. P., Klymchenko, A.S., Mely, Y., Semynozhenko, V.P., Krivoshey, A. I., Reznikov, Y.A., Yarmolenko, S. N., Goodby, J.W., "Thermodynamically Stable Dispersions of Quantum Dots in a Nematic Liquid Crystal", Langmuir. 29, 9301-9309 (2013)

106. Keshavarz, A.; Riahinasab, S. T.; Hirst, L. S.; Stokes, B. J. New promesogenic ligands for host medium microencapsulation by quantum dots via liquid crystal phase transition templating. ACS Appl. Nano Mater. 2019, DOI: 10.1021/acsanm.9b00476

107. Mang, X.; Zeng, X.; Tang, B.; Liu, F.; Ungar, G.; Zhang, R.; Cseh, L.; Mehl, G. H. Control of Anisotropic Self-Assembly of Gold Nanoparticles Coated with Mesogens. *J. Mater. Chem.* 2012, *22*, 11101–11106.

108. Nguyen, T. D.; Jankowski, E.; Glotzer, S. C. Self-Assembly and Reconfigurability of Shape-Shifting Particles. *ACS Nano* 2011, *5*, 8892–8903.

109. Amaral, J. J.; Betady, E.; Quint, M. T.; Martin, D.; Riahinasab, S. T.; Hirst, L. S.; Ghosh, S. Effect of Mesogenic Ligands on Short and Long-Term Spectral Dynamics and Stability of Core-Shell CdSe/ZnS Quantum Dots. *Mater. Res. Express.* 2016, *3*, 105029.

110. Zhao, Y.; Riemersma, C.; Pietra, F.; Koole, R.; De Mello Donegá, C.; Meijerink, A. High-Temperature Luminescence Quenching of Colloidal Quantum Dots. *ACS Nano*. 2012, *6*, 9058–9067.

111. Lou, X. W. D., Archer, L. A. & Yang, Z. Hollow micro-/nanostructures: synthesis and applications. Adv. Mater. 20, 3987–4019 (2008).

112. Prieto, G. et al. Hollow nano-and microstructures as catalysts. Chem. Rev. 116, 14056–14119 (2016).

113. Caruso, F., Caruso, R. A. & Möhwald, H. Nanoengineering of inorganic and hybrid hollow spheres by colloidal templating. Science 282, 1111–1114 (1998).

114. Boissiere, C. et al. Aerosol Route to Functional Nanostructured Inorganic and Hybrid Porous Materials. Adv. Mater. 23, 599–623 (2011)

115. Fernández-Nieves, A. et al. Novel defect structures in nematic liquid crystal shells. Phys. Rev. Lett. 99, 157801 (2007).

116. Chun Zeng, H. Ostwald ripening: a synthetic approach for hollow nanomaterials. Curr. Nanosci. 3, 177–181 (2007).

117. Toor, A., Feng, T. & Russell, T. P. Self-assembly of nanomaterials at fluid interfaces. Eur. Phys. J. E 39, 57 (2016).

118. Poulin, P., Stark, H., Lubensky, T. C. & Weitz, D. A. Novel colloidal interactions in anisotropic fluids. Science 275, 1770–1773 (1997).

119. Muševič, I., Škarabot, M., Tkalec, U., Ravnik, M. & Žumer, S. Twodimensional nematic colloidal crystals self-assembled by topological defects. Science 313, 954–958 (2006).

120. Hess, O. et al. Active nanoplasmonic metamaterials. Nat. Mater. 11, 573 (2012).

121. Mirin, N. A. & Halas, N. J. Light-bending nanoparticles. Nano Lett. 9, 1255–1259 (2009)

122. Buonsanti, R., Llordes, A., Aloni, S., Helms, B. A. & Milliron, D. J. Tunable infrared absorption and visible transparency of colloidal aluminum-doped zinc oxide nanocrystals. Nano Lett. 11, 4706–4710 (2011)

123. Hedayati, M. K. et al. Design of a perfect black absorber at visible frequencies using plasmonic metamaterials. Adv. Mater. 23, 5410–5414 (2011).

124. Ofir, Y., Samanta, B. & Rotello, V. M. Polymer and biopolymer mediated selfassembly of gold nanoparticles. Chem. Soc. Rev. 37, 1814–1825 (2008).

125. Cheng, W. et al. Free-standing nanoparticle superlattice sheets controlled by DNA. Nat. Mater. 8, 519 (2009).

126. Srivastava, S., Frankamp, B. L. & Rotello, V. M. Controlled plasmon resonance of gold nanoparticles self-assembled with PAMAM dendrimers. Chem. Mater. 17, 487–490 (2005).

127. Shenton, W., Davis, S. A. & Mann, S. Directed self-assembly of nanoparticles into macroscopic materials using antibody–antigen recognition. Adv. Mater. 11, 449–452 (1999)

128. Bockstaller, M. R., Lapetnikov, Y., Margel, S. & Thomas, E. L. Size-selective organization of enthalpic compatibilized nanocrystals in ternary block copolymer/particle mixtures. J. Am. Chem. Soc. 125, 5276–5277 (2003)

129. He, J., Liu, Y., Babu, T., Wei, Z. & Nie, Z. Self-assembly of inorganic nanoparticle vesicles and tubules driven by tethered linear block copolymers. J. Am. Chem. Soc. 134, 11342–11345 (2012).

130. Cui, H., Chen, Z., Zhong, S., Wooley, K. L. & Pochan, D. J. Block copolymer assembly via kinetic control. Science 317, 647–650 (2007).

131. Bockstaller, M. R., Mickiewicz, R. A. & Thomas, E. L. Block copolymer nanocomposites: perspectives for tailored functional materials. Adv. Mater. 17, 1331–1349 (2005).

132. Yoshida, H. et al. Nanoparticle-stabilized cholesteric blue phases. Appl. Phys. Exp. 2, 121501 (2009)

133. Anderson, V. J., Terentjev, E. M., Meeker, S. P., Crain, J. & Poon, W. C. K. Cellular solid behaviour of liquid crystal colloids 1. Phase separation and morphology. Eur. Phys. J. E 4, 11 –20 (2001).

134. Anderson, V. J. & Terentjev, E. M. Cellular solid behaviour of liquid crystal colloids 2. Mechanical properties. Eur. Phys. J. E 4, 21 –28 (2001

135. Petrov, P. G. & Terentjev, E. M. Formation of cellular solid in liquid crystal colloids. Langmuir 17, 2942–2949 (2001).

136. Martire, D. E., Oweimreen, G. A., Ågren, G. I., Ryan, S. G. & Peterson, H. T. The effect of quasispherical solutes on the nematic to isotropic transition in liquid crystals. J. Chem. Phys. 64, 1456–1463 (1976).

137. Rodarte, A. L., Pandolfi, R. J., Ghosh, S. & Hirst, L. S. Quantum dot/liquid crystal composite materials: self-assembly driven by liquid crystal phase transition templating. J. Mater. Chem. C 1, 5527–5532 (2013).

138. Milette, J. et al. Reversible long-range network formation in gold nanoparticlenematic liquid crystal composites. Soft Matter 8, 173–179 (2012).

139. Diez, S. et al. Dielectric studies of a laterally linked siloxane ester dimer. Liq. Cryst. 30, 1021–1030 (2003).

140. Prodanov, M. F. et al. Thermodynamically stable dispersions of quantum dots in a nematic liquid crystal. Langmuir 29, 9301–9309 (2013)

141. Diekmann, K., Schumacher, M. & Stegemeyer, H. Nucleus growth in liquid crystals. Liq. Cryst. 25, 349–355 (1998).

142. Bradač, Z., Kralj, S. & Žumer, S. Early stage domain coarsening of the isotropic-nematic phase transition. J. Chem. Phys. 135, 024506 (2011).

143. Yokoyama, F., Masada, I., Shimamura, K., Ikawa, T. & Monobe, K. Morphology and structure of highly elastic poly (vinyl alcohol) hydrogel prepared by repeated freezing-and-melting. Colloid Poly Sci. 264, 595–601 (1986).

144. Vollmer, D., Schofield, A. B. & Hinze, G. Network formation in suspensions of colloids and liquid crystal: reversibility – memory effects. Progr. Colloid. Polym. Sci. 129,1 –6 (2004

145. Yamamoto, Jun & Tanaka, Hajime Transparent nematic phase in a liquidcrystal-based microemulsion. Nature 409, 321–325 (2001).